

Fundamentals of Atmospheric and Adaptive Optics

Paul Hickson

The University of British Columbia

2008-06-01



1. Introduction	5
2. Atmospheric effects	7
3. Seeing	7
4. Scintillation	8
5. Speckles	8
6. Adaptive Optics (AO)	8
7. Natural guide star adaptive optics (NGAO)	9
8. Laser guide star adaptive optics (LGAO)	10
9. Multi-conjugate (MCAO)	10
10. Multi-object (MOAO)	11
11. Ground-layer (GLAO)	11
12. Mathematical preliminaries	12
13. Probability distribution	12
14. Autocorrelation and covariance	12
15. Power spectrum	13
16. Wiener-Khinchine theorem	14
17. Structure function	14
18. Atmospheric turbulence	15
19. Kolmogorov turbulence	15
20. Index of refraction fluctuations	16
21. Kolmogorov spectrum	17
22. Von Karman spectrum	17
23. Taylor frozen flow hypothesis	17
24. Vertical structure	18
25. Planetary boundary layer	18
26. Shear zones	18
27. Cerro Pachon model	18
28. Propagation of light through a turbulent medium	19
29. Wave propagation	19
30. Coherence functions	20
31. Mean field	20
32. Mutual coherence	21
33. Fourth-order coherence	21
34. Seeing and scintillation	22
35. Phase and amplitude fluctuations	22
36. The Fried parameter	23
37. Atmospheric time constant	24
38. Greenwood frequency	24
39. The scintillation index	25

40. Imaging theory	26
41. Telescope imaging	26
42. Pupils	26
43. Fourier optics	26
44. Fraunhofer diffraction	27
45. Free propagation	27
46. Linear theory: PSF, OTF, MTF	28
47. Effect of seeing on image quality	29
48. Diffraction-limited PSF and MTF	29
49. Effect of seeing	30
50. Strehl ratio	31
51. Zernike functions	31
52. Definition	31
53. Orthogonality	32
54. Fourier components	32
55. Residual atmospheric wavefront variance	32
56. Wavefront sensors and deformable mirrors	35
57. Wavefront sensors	35
58. Shack-Hartmann	35
59. Curvature	35
60. Pyramid	38
61. Interferometric sensors	38
62. Deformable mirrors	39
63. Piezoelectric mirrors	39
64. MEMS mirrors	40
65. Bimorph mirrors	40
66. Segmented mirrors	40
67. Adaptive secondary mirrors	40
68. Conventional AO	42
69. Single-star AO	42
70. Isoplanatic effects	43
71. Control systems	43
72. The Gemini ALTAIR AO system	44
73. AO Performance	47
74. Error contributions	47
75. Laser AO	49
76. Rayleigh and sodium laser systems	49
77. Limitations	50
78. Tip-tilt	50

79. Focal anisoplanatism	50
80. LGS elongation	50
81. Properties of the sodium layer and effects of variability	50
82. Advanced AO concepts	53
83. Atmospheric tomography	53
84. Fourier slice theorem	54
85. MCAO	54
86. MOAO	55
87. GLAO	55
88. Polychromatic AO	55
89. Extreme AO and high-contrast imaging systems	56
90. Astrometry and photometry with AO	58
91. The AO PSF	58
92. Performance gains with AO	58
93. Photometry	59
94. Astrometry	59
95. Limitations arising with AO	60
96. Photometry	60
97. Astrometry	60
98. ELT AO systems	61
99. Thirty Meter Telescope (TMT)	61
100. NFIRAOS	62
101. IRIS	63
102. PFI	63
103. IRMOS	65
104. WFOS	65
105. MIRES	66
106. References	67

1. Introduction

Adaptive Optics (AO) is a technology that allows ground-based optical and infrared telescopes to achieve near-diffraction-limited image quality, under certain conditions. On a large telescope, this provides more than an order of magnitude increase in resolution and several orders of magnitude increase in sensitivity. Figures 1.1 - 1.3 illustrate this performance.

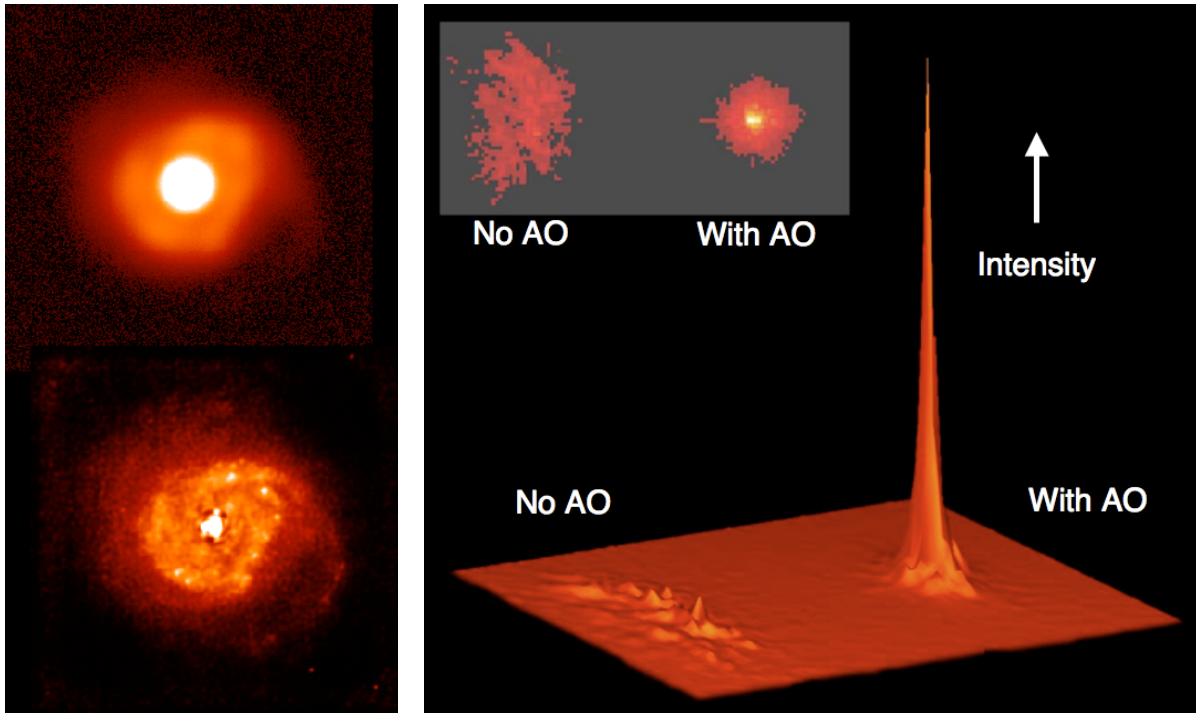


Figure 1.1. The right panel shows an image of the starburst galaxy NGC7469 taken in natural seeing (top) and with adaptive optics (bottom) (Credit: Canada-France-Hawaii Telescope). The right panel shows the image of a star with and without AO. Note the large gain in central intensity of the image, as well as the improvement in resolution (Credit: Claire E. Max, UCSC).

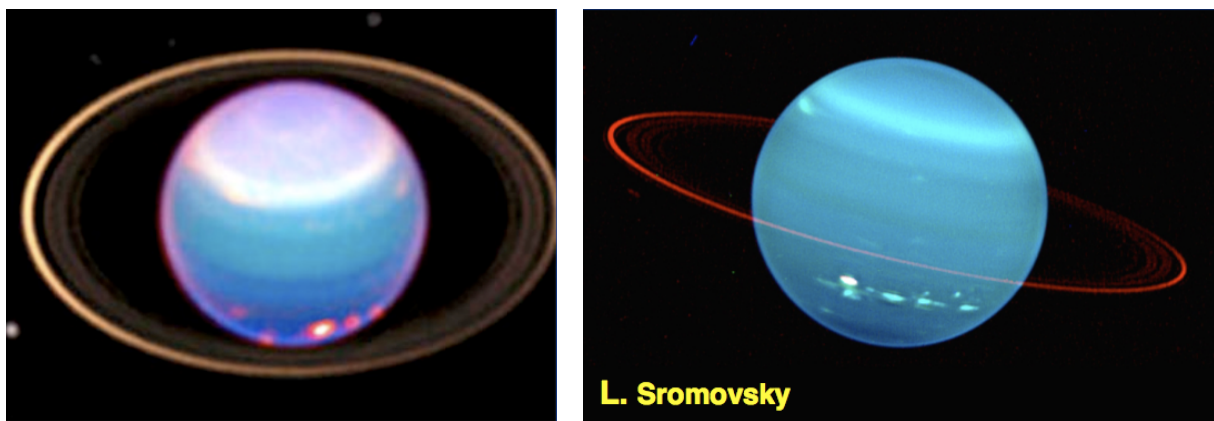


Figure 1.2. Images of Uranus taken in the visible with HST (left) and the near infrared with AO on the Keck telescope (right). The Keck image has better resolution! (Credit: Claire E. Max, UCSC).

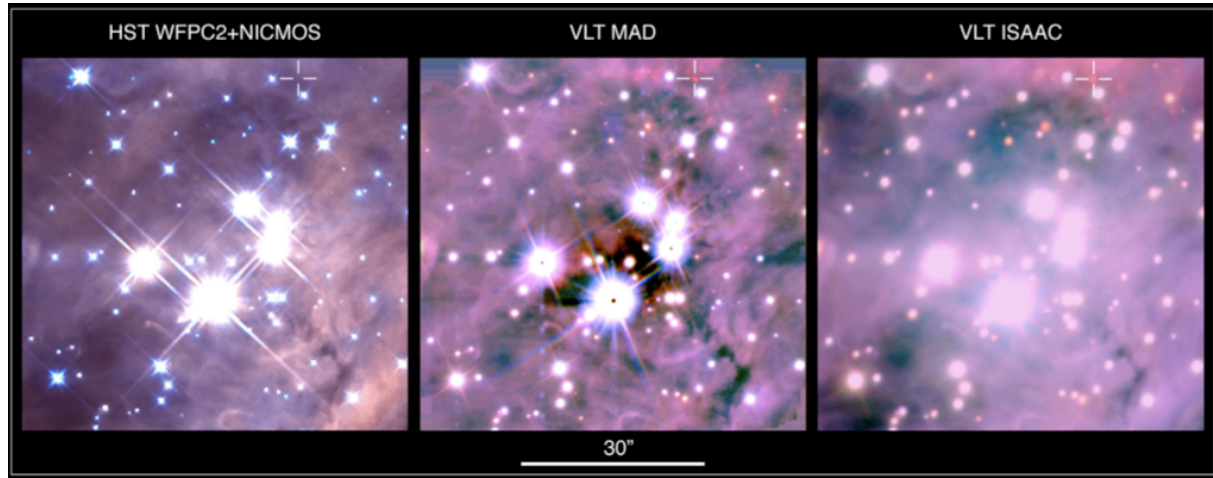


Figure 1.3. Colour images of the trapezium taken with HST (left) and the near infrared with MCAO (center) and conventional AO (right) on the VLT. (Bouy et al. 2008).

The primary aim of these lectures will be to explore the physical principles and mathematical theory behind this technology. For more theoretical detail, the reader is referred to the comprehensive review by Francois Roddier (1981). A useful summary of formulae is provided by two SPIE field guides: the Field Guide to Atmospheric Optics (Andrews 2004) and the Field Guide to Adaptive Optics (Tyson & Frazier 2004). For a complete overview of adaptive optics principles, applications and technology, the notes provided by Claire Max (USCS) are ideal. They are available online at <http://www.ucolick.org/~max/289C/>. I also recommend the tutorial by Andrei Tokovinin which can be found at <http://www.ctio.noao.edu/~atokovin/tutorial/intro.html>. There are also several text books on Adaptive Optics such as Hardy (1998), Tyson (1998), Roddier (1999) and Tyson (2000).

We begin with a brief overview of the subject.

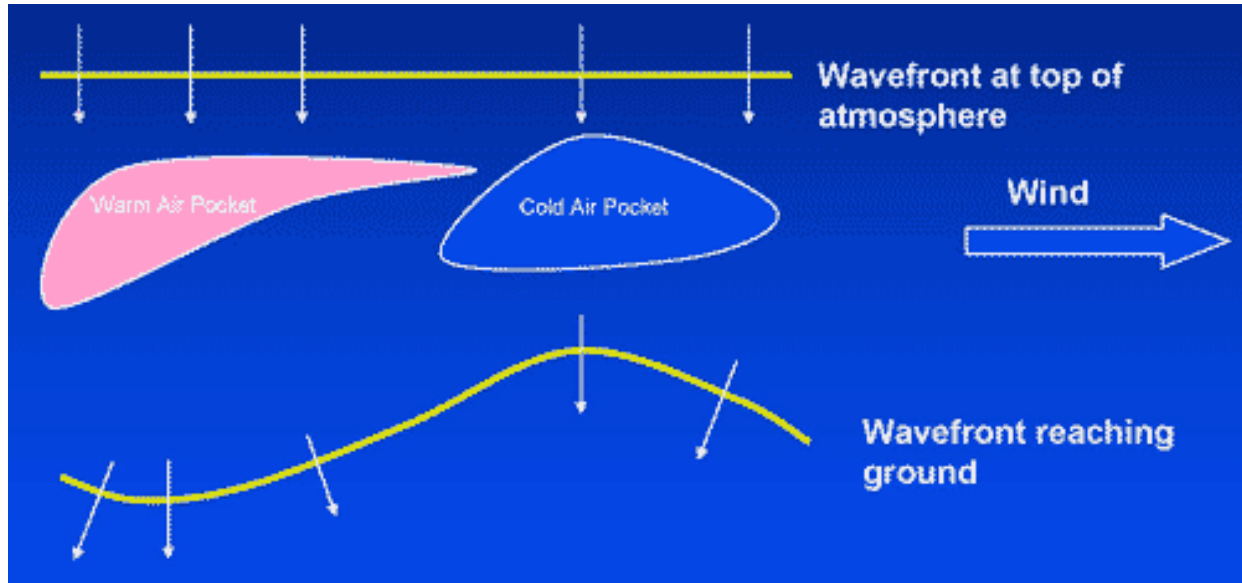


Figure 1.4. Illustration of the development of phase distortion in light propagating through the atmosphere. (Glen Herriot, NRC)

1.1. Atmospheric effects

Light propagating through the atmosphere encounters turbulent regions in which the air temperature, density and index of refraction vary. The variations $n = N - \langle N \rangle$ in index of refraction N result in variations in propagation speed for different rays. Thus, an initially plane wavefront becomes distorted, due to different *optical path lengths* (OPL - the integral of the index of refraction along the ray) for different points on the wavefront (Figure 1.3). This OPL variation is practically (but not exactly) independent of wavelength for visible and infrared light.

As the light propagates, effects of the turbulent regions accumulate, so by the time that the wavefront reaches the ground it has developed a random phase error

$$\varphi = \frac{2\pi}{\lambda} \int n ds \quad (1.1)$$

that varies with position on the wavefront. The mean square phase difference between two points on the wavefront depends on the separation between the two points, increasing in proportion to the separation to the $5/3$ power over a wide range of scales,

$$\mathcal{D}_\varphi(r) \equiv \langle [\varphi(0) - \varphi(r)]^2 \rangle \simeq 6.88 (r/r_0)^{5/3}. \quad (1.2)$$

Here $\mathcal{D}_\varphi(r)$ is called the *phase structure function* and r_0 is a characteristic length called the *Fried parameter* (the origin of the numerical factor will be explained in Section 4.4).

The Fried parameter characterizes the degree of turbulence that is present. Clearly, a large value of r_0 is desirable as that corresponds to *less* phase error at any given scale. From Eqn. (1.2) one can show that the rms phase error averaged within a circle of radius r_0 is approximately one radian,

It follows from Eqns. (1.1) and (1.2) that the Fried parameter varies with wavelength,

$$r_0 \propto \lambda^{6/5}. \quad (1.3)$$

A typical value at a good astronomical site is $r_0 \approx 0.1$ m at a wavelength of 0.5 um.

1.1.1. Seeing

Atmospheric *seeing* refers to image blurring caused by random phase distortion of the wavefronts entering a telescope. This blurring results from a combination of imperfect focussing of rays due to wavefront distortion, and random motion of the image due to varying wavefront tilt.

In a small telescope, with aperture diameter $D \lesssim r_0$, image motion dominates. The instantaneous image is nearly diffraction limited (because the phase error on scales less than r_0 is small) and has a full-width at half maximum intensity (FWHM) of

$$\vartheta \simeq 1.029 \lambda/D. \quad (1.4)$$

The position of this image fluctuates, with a displacement that is roughly Gaussian distributed with characteristic width

$$\vartheta_t \approx \lambda D^{-1/6} r_0^{-5/6}. \quad (1.5)$$

In a large telescope, with aperture $D \gg r_0$, the instantaneous image has a roughly Gaussian intensity distribution with FWHM

$$\vartheta_K \approx \lambda/r_0. \quad (1.6)$$

Image motion is less significant, decreasing with diameter as $D^{-1/6}$ according to Eqn. (1.5).

1.1.2. Scintillation

As light propagates, the local energy flow is in the direction perpendicular to the wavefront. If the wavefront is distorted, this leads to variations in the intensity at any position on the wavefront. These intensity fluctuations grow with distance, even when the light propagates through regions that have no turbulence. As the turbulent cells are carried with the wind, the intensity seen by a fixed observer on the ground will vary with time. This is called **scintillation**, and is the reason that stars appear to twinkle.

A characteristic timescale for these variations is

$$\tau_0 \approx r_0/\bar{v}, \quad (1.7)$$

where \bar{v} is a characteristic wind speed. Typically, τ_0 is a few millisecond at a wavelength of 0.5 um.

Since intensity fluctuations grow with propagation distance, turbulent layers high in the atmosphere make the greatest contribution to scintillation.

1.1.3. Speckles

Interference between light propagating from different points on the distorted wavefront produces luminous **speckles** in the focal plane of the telescope. These can be seen in short-exposure images of bright stars (Figure 1.5). The characteristic angular size of these speckles is the diffraction limit of the telescope $\vartheta \approx \lambda/D$.

1.2. Adaptive Optics (AO)

Adaptive optics systems improve image quality by sensing and correcting the phase distortion introduced by the atmosphere. This is done by an opto-mechanical system that includes a wavefront sensor, one or more deformable mirrors and a control system.

A simplified diagram of a basic AO system is shown in Figure 1.6. Light from a reference source, such as a star, bounces off a deformable mirror and a portion enters a wavefront sensor (WFS). The WFS measures the departure of the wavefront from a plane wave. From this the control system generates a correction signal which moves the deformable mirror, reducing the error. The cycle continues until the wavefront error (WFE) is reduced to a limit imposed by noise. Most of the light leaving the deformable mirror is refocussed onto a detector (the “science camera”). When the loop is closed, the image of the reference star, and those of all objects near it, are corrected.

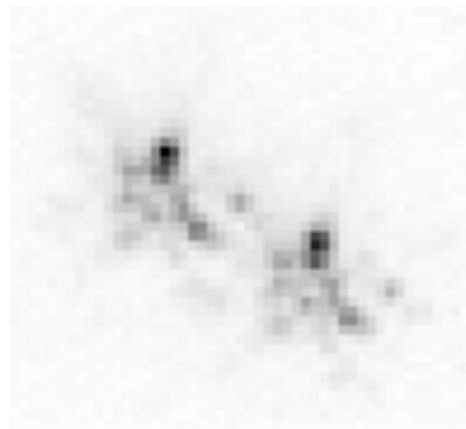


Figure 1.5. Short-exposure of the binary star Zeta Bootes showing identical speckle patterns. (Nordic Optical Telescope)

Image quality that approaches the diffraction limit is possible, and has been achieved at near-infrared (NIR) wavelengths.

A useful measure of the performance of the AO system is the *Strehl ratio* S . This is defined to be the ratio of the central intensity of the image of a point source to that which would be produced by a perfect diffraction-limited telescope having the same aperture and throughput.

It follows that the maximum value that the Strehl ratio can take is 1.0. Current AO systems have produced Strehl ratios as high as 0.5.

1.2.1. Natural guide star adaptive optics (NGAO)

The simplest form of adaptive optics uses light from a star to sense the atmospheric phase distortion. This works well as long as the star is sufficiently bright. Otherwise, photon noise limits the performance. Good results have been obtained at NIR wavelengths using natural guide stars (NGS) as faint as 15th magnitude.

The image quality (eg. the Strehl ratio) degrades as a function of angular distance from the reference star. This is because the light from an object separated from the reference star does not follow exactly the same path through the atmosphere as the light from the reference star (see Figure 1.6).

The angular radius that characterizes the region of good correction is the *isoplanatic angle* θ_0 , defined to be the angle for which the rms wavefront phase error has increased by 1 radian. The isoplanatic angle depends primarily on the strength of the high-level turbulence where the difference between optical paths is greatest. Like r_0 , it increases with wavelength,

$$\theta_0 \propto \lambda^{6/5} \quad (1.8)$$

The isoplanatic angle is typically on the order of 2 arcsec at a wavelength of 0.5 um.

The need to have a relatively bright star within a few arcsec of the object of interest limits the sky coverage of NGAO systems to regions around bright star-like objects. For some science programs this is not a serious limitation. Examples are the study of objects near stars (eg. giant planets or dwarf companions) and active galactic nuclei, where the bright nucleus can be used as the reference.

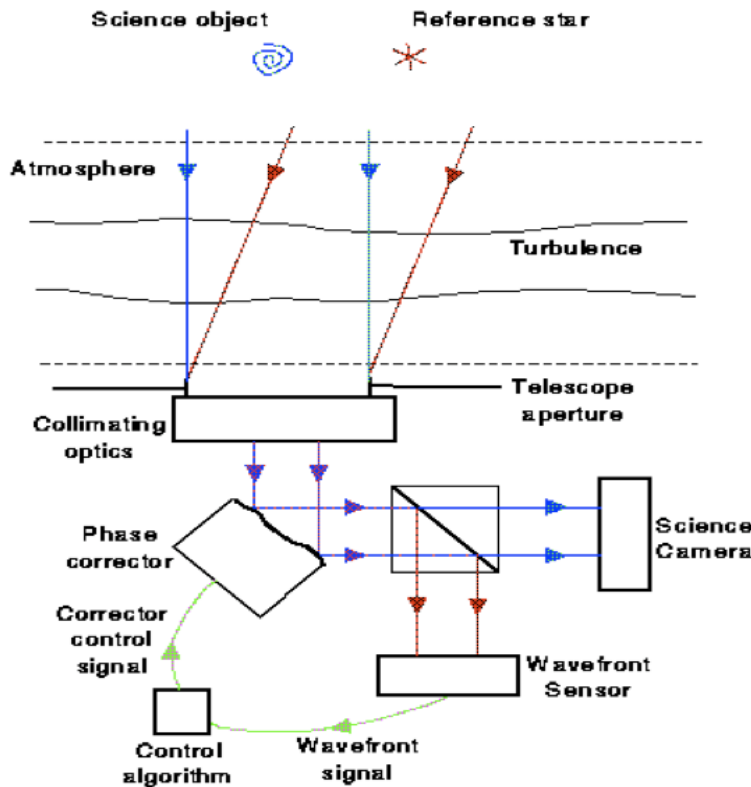


Figure 1.6. Block diagram of a simple AO system. (David Carter, Liverpool John Mores University)

1.2.2. Laser guide star adaptive optics (LGAO)

To overcome the limited sky coverage of NGAO, laser-guide-star adaptive optics systems (LGAO) have been developed. In these systems, a powerful laser is used to create an artificial reference “star” or *beacon* in the atmosphere (Figure 1.7). The great advantage of these systems is that the reference beacon can be created in any direction, so the sky coverage of LGAO systems is much larger than that of NGAO.

Two types of laser beacons are presently employed. The first uses light scattered by molecules in the lower atmosphere. As the predominant scattering process is Rayleigh scattering, these are referred to as Rayleigh systems.

The Rayleigh scattering is confined to the lower ~ 30 km of atmosphere, where the density is greatest. Most of the returned photons come from the lower 15 km.

The second type of system uses a more complex laser that can be tuned to the D₂ resonance line of atomic sodium, at 589 nm wavelength. The laser light then excites sodium atoms in the mesospheric sodium layer, some 90 km above sea level. The excited sodium atoms relax by radiation light at 589 nm, which appears as a *laser guide star* (LGS).

1.2.3. Multi-conjugate (MCAO)

Multi-conjugate adaptive optics (MCAO) systems provide a solution to the problem of the small isoplanatic angle. This is done by employing multiple laser beacons, and more than one deformable mirror.

As Figure 1.8 illustrates, by using multiple laser beacons, each with its own wavefront sensor, one can obtain information about atmospheric turbulence over a greater angle of sky. By locating a second



Figure 1.7. Lasers in use on Mauna Kea. This view from the Subaru telescope shows (from left to right) the 10-m Keck telescopes, the 3.6-m Canada-France-Hawaii telescope, the 8-m Gemini telescope and the University of Hawaii 2.2-m telescope. (Courtesy Chuck Steidel, CIT)

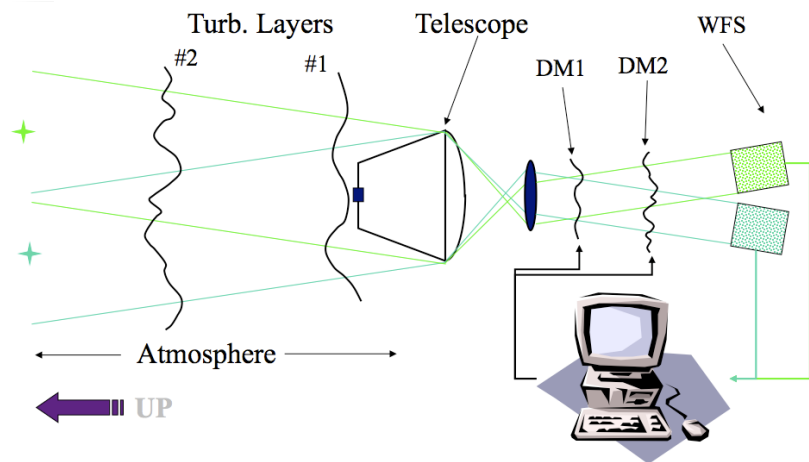


Figure 1.8. The MCAO concept. By sensing and canceling turbulence at several altitudes, correction is extended over a wide angular range. (Gemini Observatory)

DM at a position that is optically conjugate to the high-altitude turbulence layer (the first being conjugate to the ground layer), the size of the isoplanatic region can be greatly extended.

1.2.4. Multi-object (MOAO)

A third type of AO system, illustrated in Figure 1.10, uses a separate DM for each science target. These are placed within probes that can be moved to any position in the field. The DMs operate in open loop mode (no feedback) applying a correction that is computed from WFS measurements of multiple NGS or LGS.

The main advantage of this type of system is that a wide accessible field of view (**field of regard**) is possible.

1.2.5. Ground-layer (GLAO)

A fourth type of AO system uses a single DM, conjugated to the ground layer, to provide partial correction (not diffraction-limited) of images over a wide field of view.

GLAO systems use multiple LGS, spanning the field of view, each with its own WFS. From the phase errors measured by each WFS, an average correction is computed and sent to the DM. The result is a significant degree of image sharpening that would increase the sensitivity of multi-object spectroscopy.

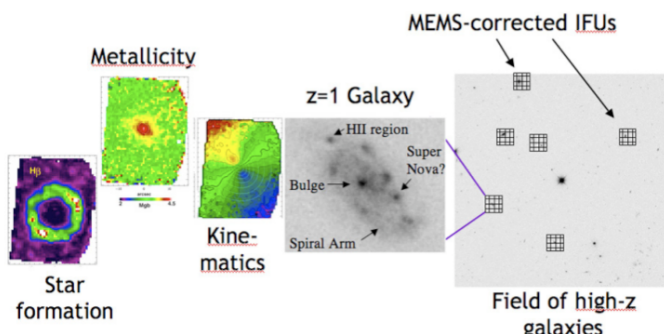


Figure 1.10. MOAO. With multiobject adaptive optics, wavefront correction is done only at the locations of specific targets. In this case an integral field spectrograph (IFU) is provided for each object, and includes a MEMS deformable mirror for correction of the local wavefront. This correction is done in open loop using an estimate provided by tomography. (Credit: Clair E. Max, UCSC)

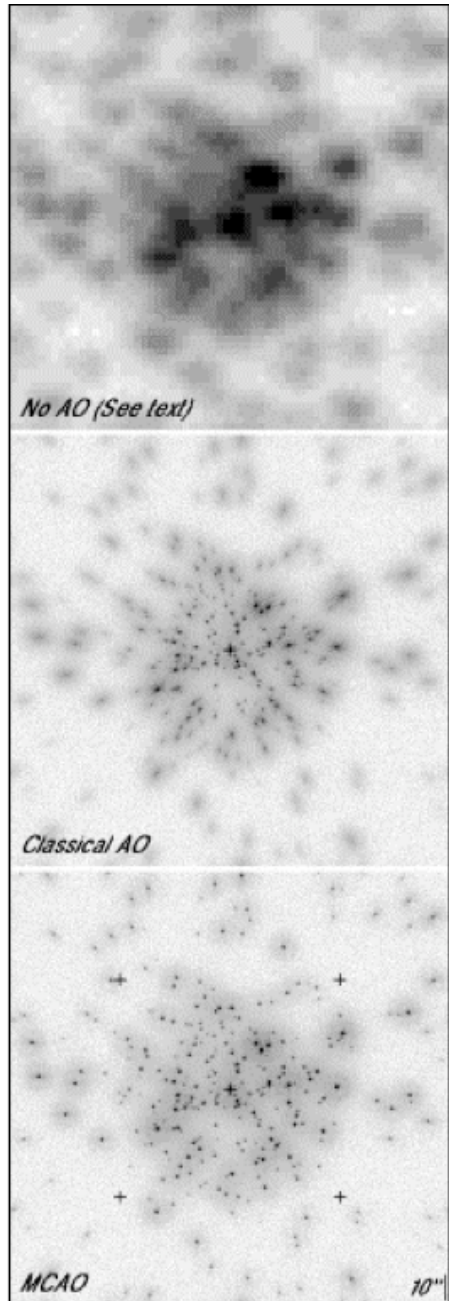


Figure 1.9. Simulation comparing classical and MCAO systems. The classical system employs a single guide star at the center of the field, with noticeable anisoplanatism. The MCAO system employs two DMs and four LGS located at the crosses. The image quality is much more uniform. (Gemini Observatory)

2. Mathematical preliminaries

Before proceeding further, we will need some tools to describe fluctuating quantities. Let $q(\mathbf{r})$ represent a quantity, temperature for example, measured at position \mathbf{r} at some particular time. If we measure again at the same position but a later time, the value will generally be different.

2.1. Probability distribution

The **distribution** f_q of a fluctuating quantity q is a function proportional to the probability that a particular value of q will occur, normalized so that the integral over all possible values is unity. This is also called the **frequency function** of q . Thus, $f_q(q) dq$ is the probability that a measurement will yield a value of q within the interval dq .

If the fluctuating quantity results from the actions of many independent effects, the distribution approaches a Gaussian distribution

$$f_q = (2\pi\sigma_q^2)^{-1/2} \exp[-(q - \langle q \rangle)^2 / 2\sigma_q^2]. \quad (2.1)$$

The parameter σ_q is the **standard deviation** of q and σ_q^2 is the **variance**. This very useful result is called the **central limit theorem**.

If the frequency function of a variable is a Gaussian, the function is said to have a **normal** distribution.

If the frequency function of the logarithm of a variable is a Gaussian, the function is said to have a **lognormal** distribution.

The **ensemble average** $\langle \rangle$ of a fluctuating quantity is the average of many **statistically independent** (ie. uncorrelated) measurements.

2.2. Autocorrelation and covariance

Let's now consider the statistical properties of a field $q(\mathbf{r})$. The **autocorrelation** function of $q(\mathbf{r})$ is defined by

$$\mathcal{R}_q(\mathbf{r}) \equiv \int q(\mathbf{r}') q(\mathbf{r} + \mathbf{r}') d^n r'. \quad (2.2)$$

Here n denotes the number of dimensions, which is normally 1, 2 or 3, and the range of integration is assumed to be infinite. The coordinate \mathbf{r} represents position, however the same functions can also be defined for the time domain.

There is a problem with this definition if $q(\mathbf{r})$ is nonzero over an infinite range. In that case $q(\mathbf{r})$ is said to be a **stochastic process**, and the integral may not converge. For such fields, we use the alternative definition, the autocorrelation per unit volume, which does converge,

$$\mathcal{R}_q(x) \equiv \lim_{V \rightarrow \infty} \frac{1}{V} \int_V q(\mathbf{r}') q(\mathbf{r} + \mathbf{r}') d^n r', \quad (2.3)$$

where V denotes an n -dimensional volume.

In many cases, the statistical properties of the field are independent of the coordinates. The field is then said to be *stationary*. In that case, the integration over the volume can be replaced by the ensemble average

$$\mathcal{R}_q(\mathbf{r}) = \langle q(0)q(\mathbf{r}) \rangle. \quad (2.4)$$

For stationary field, the position of the origin $\mathbf{r} = 0$ is arbitrary.

The *covariance* is obtained by subtracting the mean value

$$\begin{aligned} \mathcal{B}_q(\mathbf{r}) &\equiv \langle [q(0) - \langle q \rangle][q(\mathbf{r}) - \langle q \rangle] \rangle \\ &= \mathcal{R}_0(\mathbf{r}) - \langle q \rangle^2. \end{aligned} \quad (2.5)$$

We will generally (but not always!) be dealing with stationary fluctuations whose mean value is zero, for which the autocorrelation and the covariance are equal. If the mean is not zero, we have

2.3. Power spectrum

We define the n -dimensional Fourier transform pair by

$$\begin{aligned} \tilde{q}(\mathbf{f}) &= \int q(\mathbf{r}) \exp(-2\pi i \mathbf{f} \cdot \mathbf{r}) d^n r, \\ q(\mathbf{r}) &= \int \tilde{q}(\mathbf{f}) \exp(2\pi i \mathbf{f} \cdot \mathbf{r}) d^n f, \end{aligned} \quad (2.6)$$

where \mathbf{f} is the *spatial frequency*. We will often use the *wave number* $\boldsymbol{\kappa} = 2\pi\mathbf{f}$, so in terms of this variable, the Fourier transform takes the form

$$\begin{aligned} \tilde{q}(\boldsymbol{\kappa}) &= \int q(\mathbf{r}) \exp(-i\boldsymbol{\kappa} \cdot \mathbf{r}) d^n r, \\ q(\mathbf{r}) &= (2\pi)^{-n} \int \tilde{q}(\boldsymbol{\kappa}) \exp(i\boldsymbol{\kappa} \cdot \mathbf{r}) d^n \boldsymbol{\kappa}. \end{aligned} \quad (2.7)$$

The *power spectrum* of $q(\mathbf{r})$ is defined as the squared modulus of its Fourier transform

$$\Phi_q(\mathbf{f}) \equiv |\tilde{q}(\mathbf{f})|^2. \quad (2.8)$$

Now, the power contained in a given frequency interval must be the same, whether we measure the interval in terms of \mathbf{f} or $\boldsymbol{\kappa}$, so we must have $\Phi_q(\boldsymbol{\kappa}) d^n \boldsymbol{\kappa} = \Phi_q(\mathbf{f}) d^n f$ hence

$$\Phi_q(\boldsymbol{\kappa}) \equiv (2\pi)^{-n} |\tilde{q}(\boldsymbol{\kappa})|^2. \quad (2.9)$$

In the case of a stochastic process, we can use the modified definition,

$$\Phi_q(\boldsymbol{\kappa}) \equiv \lim_{V \rightarrow \infty} \frac{1}{V} \left| \int_V q(\mathbf{r}) \exp(-i\boldsymbol{\kappa} \cdot \mathbf{r}) d^n r \right|^2. \quad (2.10)$$

One can show that for a normally-distributed random process, the statistical properties are *entirely* determined by the power spectrum. It contains all the statistical information about the process.

2.4. Wiener-Khinchine theorem

An important result is the **Wiener-Khinchine theorem**, which states that the power spectrum equals the Fourier transform of the autocorrelation function

$$\Phi_q(\mathbf{f}) = \int \mathcal{R}_q(\mathbf{r}) \exp(-2\pi i \mathbf{f} \cdot \mathbf{r}) d^n r, \quad (2.11)$$

Thus

$$\Phi_q(\boldsymbol{\kappa}) = (2\pi)^{-n} \int \mathcal{R}_q(\mathbf{r}) \exp(-i\boldsymbol{\kappa} \cdot \mathbf{r}) d^n r. \quad (2.12)$$

2.5. Structure function

The structure function $D_q(\mathbf{r})$ is defined by

$$\mathcal{D}_q(\mathbf{r}) = \langle [q(\mathbf{r}) - q(0)]^2 \rangle. \quad (2.13)$$

By expanding the square, and employing the linearity of the ensemble average, one finds

$$\begin{aligned} \mathcal{D}_q(\mathbf{r}) &= \langle q(\mathbf{r})^2 \rangle + \langle q(0)^2 \rangle - 2\langle q(\mathbf{r})q(0) \rangle, \\ &= 2\mathcal{R}_q(0) - 2\mathcal{R}_q(\mathbf{r}), \\ &= 2\mathcal{B}_q(0) - 2\mathcal{B}_q(\mathbf{r}). \end{aligned} \quad (2.14)$$

The last equality follows from Eqn. (2.5).

3. Atmospheric turbulence

In this section we review the most important elements of the theory and observations of atmospheric turbulence.

3.1. Kolmogorov turbulence

Kolmogorov and Obukhov (1941) developed a theory of turbulence based on scaling arguments. They supposed that turbulence is generated on some large **outer scale** L_0 , and progresses to smaller and smaller scales as large vortices transfer energy to small vortices. When this energy cascade reaches a sufficiently small **inner scale** l_0 , viscous forces result in dissipation of the energy into heat (Figure 3.1).

The range between the inner scale and the outer scale is called the **inertial range**. Here the velocities are generally **isotropic** (ie. they have no preferred direction) and there is a well-developed relationship between energy and scale.

Let \mathcal{E} be the rate at which energy is dissipated, per unit mass, at the inner scale. In equilibrium, this must equal the rate at which energy is injected at the outer scale, and must also be proportional to the energy flux passing from larger to smaller scales.

Let $v(l)$ characterize the turbulent velocity on a scale l . In the inertial range, viscous effects are not important, so this can depend only on the energy flux \mathcal{E} , and the scale l . The only combination of these two factors that has the dimension of velocity is

$$v \propto (\mathcal{E}l)^{1/3}. \quad (3.1)$$

Thus, the velocity variation over a small distance is proportional to the cube root of the distance.

In a similar manner, one can consider energy in the Fourier domain. Since the turbulence is isotropic, the turbulent energy at wave number $\kappa \sim 2\pi/l$, in the range $d\kappa$ depends only on the magnitude κ . From dimensional analysis, we find that the energy per unit mass is

$$E(\kappa) d\kappa \propto v^2 \propto \kappa^{-2/3}. \quad (3.2)$$

Thus,

$$E(\kappa) \propto \kappa^{-5/3}, \quad (3.3)$$

which is known as **Kolmogorov's law**. It is useful to write this in terms of a three-dimensional spectral density $E(\vec{\kappa})$. (In this and subsequent sections, we shall use an overhead arrow to denote a three-

dimensional quantity, and bold face to denote a two-dimensional quantity.) This is related to the one-dimensional density by the relation

$$E(\kappa) d\kappa = E(\vec{\kappa}) d^3 \kappa = 4\pi E(\vec{\kappa}) \kappa^2 d\kappa \quad (3.4)$$

Thus,

$$E(\vec{\kappa}) \propto \kappa^{-11/3}. \quad (3.5)$$

On large scales, the air will invariably contain regions of different temperatures. Turbulent mixing will result in eddies of different temperatures. These small temperature fluctuations do not affect the dynamics of the turbulence, but are simply carried along by it. As a result, the power spectrum of temperature fluctuations also follows Kolmogorov's law (Obukhov 1949, Yaglom 1949),

$$\Phi_T(\vec{\kappa}) \propto \kappa^{-11/3}. \quad (3.6)$$

3.2. Index of refraction fluctuations

The index of refraction of air depends on its temperature and humidity. For astronomical sites, temperature is by far the dominant factor. Fluctuations in index of refraction N are related to fluctuations of temperature by

$$n \equiv N - \langle N \rangle \simeq 7.76 \cdot 10^{-9} PT^{-2} (T - \langle T \rangle), \quad (3.7)$$

where P is the atmospheric pressure in Pa and T is the absolute temperature in K.

Since the index of refraction fluctuation is proportional to the temperature fluctuation, its power spectrum (in the inertial range) is given by Kolmogorov's law

$$\Phi_n(\vec{\kappa}) = A \kappa^{-11/3}, \quad (3.8)$$

where A is a proportionality constant. Applying the inverse Fourier transform to Eqn (2.12), and recalling that the index of refraction fluctuations have zero mean, we find

$$\mathcal{B}_n(\vec{r}) = \mathcal{R}_n(\vec{r}) = \int \Phi_n(\vec{\kappa}) \exp(i\vec{\kappa} \cdot \vec{r}) d^3 \kappa. \quad (3.9)$$

However, because the power spectrum of Eqn (3.7) is infinite at the origin, the integral diverges. Fortunately, the structure function is finite,

$$\begin{aligned} \mathcal{D}_n(\vec{x}) &= 2 \int \Phi_n(\vec{\kappa}) [1 - \exp(i\vec{\kappa} \cdot \vec{r})] d^3 \kappa, \\ &= 8\pi A \int_0^\infty [1 - \sin(\kappa r)/(\kappa r)] \kappa^{-5/3} d\kappa, \\ &= 4\pi \Gamma(-5/3) A r^{2/3}. \end{aligned} \quad (3.10)$$

It is conventional to label the coefficient in Eqn. (3.10) C_N^2 , the index of refraction **structure constant**. Thus,

$$\mathcal{D}_n(r) = C_N^2 r^{2/3}. \quad (3.11)$$

From this we see that the rms index of refraction fluctuation between two points (the square root of $\mathcal{D}_n(r)$) increases in proportion to distance to the 1/3 power.

The stucture constant is a function of height. Typical values range from $10^{-14} \text{ m}^{-2/3}$ near the ground to $10^{-17} \text{ m}^{-2/3}$ at an altitude of $\sim 10 \text{ km}$.

3.3. Kolmogorov spectrum

Comparing Eqns (3.9) and (3.10) we see that

$$\begin{aligned} A &= \frac{1}{4\pi\Gamma(-5/3)} C_N^2, \\ &\simeq 0.0330054 C_N^2. \end{aligned} \quad (3.12)$$

Thus, in the inertial range we have the Kolmogorov spectrum

$$\Phi_n(\vec{k}) \simeq 0.033 C_N^2 k^{-11/3}. \quad (3.13)$$

3.4. Von Karman spectrum

A generalization of Eqn (3.13) that incorporates the outer scale was suggested by von Karman.

$$\Phi_n(\vec{k}) \simeq 0.033 C_N^2 (k^2 + k_0^2)^{-11/6}. \quad (3.14)$$

A second form that also includes the inner scale is the *modified von Karman spectrum*,

$$\Phi_n(\vec{k}) \simeq 0.033 C_N^2 (k^2 + k_0^2)^{-11/6} \exp(-k^2/k_m^2), \quad (3.15)$$

where $k_0 = 2\pi/L_0$ and $k_m = 5.92/l_0$. This clearly reduces to the Kolmogorov spectrum in the inertial range. At low frequencies it approaches a constant.

3.5. Taylor frozen flow hypothesis

At any given instant, the pattern of phase distortion in light reaching the ground is determined by the turbulence structure in the light path. As time goes on, the turbulence pattern changes, and so does its optical effect.

To a good approximation, most of the change comes because wind carries the pattern of turbulence downstream. Compared to this, the intrinsic change in the structure of the turbulence is relatively slow. Also, the wind direction is predominantly horizontal, varying slowly with horizontal distance and more rapidly with height.

Thus, to a first approximation, the index of refraction structure, at a particular height, at a given time is simply related to the pattern at an earlier time, shifted by distance that equals the wind velocity times the time interval,

$$n(\mathbf{r}, h, t) = n(\mathbf{r} - \mathbf{v} \Delta t, h, t - \Delta t). \quad (3.16)$$

(Here we are using bold face symbols to indicate two-dimensional vectors in the horizontal plane.) This is called the *Taylor frozen flow hypothesis*. It allows one to relate *temporal fluctuations* to *spatial fluctuations*.

3.6. Vertical structure

The effect of the atmosphere on image quality, and adaptive optics, is determined almost entirely by

- the turbulence profile as a function of altitude, or height above the observatory
- the wind velocity as a function of altitude

It is therefore of great importance to determine these parameters as well as possible when considering a site for a telescope, or when designing an AO system. This is a primary goal of site testing campaigns.

3.6.1. Planetary boundary layer

It is found that turbulence is strongest near the ground, decreasing roughly exponentially with height in the lower few km of the atmosphere. This region is the *planetary boundary layer*.

3.6.2. Shear zones

In addition, one or more layers of strong turbulence are found to exist at high altitudes, on the order of 10 - 20 km. These are due to turbulence created by wind shear, possibly associated with the jet stream. These layers are generally quite narrow. Collectively they are referred to as *high-altitude turbulence*.

3.6.3. Cerro Pachon model

A widely-used model of the atmosphere is the Cerro Pachon model (Tokovinin and Travouillon 2006), determined by a campaign of site testing using balloon soundings, SODAR, scintillometers and differential image motion monitors. The typical boundary layer profile is represented by a double exponential

$$C_N^2(h) = A_0 \exp(-h/h_0) + A_1 \exp(-h/h_1), \quad (3.17)$$

with parameters given in Table 3.1. The table also lists median values of the turbulence integral

$$\mathcal{J} = \int C_N^2(h) dh \quad (3.18)$$

for the ground layer \mathcal{J}_{GL} (corresponding to the range 6 - 500 m) and the high altitude (“free atmosphere”) \mathcal{J}_{FA} (corresponding to the atmosphere above 500m).

Table 3.1. The median Cerro Pachon model

A_0	h_0	A_1	h_1	\mathcal{J}_{GL}	\mathcal{J}_{FA}
$4.5 \cdot 10^{-15} \text{ m}^{-2/3}$	30 m	$5 \cdot 10^{-17} \text{ m}^{-2/3}$	500 m	$2.7 \cdot 10^{-13} \text{ m}^{1/3}$	$1.5 \cdot 10^{-13} \text{ m}^{1/3}$

4. Propagation of light through a turbulent medium

So far, we have reviewed the statistical properties of index of refraction fluctuations in the atmosphere. In this section we examine their effect on the propagation of light. We shall assume that the wavefronts are initially plane. This is equivalent to the assumption that the distance to the source is much greater than the scale of turbulent eddies. We shall also assume that the turbulence is isotropic.

We use conventional astronomical definitions of radiative quantities. **Irradiance** is the radiant flux in the propagating beam, measured in Wm^{-2} . **Intensity** is flux per unit solid angle, measured in $\text{Wm}^{-2}\text{sr}^{-1}$. As long as photons are not absorbed or emitted, intensity remains constant throughout an optical system. Irradiance will change if the beam diameter changes, as required to by conservation of energy.

4.1. Wave propagation

Isotropic turbulence has no preferred direction, so there is no effect on the polarization of light. Therefore, we can use a scalar treatment of wave propagation. We use arrows to indicate three-dimensional vectors and bold face to indicate two dimensional vectors in the plane perpendicular to the direction of propagation.

The complex amplitude of the electric field $E(\vec{r}, t) = E(\mathbf{r}, z, t)$ satisfies the scalar wave equation

$$\nabla^2 E - \frac{N^2}{c^2} \frac{\partial^2 E}{\partial t^2} = 0, \quad (4.1)$$

where c is the speed of light in vacuum and $N(\mathbf{r}, z) \simeq 1 + n(\mathbf{r}, z)$ is the index of refraction (Section 3.2).

The substitution

$$E = \psi(\vec{r}) \exp[i(\mathbf{k} \cdot \mathbf{r} - \omega t)], \quad (4.2)$$

where $k \equiv |\mathbf{k}| = 2\pi/\lambda = \omega/c$, gives

$$\nabla^2 \psi + 2ik \frac{\partial \psi}{\partial z} = -2k^2 n \psi. \quad (4.3)$$

The Laplacian can be separated into transverse and longitudinal terms to give

$$\nabla_{\perp}^2 \psi + \frac{\partial^2 \psi}{\partial z^2} + 2ik \frac{\partial \psi}{\partial z} = -2k^2 n \psi. \quad (4.4)$$

If we assume that the amplitude changes slowly as the wave propagates, with significant changes occurring over a distance $L \gg \lambda$, the second term in Eqn. (4.4) will be smaller than the third by a factor of $(kL)^{-1} \ll 1$ and can be neglected. Omitting this term, we obtain

$$\frac{i}{k} \frac{\partial \psi}{\partial z} = -\left(\frac{1}{2k^2} \nabla_{\perp}^2 + n\right) \psi \equiv \mathcal{H}(\mathbf{r}, z) \psi. \quad (4.5)$$

Eq. (4.5) can be recognized as the Schrodinger equation in two dimensions. Here the coordinate z plays the role of time, and the wavelength λ is equivalent to Planck's constant h . The operator \mathcal{H} plays the role

of the Hamiltonian and acts to propagate the amplitude in the z direction. The index of refraction acts like a time-varying potential $V(\mathbf{r}, z) = -n(\mathbf{r}, z)$.

Eqn. (4.5) has the formal solution

$$\psi(z) = \psi(0) + \sum_{p=1}^{\infty} (ik)^p \int_0^z dz_0 \int_0^{z_0} dz_1 \cdots \int_0^{z_{p-2}} dz_{p-1} \exp[i(z-z_0)\nabla_{\perp}^2/2k] n_0 \\ \exp[i(z_0-z_1)\nabla_{\perp}^2/2k] n_1 \cdots \exp[i(z_{p-2}-z_{p-1})\nabla_{\perp}^2/2k] n_{p-1} \psi(0). \quad (4.6)$$

where $\psi(0)$ is the initial amplitude. Here we have introduced the notation $n_j = n(\mathbf{r}, z_j)$.

The first term in the summation can be interpreted as the amplitude change produced by a single scattering from an index of refraction fluctuation located at distance z_0 . The second term corresponds to two scatterings, the third term to three and so on.

Eqn. (4.6) can be written in terms of the two-dimensional Fourier coefficients of the index of refraction fluctuations \tilde{n} . We take the initial amplitude to be unity, $\psi(0) = 1$. The result is

$$\psi(\mathbf{r}, z) = \sum_{p=0}^{\infty} \left(\frac{ik}{4\pi^2} \right)^p \int_0^z dz_0 \int_0^{z_0} dz_1 \cdots \int_0^{z_{p-2}} dz_{p-1} \int d^2 \boldsymbol{\kappa}_0 \cdots \int d^2 \boldsymbol{\kappa}_{p-1} \\ \exp(-i\{(z-z_0)[\boldsymbol{\kappa}_0^2 + 2\boldsymbol{\kappa}_0 \cdot (\boldsymbol{\kappa}_1 + \cdots + \boldsymbol{\kappa}_{p-1})] + (z-z_1)[\boldsymbol{\kappa}_1^2 + 2\boldsymbol{\kappa}_1 \cdot (\boldsymbol{\kappa}_2 + \cdots + \boldsymbol{\kappa}_{p-1})^2] + \cdots + (z-z_{p-1})\boldsymbol{\kappa}_{p-1}^2\}/2k + i\mathbf{r} \cdot (\boldsymbol{\kappa}_0 + \cdots + \boldsymbol{\kappa}_{p-1})) \tilde{n}_0 \cdots \tilde{n}_{p-1}. \quad (4.7)$$

With this solution, we are now able to compute the statistics of the radiation field at any distance z along the line of sight. However, one more assumption is needed. We assume that the propagation distance is large compared to the distance over which the index of refraction fluctuations are correlated (ie the turbulence scale). This is called the **Markov approximation**. It allows us to write the ensemble average of products of index of refraction Fourier components in terms of the power spectrum

$$\langle \tilde{n}(\boldsymbol{\kappa}_j, z_j) \tilde{n}^*(\boldsymbol{\kappa}_k, z_k) \rangle \approx (2\pi)^5 \Phi(\boldsymbol{\kappa}_j, z_j) \delta(\boldsymbol{\kappa}_j - \boldsymbol{\kappa}_k) \delta(z_j - z_k). \quad (4.8)$$

The delta function over $\boldsymbol{\kappa}$ appears because the Fourier components of independent random fluctuations are uncorrelated. These delta functions greatly simplify the calculation of the integrals in Eqn. (4.7).

Finally, we make use of the following property of Gaussian fluctuations,

$$\langle \tilde{n}_1 \tilde{n}_2 \cdots \tilde{n}_k \rangle = \langle \tilde{n}_1 \tilde{n}_2 \rangle + \langle \tilde{n}_1 \tilde{n}_3 \rangle + \langle \tilde{n}_2 \tilde{n}_3 \rangle + \cdots, \quad (4.9)$$

where the sum extends over all possible combinations of pairs of fluctuations.

4.2. Coherence functions

Let's now calculate some statistical properties of the radiation field.

4.2.1. Mean field

The simplest quantity of interest is the **mean field** $\langle \psi(z) \rangle$. Applying Eqns. (4.6), (4.7), (4.8) and (4.9) and summing the resulting series, one obtains

$$\langle \psi(r, z) \rangle = \exp \left[-2\pi^2 k^2 \int_0^z dz_0 \int_0^\infty \Phi(\kappa, z_0) \kappa d\kappa \right]. \quad (4.10)$$

The integral is infinite for the Kolmogorov spectrum. For the von Karman spectrum, Eqn. (3.14), the result is

$$\langle \psi(r, z) \rangle = \exp \left[-0.361 \lambda^{-2} L_0^{5/3} \int_0^z C_N^2(z_0) dz_0 \right]. \quad (4.11)$$

From this we see that the light gradually loses coherence as more and more light is diffracted by the index of refraction fluctuations. For propagation through the atmosphere, the mean field at ground level at optical and near-infrared wavelengths is virtually zero.

4.2.2. Mutual coherence

Of more interest is the ***mutual coherence***, defined by

$$\Gamma_2(\mathbf{r}_1, \mathbf{r}_2, z) = \langle \psi(\mathbf{r}_1, z) \psi^*(\mathbf{r}_2, z) \rangle \quad (4.12)$$

For isotropic turbulence, this is a function only of the separation $r = |\mathbf{r}_1 - \mathbf{r}_2|$. Again using Eqns. (4.6), (4.7), (4.8) and (4.9), we obtain

$$\Gamma_2(\mathbf{r}_1, \mathbf{r}_2, z) = \exp \left[-4\pi^2 k^2 \int_0^z dz_0 \int_0^\infty \Phi(\kappa) [1 - J_0(\kappa r)] \kappa d\kappa \right]. \quad (4.13)$$

Note that when $r = 0$, we have $\Gamma_2(0, z) = \langle \psi \psi^* \rangle = \langle I \rangle = 1$, which states that the average irradiance I does not change. This is a statement of conservation of energy - the photons are scattered but not absorbed, so the mean number of photons per unit area in the wave is conserved.

4.2.3. Fourth-order coherence

The ***fourth-order coherence function*** is defined by

$$\Gamma_4(\mathbf{r}_1, \mathbf{r}_2, \mathbf{r}_3, \mathbf{r}_4, z) = \langle \psi(\mathbf{r}_1, z) \psi^*(\mathbf{r}_2, z) \psi(\mathbf{r}_3, z) \psi^*(\mathbf{r}_4, z) \rangle. \quad (4.14)$$

Of particular interest is the special case $\Gamma_4(\mathbf{r}, z) \equiv \Gamma_4(\mathbf{r}_1, \mathbf{r}_1, \mathbf{r}_2, \mathbf{r}_2, z)$, where $\mathbf{r} = \mathbf{r}_1 - \mathbf{r}_2$.

Unfortunately, calculation of these quantities has proven difficult and no exact closed-form solution has been found despite many years of effort. In the case of weak scintillation we have the first-order solution

$$\Gamma_4(\mathbf{r}, z) = 1 + 8\pi^2 k^2 \int_0^z dz_0 \int_0^\infty \Phi(\kappa, z_0) \{1 - \cos[(z - z_0)\kappa^2/k]\} J_0(\kappa r) \kappa d\kappa + \dots \quad (4.15)$$

The ***covariance function of irradiance*** is defined by

$$\mathcal{B}_I(\mathbf{r}, z) \equiv \mathcal{B}_I(\mathbf{r}_1, \mathbf{r}_2, z) = \frac{\Gamma_4(r_1, r_1, r_2, r_2, z)}{\Gamma_2(\mathbf{r}_1, \mathbf{r}_1, z) \Gamma_2(\mathbf{r}_2, \mathbf{r}_2, z)} - 1. \quad (4.16)$$

To first order this is

$$\mathcal{B}_I(\mathbf{r}, z) = 16\pi^2 k^2 \int_0^z dz_0 \int_0^\infty \Phi(\kappa, z_0) \sin^2[(z - z_0)\kappa^2/2k] J_0(\kappa r) \kappa d\kappa + \dots \quad (4.17)$$

An important special case is the *scintillation index*,

$$\sigma_I^2(z) \equiv \mathcal{B}_I(0, z) = 16\pi^2 k^2 \int_0^z dz_0 \int_0^\infty \Phi(\kappa, z_0) \sin^2[(z - z_0)\kappa^2/2k] \kappa d\kappa + \dots \quad (4.18)$$

4.3. Seeing and scintillation

We now examine the optical effects of the statistical moments described in the previous section.

4.3.1. Phase and amplitude fluctuations

The complex amplitude can be written in terms of phase and log-amplitude fluctuations φ and χ , defined by

$$\psi = \exp(\chi + i\varphi). \quad (4.19)$$

We assume that both φ and χ are Gaussian random variables. The phase φ is equally likely to be positive or negative and so has zero mean, $\langle \varphi \rangle = 0$.

To find the mean value of χ , we note that

$$\Gamma_2(0, z) = \langle \psi \psi^* \rangle = \langle \exp(2\chi) \rangle = 1. \quad (4.20)$$

The last equality follows from Eqn. (4.13). It can be verified by integrating over the probability distributions that for any independent Gaussian random variables f and g , the following equality holds (Fried 1966),

$$\langle \exp(f + g) \rangle = \exp\left\{\langle [f - \langle f \rangle]^2 \rangle / 2 + \langle [g - \langle g \rangle]^2 \rangle / 2 + \langle f \rangle + \langle g \rangle\right\}. \quad (4.21)$$

Applying this to Eqn. (4.20) gives

$$\langle \exp(2\chi) \rangle = \exp(2\langle \chi^2 \rangle + 2\langle \chi \rangle). \quad (4.22)$$

Since this must equal unity, for energy conservation, we have

$$\langle \chi \rangle = -\langle \chi^2 \rangle = -\mathcal{R}_\chi(0). \quad (4.23)$$

Thus,

$$\mathcal{B}_\chi(0) = \mathcal{R}_\chi(0) - \langle \chi \rangle^2 = \mathcal{R}_\chi(0)[1 - \mathcal{R}_\chi(0)]. \quad (4.24)$$

We can now calculate the mean field in terms of phase and log-amplitude fluctuations. Using Eqns. (4.15), (4.21) and (4.23) we obtain

$$\begin{aligned}\langle \psi \rangle &= \exp \left\{ \frac{1}{2} [\langle \chi^2 \rangle - \langle \varphi^2 \rangle] + \langle \chi \rangle \right\}, \\ &= \exp \left\{ -\frac{1}{2} [\mathcal{R}_\chi(0) + \mathcal{R}_\varphi(0)] \right\}.\end{aligned}\quad (4.25)$$

Comparing this with Eqn. (4.10) we find that

$$\mathcal{R}(0) \equiv \mathcal{R}_\chi(0) + \mathcal{R}_\varphi(0) = 4\pi^2 k^2 \int_0^z dz_0 \int_0^\infty \Phi(\kappa, z_0) \kappa d\kappa. \quad (4.26)$$

In the same manner, we can calculate the mutual coherence

$$\begin{aligned}\Gamma_2(\mathbf{r}_1, \mathbf{r}_2, z) &= \langle \exp \{ \chi(r_1) + \chi(r_2) + i[\varphi(r_1) - \varphi(r_2)] \} \rangle, \\ &= \exp \left[-\mathcal{R}_\chi(0) + \mathcal{R}_\chi(r) - \mathcal{R}_\varphi(0) + \mathcal{R}_\varphi(r) \right], \\ &= \exp \left\{ -\frac{1}{2} [\mathcal{D}_\chi(r) + \mathcal{D}_\varphi(r)] \right\}.\end{aligned}\quad (4.27)$$

Comparing this with Eqn. (4.13) we see that

$$\mathcal{D}(r) \equiv \mathcal{D}_\chi(r) + \mathcal{D}_\varphi(r) = 8\pi^2 k^2 \int_0^z dz_0 \int_0^\infty \Phi(\kappa) [1 - J_0(\kappa r)] \kappa d\kappa. \quad (4.28)$$

The function $\mathcal{D}(r)$ is called the *wave structure function*. In astronomical applications, phase fluctuations are generally much larger than log-amplitude fluctuations, so $\mathcal{D}(r) \approx \mathcal{D}_\varphi(r)$.

4.3.2. The Fried parameter

Let's evaluate the structure function for observations through the atmosphere of a target at zenith angle ζ . In this case, distance z along the line of sight is related to the height h by $dz = \sec \zeta dh$.

Substituting the Kolmogorov spectrum, Eqn. (3.13), into Eqn. (4.28) and integrating over κ , we find

$$\begin{aligned}\mathcal{D}(r) &= 0.033 (8\pi^2 k^2) \frac{3\Gamma(1/6)}{10 \cdot 2^{2/3} \Gamma(11/6)} \int_0^\infty C_N^2(z_0) dz_0 r^{5/3}, \\ &\simeq 2.913 k^2 \sec \zeta r^{5/3} \int_0^\infty C_N^2(h) dh.\end{aligned}\quad (4.29)$$

David Fried (1965) introduced the *Fried parameter* r_0 , defined by

$$\mathcal{D}(r) = 6.8839 (r/r_0)^{5/3}, \quad (4.30)$$

where the numerical factor, more precisely given by $2[(24/5)\Gamma(6/5)]^{5/6}$, was chosen in such a way that a telescope of aperture diameter $D = r_0$ has equal contribution to image blur from seeing and diffraction.

Comparing Eqns. (4.29) and (4.30) we see that

$$r_0 = (0.423 k^2 \sec \zeta)^{-3/5}. \quad (4.31)$$

where \mathcal{J} is the turbulence integral defined in Eqn. (3.18).

Eqn. (4.30) shows that the rms phase fluctuations between two points on the wavefront grow in proportion to the $5/6$ power of the separation. r_0 corresponds to the scale at which these fluctuations become large (the rms phase fluctuation is 2.62 radians when $r = r_0$).

From Eqn. (4.31) we see that the Fried parameter is directly related to the turbulence integral \mathcal{J} , and is proportional to the wavelength to the $6/5$ power. Thus the seeing depends only on the integral of C_N^2 along the line of sight, and improves with increasing wavelength.

4.3.3. Atmospheric time constant

An important parameter for adaptive optics is the rate at which the wavefront phase structure changes. This is due primarily to wind that carries the turbulence pattern past the telescope. Consider the effect of a single turbulent layer of infinitesimal thickness δh , moving horizontally with speed v . From Eqn. (4.29) the contribution of this layer to the structure function will be

$$\delta\mathcal{D}(r) \simeq 2.913 k^2 \sec \zeta r^{5/3} C_N^2(h) \delta h. \quad (4.32)$$

Now, by the Taylor hypothesis, this can be converted to a temporal structure function by the substitution $r = vt$. Thus

$$\delta\mathcal{D}(t) \simeq 2.913 k^2 \sec \zeta t^{5/3} v(h)^{5/3} C_N^2(h) \delta h. \quad (4.33)$$

Integrating this over all layers gives

$$\mathcal{D}(t) = 2.913 k^2 \sec \zeta t^{5/3} \int_0^\infty C_N^2 v^{5/3} dh. \quad (4.34)$$

This can be written in the form

$$D_\phi(t) = (t/\tau_0)^{5/3}, \quad (4.35)$$

where

$$\tau_0 = \left(2.913 k^2 \sec \zeta \int_0^\infty C_N^2 v^{5/3} dh \right)^{-3/5}, \quad (4.36)$$

is the atmospheric timescale (Roddier 1981).

4.3.4. Greenwood frequency

The *Greenwood frequency* (Greenwood 1976), is a characteristic frequency, related to τ_0 , defined by

$$f_G = \left(0.102 k^2 \sec \zeta \int_0^\infty C_N^2 v^{5/3} dh \right)^{3/5}. \quad (4.37)$$

Thus

$$f_G = 0.1338/\tau_0. \quad (4.38)$$

The Greenwood frequency is a measure of how fast the AO system must respond. Typically, the closed-loop bandwidth of the AO system is taken to be about ten times the Greenwood frequency (Greenwood & Fried 1976).

4.3.5. The scintillation index

To further explore scintillation, substitute the Kolmogorov spectrum, Eqn. (3.13), into Eqn. (4.18). This gives

$$\sigma_i^2(\mathbf{r}, z) \equiv \mathcal{B}_i(0, z) = 16\pi^2 k^2 \int_0^z dz_0 \int_0^\infty \Phi(\kappa, z_0) \sin^2[(z - z_0)\kappa^2/2k] \kappa d\kappa + \dots. \quad (4.39)$$

Performing the integration over κ , we find that

$$\begin{aligned} \sigma_i^2(z) &= \frac{0.033 \cdot 16 \cdot 3}{10} (3^{1/2} - 1) \cdot 2^{-3/2} \Gamma(1/6) \pi^2 k^{7/6} \int_0^z C_N^2(z_0) (z - z_0)^{5/6} dz_0 + \dots, \\ &\simeq 2.252 k^{7/6} \int_0^z C_N^2(z_0) (z - z_0)^{5/6} dz_0 + \dots. \end{aligned} \quad (4.40)$$

Two special cases are illustrative. Suppose first that the turbulence is confined to a thin layer at $z = 0$. Then from Eqn. (4.40), $\sigma_i^2(z) \propto k^{7/6} z^{5/6}$ and we see that the scintillation index grows as the $5/6$ power of the propagation distance from the layer.

Now suppose that the turbulence is uniform, $C_N^2(z) = \text{constant}$. Again, we can integrate Eqn. (4.40). We find that, to first order, the scintillation index is given by the **Rytov variance** $\sigma_i^2(z) = 1.23 C_N^2 k^{7/6} z^{11/6}$.

As the propagation distance increases, the scintillation index grows, eventually exceeding unity. Numerical calculations indicate that saturation occurs, and eventually the scintillation index begins to decrease due to loss of coherence, reaching a limiting value of 1.0 (Figure 4.1).

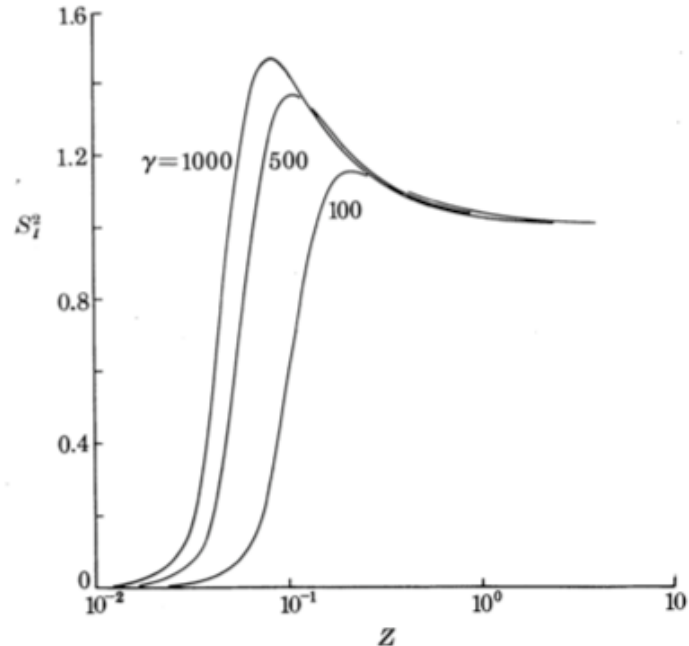


Figure 4.1. Growth of the scintillation index with distance. The parameter γ is related to the turbulence strength. (Uscinski 1982)

5. Imaging theory

In this section we briefly review some important results relating to image formation by telescopes.

5.1. Telescope imaging

5.1.1. Pupils

The purpose of a telescope is to collect and focus light from a distant source, thus forming an image of the source. All telescopes have some sort of aperture that restricts the rays that reach the image. Generally this is the entrance aperture, or telescope primary mirror.

Images of the aperture may be formed by the optical elements of the telescope. For example, in a Cassegrain telescope the secondary mirror forms a virtual image of the primary mirror. In a Gregorian telescope this image is real.

The aperture, or image of the aperture, first encountered by rays entering the telescope is called the *entrance pupil*. For a large telescope, this is usually the primary mirror aperture.

The aperture, or image of the aperture, last encountered by rays before they leave the telescope, or reach the final focus, is called the *exit pupil*.

Two points, or planes perpendicular to the axis of the telescope, are said to be *optically conjugate* if light from one is focussed to the other. In other words, an object is optically conjugate to its image. It follows that all pupils are optically conjugate to each other.

5.1.2. Fourier optics

Consider a wavefront reaching the entrance pupil \mathcal{A} of a perfect telescope. If the wavefront is plane and perpendicular to the axis of the telescope, it will be focussed (geometrically) to the point where the telescope axis intercepts the image plane. By Fermat's principle, the optical path length from this point to all points on the wavefront is the same.

Now consider a point in the image displaced from the origin by distance that corresponds to an angular displacement $\boldsymbol{\theta}$. (The angular displacement is equal to the linear displacement in the image plane divided by the telescope's effective focal length). In order to focus at that point, a wavefront would need to be tilted by an angle $\boldsymbol{\theta}$ with respect to the first. Thus, the optical path length from this point to any point the original wavefront differs by an

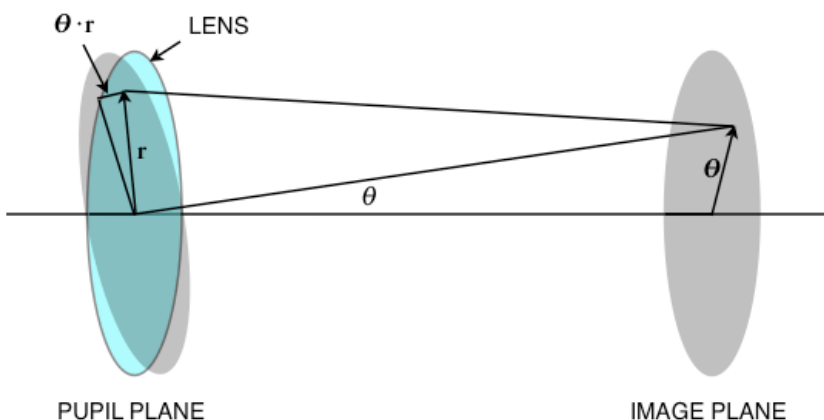


Figure 5.1. Geometry of imaging. A point located at angular position $\boldsymbol{\theta}$ in the image plane is a constant optical path length from all points in a pupil plane that is tilted by angle $\boldsymbol{\theta}$ with respect to the optical axis. Therefore the optical path length from an untilted wavefront is shorter by a distance $\boldsymbol{\theta} \cdot \mathbf{r}$, which introduces a phase shift of $k\boldsymbol{\theta} \cdot \mathbf{r}$.

amount $\boldsymbol{\Theta} \cdot \mathbf{r}$, where \mathbf{r} is a vector extending from the optical axis to the point on the wavefront (see Figure 5.1).

By Huygens principle, the total amplitude at the point $\boldsymbol{\Theta}$ is found by integrating over the amplitude on the wavefront, multiplied by the phase factor corresponding to the propagation distance. Thus, we have

$$\psi(\boldsymbol{\Theta}) \propto \int_A \psi(\mathbf{r}) \exp(-2\pi i \boldsymbol{\Theta} \cdot \mathbf{r}/\lambda) d^2 r. \quad (5.1)$$

We can eliminate the wavelength, by defining a new vector $\boldsymbol{\rho} = \mathbf{r}/\lambda$, that is the position in the pupil in units of wavelength. If we define $\psi(\boldsymbol{\rho})$ to be zero outside the pupil, the integration can be extended to infinity,

$$\psi(\boldsymbol{\Theta}) \propto \int \psi(\boldsymbol{\rho}) \exp(-2\pi i \boldsymbol{\rho} \cdot \boldsymbol{\Theta}) d^2 \rho. \quad (5.2)$$

Comparing this with Eqn. (2.6) we see that the amplitude in the image plane is proportional to the Fourier transform of the amplitude in the pupil.

If no light is absorbed within the telescope, the total energy entering the pupil must equal that in the image plane so we require that

$$\int |\psi(\boldsymbol{\Theta})|^2 d^2 \boldsymbol{\Theta} = \int |\psi(\boldsymbol{\rho})|^2 d^2 \rho. \quad (5.3)$$

This will be true by Parseval's theorem, but only if the constant of proportionality in Eqn. (5.2) is unity. So, we see that for a perfect telescope, the amplitude in the image plane equals the Fourier transform of the amplitude in the pupil,

$$\tilde{\psi}(\boldsymbol{\Theta}) = \int_{-\infty}^{\infty} \psi(\boldsymbol{\rho}) \exp(-2\pi i \boldsymbol{\rho} \cdot \boldsymbol{\Theta}) d^2 \rho. \quad (5.4)$$

Here we have added a \sim over the amplitude in the image plane to emphasise the Fourier transform relationship.

5.1.3. Fraunhofer diffraction

Eqn. (5.4) is equivalent to that describing Fraunhofer diffraction, so an equivalent statement is that the amplitude in the image is the Fraunhofer diffraction pattern of the amplitude in the pupil.

5.1.4. Free propagation

If there are no focusing optics and no variations in the index of refraction, light propagates freely. Consider a plane wave with initial amplitude $\psi(\mathbf{r}, 0)$. After propagating a distance z , the amplitude will be (Born & Wolfe 1999)

$$\psi(\mathbf{r}, z) \propto \int \psi(\mathbf{r}', 0) \exp\{2\pi i [(\mathbf{r} - \mathbf{r}')^2 + z^2]^{1/2} / \lambda\} d^2 r'. \quad (5.5)$$

If the propagation distance is much greater than the displacement $\mathbf{r} - \mathbf{r}'$, the square root can be expanded in a Taylor series. Keeping terms to second order (the *Fresnel approximation*), this becomes

$$\psi(\mathbf{x}, z) \propto \int \psi(\mathbf{r}', 0) \exp[\pi i (\mathbf{r} - \mathbf{r}')^2 / \lambda z] d^2 r'. \quad (5.6)$$

We recognize this integral as a convolution $\psi(\mathbf{r}, z) = \psi(\mathbf{r}, 0) * F(\mathbf{r}, z)$ where the function $F(\mathbf{r}, z)$ is

$$F(\mathbf{r}, z) \propto \exp(\pi i r^2 / \lambda z). \quad (5.7)$$

Again, the constant of proportionality can be found by energy conservation, to within a constant phase factor. The result is

$$F(\mathbf{r}, z) = \frac{1}{i\lambda z} \exp(\pi i r^2 / \lambda z). \quad (5.8)$$

Thus, we see that the amplitude at distance z can be found by convolving the original amplitude by the Fresnel kernel $F(\mathbf{r}, z)$.

This becomes even simpler in Fourier space. Taking the Fourier transform of Eqn. (5.6) and applying the convolution theorem, one obtains

$$\tilde{\psi}(\mathbf{f}, z) = \tilde{\psi}(\mathbf{f}, 0) \cdot \tilde{F}(\mathbf{f}, z), \quad (5.9)$$

where

$$\tilde{F}(\mathbf{f}, z) = \exp(-\pi i \lambda z f^2). \quad (5.10)$$

If $1/f \gg \sqrt{\lambda z}$, then $\tilde{F}(\mathbf{f}, z) \approx 1$, so diffraction is unimportant for length scales that are larger than the Fresnel length $L_F = \sqrt{\lambda z}$.

5.2. Linear theory: PSF, OTF, MTF

The **point-spread function** (PSF) is defined to be the irradiance profile in the image of a point source. In other words, it is the response of the system (telescope plus atmosphere) to an incident plane wave.

Denoting the intensity by $I(\boldsymbol{\Theta})$, we have $I(\boldsymbol{\Theta}) = |\tilde{\psi}(\boldsymbol{\Theta})|^2$.

The **optical transfer function** (OTF) is the Fourier transform of the PSF,

$$\begin{aligned} O(\boldsymbol{\rho}) &= \int \tilde{\psi}(\boldsymbol{\Theta}) \tilde{\psi}^*(\boldsymbol{\Theta}) \exp(2\pi i \boldsymbol{\rho} \cdot \boldsymbol{\Theta}) d^2 \boldsymbol{\theta}, \\ &= \int \psi(\boldsymbol{\rho}') \psi^*(\boldsymbol{\rho}' - \boldsymbol{\rho}) d^2 \boldsymbol{\rho}'. \end{aligned} \quad (5.11)$$

The second line follows by substituting from Eqn. (5.4) and using the two-dimensional Dirac delta function

$$\delta^2(\mathbf{r}) = \int \exp(2\pi i \mathbf{f} \cdot \mathbf{r}) d^2 f. \quad (5.12)$$

The optical transfer function is analogous to transfer functions in electrical engineering and control theory. Optical images are degraded by a number of different effects: seeing, diffraction, etc. The effect of each is to convolve the image with a PSF that describes the effect. The total PSF is the convolution of all

the individual effects. By the convolution theorem, this is equivalent to multiplying the transfer functions for each effect to get the total transfer function.

The modulus of the OTF is called the ***modulation transfer function*** (MTF)

5.3. Effect of seeing on image quality

Seeing has a profound effect on image quality for all but the smallest telescopes. Not only is the image blurred, but because the light is spread out over a larger area, the intensity is reduced compared to the background. Thus, the contrast of the image is degraded and the sensitivity is much reduced.

5.3.1. Diffraction-limited PSF and MTF

To illustrate the concepts of the previous section, let's calculate the OTF and PSF of a perfect telescope having a filled circular aperture of diameter D . For a perfect plane wave incident on the telescope, the amplitude in the entrance pupil is equal to the pupil function $P(\rho)$, defined to have unit value inside the aperture and zero outside. Let's normalize the input amplitude so that the integral of the irradiance over the entrance pupil is unity. Then,

$$\psi(\rho) = A^{-2} P(\rho) = A^{-2} \Pi(2\rho\lambda/D), \quad (5.13)$$

where $A = \pi D^2/4$ is the area of the pupil and

$$\Pi(x) \equiv \begin{cases} 1 & |x| \leq 1/2 \\ 0 & |x| > 1/2 \end{cases} \quad (5.14)$$

The OTF is the autocorrelation of this function, namely the area of overlap of two circles, whose centers are separated by a distance $\rho\lambda$. This is easily calculated, with the result shown in Figure 5.2,

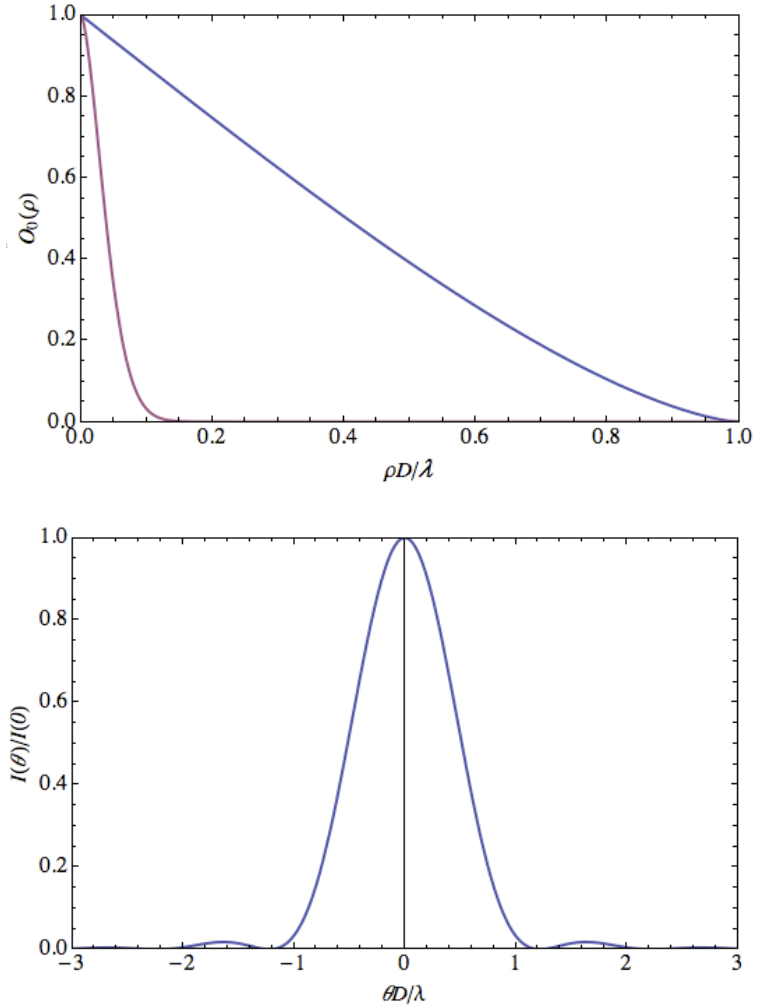


Figure 5.2. Top: MTF of a filled circular aperture (upper curve). For comparison, the atmospheric MTF for Kolmogorov turbulence ($D/r_0 = 10$) is also shown (lower curve). Bottom: PSF corresponding to the diffraction MTF.

$$O_0(\rho) = 1 - \frac{2}{\pi} \left[\arcsin(\rho\lambda/D) + \frac{\lambda\rho}{D} (1 - \lambda^2\rho^2/D^2)^{1/2} \right]. \quad (5.15)$$

The PSF is most easily found by taking the Fourier transform of the amplitude (Eqn. 5.13) and squaring it. This gives the *Airy profile*, illustrated in Figure 5.2,

$$I(\theta) = \left[\frac{2J_1(\pi\theta D/\lambda)}{\pi\theta D/\lambda} \right]^2. \quad (5.16)$$

The FWHM of this function is $\vartheta \simeq 1.029 \lambda/D$.

5.3.2. Effect of seeing

Our aim now is to determine quantitatively the effect of atmospheric turbulence on image quality. The first step will be to determine the OTF of seeing. The OTF is given by Eqn. (5.11). However, since the fluctuations produced by atmospheric turbulence are stationary, we can replace the integral with an ensemble average. This gives

$$\begin{aligned} O(\rho) &= \langle \psi(0)\psi^*(-\rho) \rangle, \\ &= \Gamma_2(-\rho) = \Gamma_2(\rho). \end{aligned} \quad (5.17)$$

The last step follows from the isotropy of the turbulence.

So we see that the OTF of atmospheric turbulence is the mutual coherence function. We have already calculated this in Section 4.2.2. From Eqn. (4.14), keeping in mind that the physical distance $r = \lambda\rho$, the result is

$$\Gamma_2(\rho) = \exp \left[-4\pi^2 k^2 \int_0^z dz_0 \int_0^\infty \Phi(\kappa) [1 - J_0(\kappa\lambda\rho)] \kappa d\kappa \right]. \quad (5.18)$$

We have also already evaluated the frequency integral for Kolmogorov turbulence. Referring to Eqns. (4.27) and (4.29) we see that

$$\begin{aligned} O_K(\rho) &= \Gamma_2(\rho) = \exp[-\mathcal{D}(\rho)/2], \\ &\simeq \exp[-3.44(\lambda\rho/r_0)^{5/3}]. \end{aligned} \quad (5.19)$$

The seeing PSF is the Fourier transform of this. It cannot be calculated in closed form, although it has a series representation in terms of hypergeometric functions. However, observe that Eqn. (4.14) is close to a Gaussian. Since the Fourier transform of a Gaussian is also Gaussian, we expect that the PSF will be roughly Gaussian. This turns out to be true for the core, but the outer part of the PSF falls less rapidly, approaching the power law $I(\theta) \propto \theta^{-11/3}$ at large angles. Racine (1996) has found that the seeing PSF can be represented quite well by the sum of a pair of Moffat (1969) functions.

One finds by numerical calculation that the FWHM of the Kolmogorov PSF is

$$\vartheta_K \simeq 0.96 \lambda/r_0. \quad (5.20)$$

5.3.3. Strehl ratio

The Strehl ratio is defined as the ratio of the central irradiance of the PSF to that of a diffraction limited PSF,

$$S = I(0)/I_0(0). \quad (5.21)$$

Now, since the OTF is the Fourier transform of the PSF, the central irradiance is equal to the integral of the OTF,

$$I(0) = \int O(\rho) d^2\rho. \quad (5.22)$$

The integral of the OTF is called the ***resolving power*** of the telescope, and is equivalent to the bandwidth in electrical engineering. Thus, the Strehl ratio is a measure of the relative resolving power of the telescope + atmosphere.

A characteristic width of the diffraction-limited OTF is D/λ , whereas a characteristic width of the seeing OTF (Eqn. 5.19), is r_0/λ . So, the Strehl ratio of seeing-limited images will be $S \sim (r_0/D)^2$, which is proportional to wavelength to the 12/5 power. This is typically a very small number.

A very useful relation between the Strehl ratio and the wavefront variance can be obtained as follows. From Eqn. (5.19), (5.21), (5.22) and the multiplicative property of the transfer function,

$$\begin{aligned} S &= \int O d^2\rho / \int O_0 d^2\rho, \\ &= \int O_K O_0 d^2\rho / \int O_0 d^2\rho, \\ &= \int O_0 \exp[-\mathcal{D}_\phi(\rho)/2] d^2\rho / \int O_0 d^2\rho, \\ &= \int O_0 \exp[-\mathcal{B}_\phi(0) + \mathcal{B}_\phi(\rho)] d^2\rho / \int O_0 d^2\rho, \\ &= \exp[-\mathcal{B}_\phi(0)] \left\{ \int O_0 \exp[\mathcal{B}(\rho)] d^2\rho / \int O_0 d^2\rho \right\}. \end{aligned} \quad (5.23)$$

Now, if the wavefront variance is small, $\mathcal{B}(\rho) \ll 1$ within the telescope aperture, the factor in parenthesis will be very close to unity. Now $\mathcal{B}_\phi(0)$ is the ensemble average of the square phase fluctuation, which is the same as the phase variance averaged over the aperture, σ_ϕ^2 . Thus we have the important result

$$S \approx \exp(-\sigma_\phi^2). \quad (5.24)$$

This is called the ***Maréchal approximation*** (Maréchal 1947)

5.4. Zernike functions

Zernike functions are a set of orthogonal functions that are convenient for representing wavefront errors in a circular pupil. Different normalizations and labeling can be used. Most common in AO applications are the modified Zernike functions adopted by Noll (1976), which we use here.

5.4.1. Definition

The Noll Zernike functions Z_j are defined by

$$\begin{aligned} Z_j &= \sqrt{n+1} R_n^0(r) & m = 0 \\ Z_j &= \sqrt{n+1} R_n^m(r) \sqrt{2} \cos m\phi & m \neq 0, j \text{ even} \\ Z_j &= \sqrt{n+1} R_n^m(r) \sqrt{2} \sin m\phi & m \neq 0, j \text{ odd} \end{aligned} \quad (5.25)$$

where

$$R_n^m(r) = \sum_{s=0}^{(n-m)/2} \frac{(-1)^s (n-s)!}{s! [(n+m)/2-s]! [(n-m)/2-s]!} r^{n-2s} \quad (5.26)$$

The *radial order* n and *azimuthal order* m are integers and always satisfy the conditions $m \leq n$, $n - |m| = \text{even}$. The index j is a function of m and n and serves to order the functions.

5.4.2. Orthogonality

The Zernike functions satisfy the following *orthogonality condition*

$$\frac{1}{\pi} \int_0^1 dr \int_0^{2\pi} d\phi Z_i(r, \phi) Z_j(r, \phi) = \delta_{ij}, \quad (5.27)$$

where δ_{ij} is the Kronecker delta, equal to unity if its indices are equal and zero otherwise. This allows one to expand any continuous function defined on the unit disk,

$$f(r, \phi) = \sum_{j=0}^{\infty} a_j Z_j(r, \phi), \quad (5.28)$$

where the coefficients are given by

$$a_j = \frac{1}{\pi} \int_0^1 dr \int_0^{2\pi} d\phi f(r, \phi) Z_j(r, \phi). \quad (5.29)$$

The first few Zernicke functions are listed in Table 5.1 and illustrated in Figure 5.3.

5.4.3. Fourier components

The Fourier transforms of the Zernike functions can be written in terms of Bessel functions,

$$\begin{aligned} \tilde{Z}_j(\kappa, \phi) &= 2i^n \sqrt{n+1} J_{n+1}(\kappa) \kappa^{-1} & m = 0 \\ \tilde{Z}_j(\kappa, \phi) &= 2\sqrt{2} i^n \sqrt{n+1} J_{n+1}(\kappa) \kappa^{-1} \cos m\phi & m \neq 0, j \text{ even} \\ \tilde{Z}_j(\kappa, \phi) &= 2\sqrt{2} i^n \sqrt{n+1} J_{n+1}(\kappa) \kappa^{-1} \sin m\phi & m \neq 0, j \text{ odd} \end{aligned} \quad (5.30)$$

5.4.4. Residual atmospheric wavefront variance

For Kolmogorov turbulence, the wavefront phase variance is infinite. However, the infinity is contained entirely in the piston term. If this is subtracted, the result is finite. Noll (1976) has calculated the residual phase variance Δ_j that remains when the first j Zernike modes are removed. From this one can determine the improvement in the Strehl ratio after correction for atmospheric tilt, focus, astigmatism, coma terms, etc, by an AO system. The results are summarized in Table 5.2.

Table 5.1. Zernike functions to fourth radial order, after Noll (1976)

j	n	m	Z_j	Name
1	0	0	1	Piston
2	1	-1	$2r \cos \phi$	Tilt
3	1	1	$2r \sin \phi$	Tilt
4	2	0	$\sqrt{3}(2r^2 - 1)$	Focus
5	2	2	$\sqrt{6} r^2 \sin 2\phi$	3rd-order astigmatism
6	2	-2	$\sqrt{6} r^2 \cos 2\phi$	3rd-order astigmatism
7	3	-1	$\sqrt{8}(3r^3 - 2r) \sin \phi$	3rd-order coma
8	3	1	$\sqrt{8}(3r^3 - 2r) \cos \phi$	3rd-order coma
9	3	3	$\sqrt{8} r^3 \sin 3\phi$	trefoil
10	3	-3	$\sqrt{8} r^3 \cos 3\phi$	trefoil
11	4	0	$\sqrt{5}(6r^4 - 6r^2 + 1)$	3rd-order spherical
12	4	-2	$\sqrt{10}(3r^4 - 3r^2) \cos 2\phi$	5th-order astigmatism
13	4	2	$\sqrt{10}(3r^4 - 3r^2) \sin 2\phi$	5th-order astigmatism
14	4	-4	$\sqrt{10} r^4 \cos 4\phi$	
15	4	4	$\sqrt{10} r^4 \sin 4\phi$	

Table 5.2. Residual mean phase variance after removal of sequential Zernike modes (Noll 1976).

$\Delta_1 = 1.0299(D/r_0)^{5/3}$	$\Delta_2 = 0.582(D/r_0)^{5/3}$	$\Delta_3 = 0.134(D/r_0)^{5/3}$	$\Delta_4 = 0.111(D/r_0)^{5/3}$
$\Delta_5 = 0.0880(D/r_0)^{5/3}$	$\Delta_6 = 0.0648(D/r_0)^{5/3}$	$\Delta_7 = 0.0587(D/r_0)^{5/3}$	$\Delta_8 = 0.0525(D/r_0)^{5/3}$
$\Delta_9 = 0.0463(D/r_0)^{5/3}$	$\Delta_{10} = 0.0401(D/r_0)^{5/3}$	$\Delta_{11} = 0.0377(D/r_0)^{5/3}$	$\Delta_{12} = 0.0352(D/r_0)^{5/3}$

For large values of j , $\Delta_j \approx 0.2944 j^{-\sqrt{3}/2} (D/r_0)^{5/3}$.

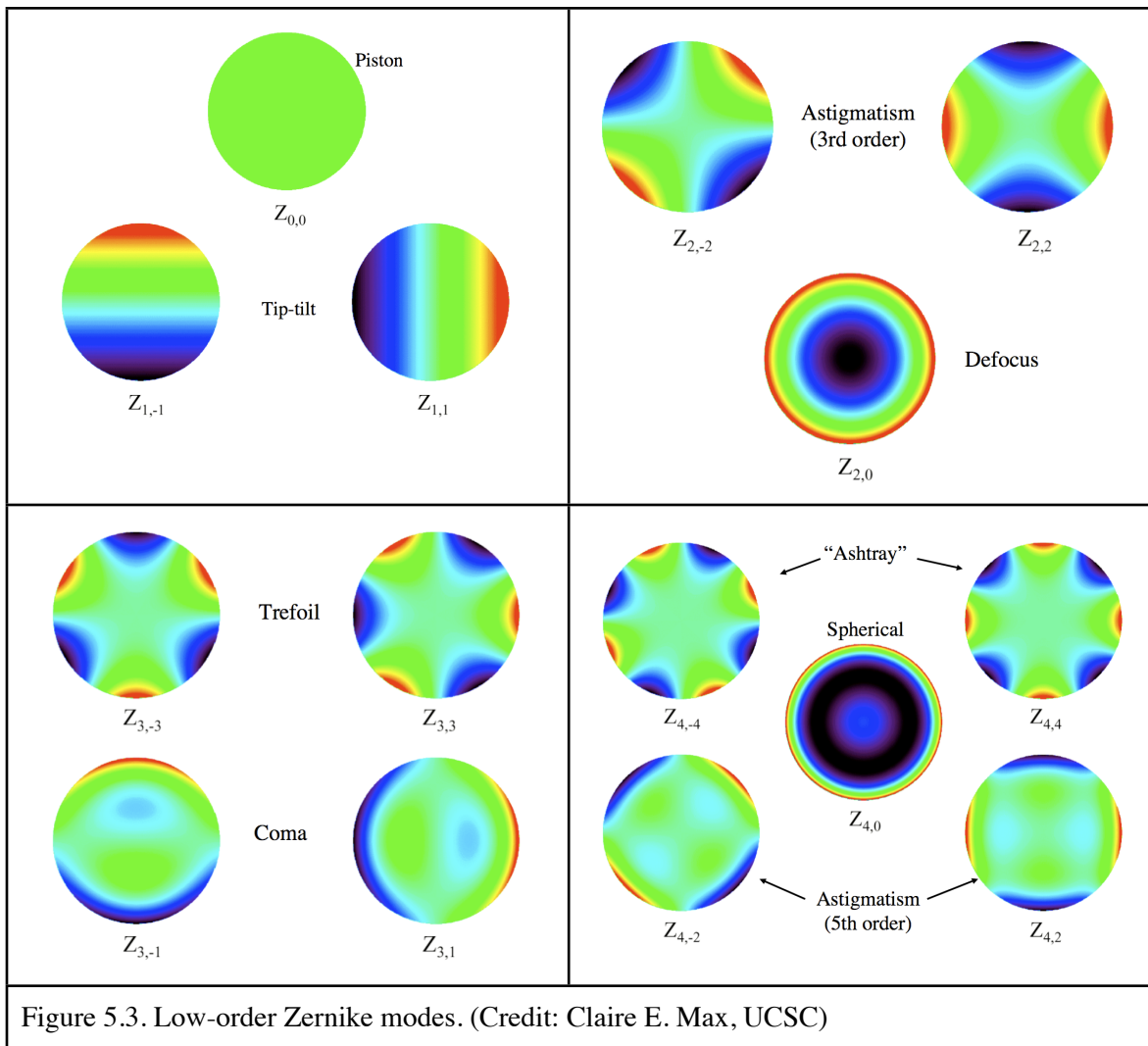


Figure 5.3. Low-order Zernike modes. (Credit: Claire E. Max, UCSC)

6. Wavefront sensors and deformable mirrors

6.1. Wavefront sensors

In order to correct the phase distortion introduced by the atmosphere, it is first necessary to measure it. Several techniques have been developed for this purpose.

6.1.1. Shack-Hartmann

Perhaps the most common is the Shack-Hartmann sensor. It employs a lenslet array and imaging detector to measure the local slope of the wavefront, arriving from a reference star, over a grid of points in the pupil (Figure 6.1).

The lenslet array is placed in the optical system at a location that is optically conjugate to the turbulence that is being sensed. For a conventional AO system, this is at a pupil (i.e. optically conjugate to the entrance pupil). Each lenslet samples a small portion of the pupil, called a *subaperture*.

Each lenslet forms an image of the reference star on the detector. The displacement of this image, from the central position, is proportional to the average slope of the wavefront over the subaperture. Specifically, if Θ_c is the angular displacement of the intensity-weighted centroid of the image (the linear displacement divided by the focal length of the lenslet), A is the area of the subaperture and $\nabla\varphi$ is the local gradient of the wavefront phase,

$$\Theta_c = k^{-1} \nabla\varphi \equiv \frac{1}{kA} \int_A \nabla\varphi d^2x. \quad (6.1)$$

The wavefront phase error can then be reconstructed (to within an arbitrary constant), from the measured gradients. To first order,

$$\varphi = \varphi(0) + \mathbf{x} \cdot \nabla\varphi + \dots \quad (6.2)$$

We postpone for now a discussion of the details of the reconstruction process.

Because the sensor measures only the average gradient over each subaperture, our knowledge of the phase is incomplete. The difference between the actual phase and the reconstructed phase is called the *fitting error*. Clearly, the fitting error can be reduced by increasing the number of subapertures that cover the pupil. However, the number of photons that are available for each subaperture is then reduced, which increases the measurement noise. A balance of these errors is required, and this is part of the process of optimization of an AO system.

6.1.2. Curvature

The curvature sensor, invented by F. Roddier (1988), makes use of the fact that as light propagates from a pupil to a focus, phase fluctuations develop into irradiance fluctuations (Figure 6.2). Thus by measuring

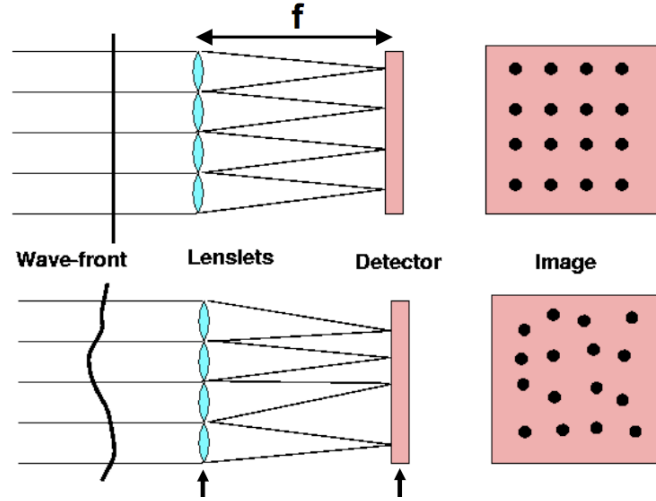


Figure 6.1. Principle of a Shack-Hartmann wavefront sensor. (Credit: Claire E. Max, UCSC)

the irradiance fluctuations in a defocused image, one can estimate the wavefront curvature and thus recover the phase.

To see this consider the simple telescope shown in Figure 6.3. The intensity pattern in the beam at a distance z from the pupil is the same as the intensity pattern in the conjugate plane, located in the parallel beam at a distance z' from the pupil.

From geometrical optics, these two distances are related to the telescope focal length f by the Gaussian image formula,

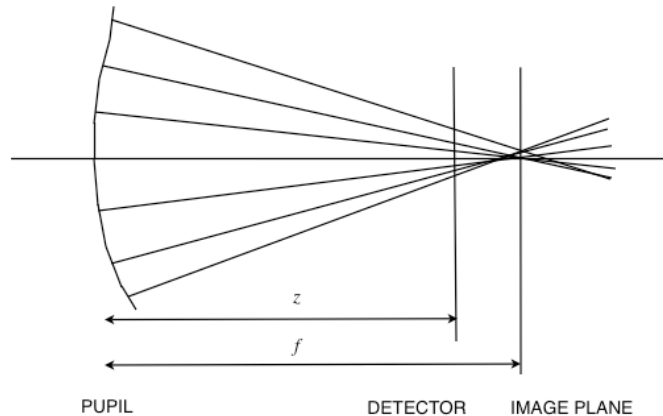


Figure 6.2. Principle of a curvature wavefront sensor. Variations in wavefront curvature develop into variations in intensity as the light propagates to the focus.

$$z' = zf/(f-z). \quad (6.3)$$

By energy conservation, the irradiance in the converging beam is higher than that in the conjugate plane by a factor of $f^2/(f-z)^2$.

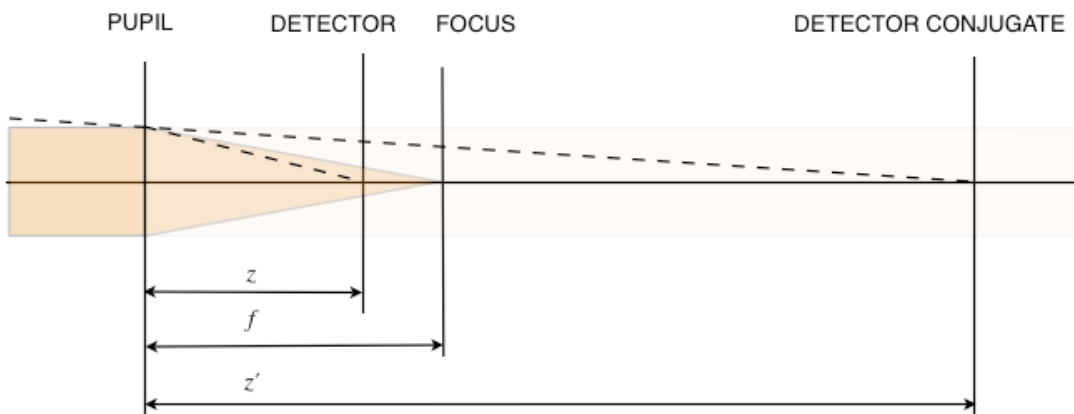


Figure 6.3. Geometry for curvature sensor analysis. The intensity fluctuations in the detector plane are the same as those in the conjugate plane, which can be obtained by propagating the phase fluctuations in the pupil plane using Fresnel diffraction theory.

The irradiance in the conjugate plane can be found using Fresnel diffraction. In Section 5.5 we saw that the amplitude at distance z is found by convolving the original amplitude with the Fresnel kernel $F(r,z) = \exp(\pi ir^2/\lambda z)/i\lambda z$. Let the amplitude in the pupil be $\psi(\mathbf{r},0)$. Then, the amplitude at a distance z' will be

$$\psi(\mathbf{r},z') = \psi(\mathbf{r},0) * F(r,z'). \quad (6.4)$$

In Fourier space this becomes

$$\tilde{\psi}(\mathbf{f}, z') = \tilde{\psi}(\mathbf{f}, 0) \cdot \exp(-i\pi\lambda z' f^2). \quad (6.5)$$

If the phase fluctuations in the pupil are small, we may write $\psi(\mathbf{r}, 0) \approx 1 + i\varphi(\mathbf{r})$, and thus $\tilde{\psi}(\mathbf{f}, 0) \approx \delta^2(\mathbf{f}) + i\tilde{\varphi}(\mathbf{f})$. Substituting these into Eqn. (6.5) and taking the inverse transform gives

$$\begin{aligned} \psi(\mathbf{r}, z') &\approx \int \exp(-i\pi\lambda z' f^2) [\delta^2(\mathbf{f}) + i\tilde{\varphi}(\mathbf{f})] d^2 f, \\ &= 1 + i \exp(i\lambda z' \nabla^2 / 4\pi) \varphi(\mathbf{r}). \end{aligned} \quad (6.6)$$

The last line is obtained by expanding the exponential in a Taylor series and applying the Fourier derivative theorem to each term. The exponential of the Laplacian operator is to be interpreted in terms of the series expansion.

To first order in $\varphi(\mathbf{r})$, the irradiance is therefore

$$\begin{aligned} I(\mathbf{r}, z') &\approx 1 + i[\exp(i\lambda z' \nabla^2 / 4\pi) - \exp(-i\lambda z' \nabla^2 / 4\pi)] \varphi(\mathbf{r}) \\ &= 1 - 2 \sin(\lambda z' \nabla^2 / 4\pi) \varphi(\mathbf{r}). \end{aligned} \quad (6.7)$$

The irradiance fluctuation is the difference between this and the mean irradiance

$$\begin{aligned} \Delta I(\mathbf{r}, z') &= -2 \sin(\lambda z' \nabla^2 / 4\pi) \varphi(\mathbf{r}), \\ &\approx -\frac{z'}{k} \nabla^2 \varphi(\mathbf{r}) + \frac{1}{3} \left(\frac{z'}{k}\right)^3 \nabla^6 \varphi(\mathbf{r}) + \dots. \end{aligned} \quad (6.8)$$

As long as the irradiance fluctuations are small the first (linear) term dominates. Transferring this now to the converging beam using Eqn. (6.3), and dividing by the mean irradiance, we obtain

$$\frac{\Delta I(r, z')}{\langle I \rangle} \approx -\frac{fz}{k(f-z)} \nabla^2 \varphi(\mathbf{r}). \quad (6.9)$$

Here the vector \mathbf{r} refers to the position in the entrance pupil, not the demagnified coordinate in the converging beam.

The irradiance fluctuations can be sensed by placing an imaging detector, such as a CCD, in the beam but displaced longitudinally from the focus. The closer it is to the focus, the larger the fluctuations (by virtue of Eqn. 6.9). However, care must be taken to use a large enough displacement so that the linear approximation is valid.

Although an overall wavefront tilt does not change the irradiance, it does produce a transverse shift in the image position by an amount $(z/k) \nabla \varphi$, which when referred back to coordinates in the entrance pupil is a shift $fz/[k(f-z)] \nabla \varphi$. This shift is easily sensed by computing the centroid.

In Roddier's curvature sensor, the irradiance is measured on both sides of the focus. By subtracting the two images, calibration errors cancel. This was done by inserting a membrane mirror in the beam and rapidly alternating between positive and negative curvature of the membrane in order to move the focus in and out, on either side of the detector (Roddier used an array of avalanche photodiodes). However, in principle a single defocused image will suffice (Hickson 1994).

6.1.3. Pyramid

The most recent development in wavefront sensing is the pyramid sensor (Ragazzoni 1996). In this device a four-sided pyramid is placed at the focus (Figure 6.4). The pyramid divides the image into four beams which then pass through a field lens that produces four images of the pupil on a CCD detector. A perfect image will result in the irradiance patterns in all four pupil images being equal. Any wavefront errors will deflect rays to one side or other of the focus, creating differences in the irradiance patterns in the four pupil images.

In order to measure the wavefront phase error, the prism is moved back and forth, in both x and y directions, at a constant speed with maximum displacement $\pm L$. Now, for each point in the pupil, the transverse displacement of the corresponding ray in the focal plane is $f\nabla\varphi/k$. Referring to Figure 6.4, we see that when the prism oscillates in the x direction, the fraction of time that the ray is sent to pupil image a is $(L + f\nabla_x\varphi/k)/(2L)$, and the fraction of time for pupil image c is $(L - f\nabla_x\varphi/k)/(2L)$. Therefore, by subtracting the intensities in the two pupil images we can obtain the x -component of the phase gradient,

$$\frac{I_a - I_c}{I_a + I_c} = \frac{f\nabla_x\varphi}{kL}. \quad (6.10)$$

The same information is provided by the difference between pupil images b and d . Similar relation holds for the y direction. Combining these, we find

$$\begin{aligned} \nabla_x\varphi(\mathbf{r}) &= \frac{kL}{f} \left[\frac{I_a(\mathbf{r}) - I_c(\mathbf{r}) + I_b(\mathbf{r}) - I_d(\mathbf{r})}{I_a(\mathbf{r}) + I_c(\mathbf{r}) + I_b(\mathbf{r}) + I_d(\mathbf{r})} \right], \\ \nabla_y\varphi(\mathbf{r}) &= \frac{kL}{f} \left[\frac{I_b(\mathbf{r}) - I_a(\mathbf{r}) + I_d(\mathbf{r}) - I_c(\mathbf{r})}{I_a(\mathbf{r}) + I_c(\mathbf{r}) + I_b(\mathbf{r}) + I_d(\mathbf{r})} \right]. \end{aligned} \quad (6.11)$$

An important advantage of the pyramid sensor is that its sensitivity and dynamic range are determined by the amplitude L of the oscillation of the prism, and can be tuned in real time to provide the best match to the atmospheric conditions.

6.1.4. Interferometric sensors

Wavefront sensors employing interferometric principles have also been used for AO. The most common is the *shearing interferometer*.

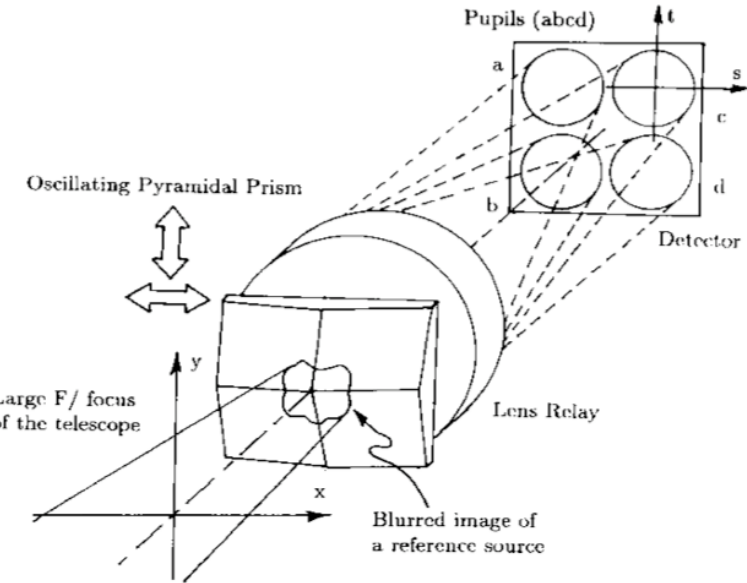


Figure 6.4. Sketch of a pyramid wavefront sensor. (Ragazzoni 1996)

In a shearing interferometer, light is split into two beams using a beamsplitter. One beam is then shifted in a transverse direction and the beams are then recombined. The amplitude in the recombined pupil image is $\psi(\mathbf{r}) = \{\exp[i\varphi(\mathbf{r})] + \exp[i\varphi(\mathbf{r} - \mathbf{u})]\}/2$, where \mathbf{u} is the shift vector. Therefore, the irradiance is

$$I(\mathbf{r}) = \psi(\mathbf{r})\psi^*(\mathbf{r}) = \frac{1}{2}\{1 + \cos[\varphi(\mathbf{r}) - \varphi(\mathbf{r} - \mathbf{u})]\}. \quad (6.12)$$

Using a Taylor expansion $\varphi(\mathbf{r} - \mathbf{u}) \approx \varphi(\mathbf{r}) - \mathbf{u} \cdot \nabla \varphi(\mathbf{r})$, this becomes

$$I(\mathbf{r}) \approx \frac{1}{2}\{1 + \cos[\mathbf{u} \cdot \nabla \varphi(\mathbf{r})]\} \quad (6.13)$$

so from the irradiance in the combined beam one can determine the component of the phase gradient in the direction of the shift.

By splitting the beam into two channels and shearing each in orthogonal directions one obtains both components of the phase gradient.

6.2. Deformable mirrors

A key component of AO systems are the deformable mirrors (DMs) that produce the required wavefront correction. Let's take a look at some of the current technology.

6.2.1. Piezoelectric mirrors

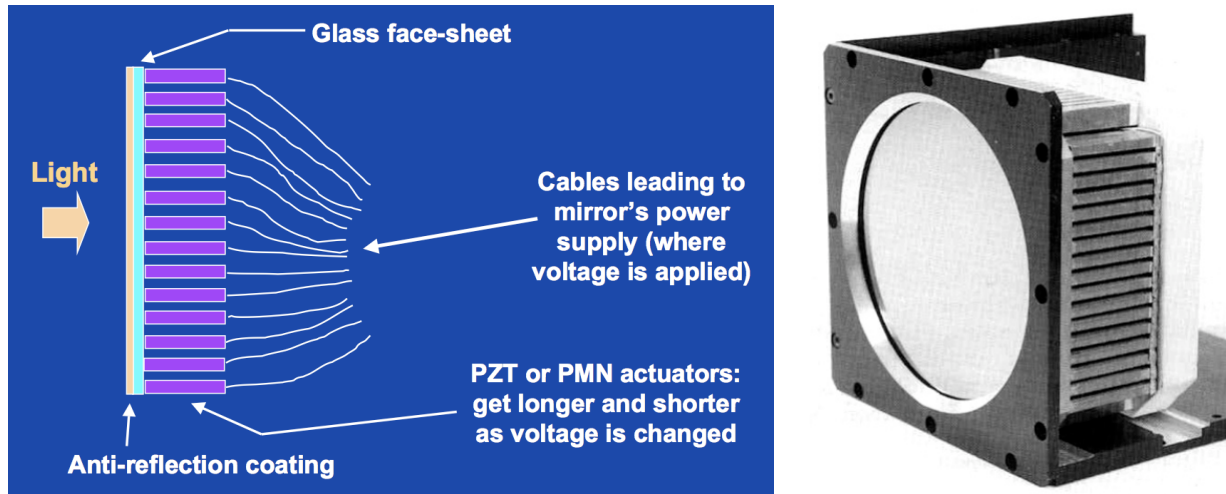


Figure 6.5. Sketch of a piezoelectric deformable mirror (left) and photograph of a 249-actuator mirror made by CILAS (France). One end of each actuator is attached to a thin aluminized glass face-sheet. The other end is secured to a base plate. Voltages applied to the actuators change their length, causing the face sheet to flex. (Credit: Claire E. Max, UCSC, and Michael Loyd-Hart).

Most commonly used at the present time are piezoelectric face-sheet mirrors (Figure 6.5). These consist of a thin glass mirror to which is attached an array of piezoelectric actuators.

Two types of materials are used, Lead zirconate titanate (PZT) provides a displacement that is nearly linear with voltage, but with hysteresis at a level of 10 - 20%. Lead magnesium niobate is a

magnetostrictive material that expands quadratically with voltage. It has lower hysteresis than PZT at temperatures of 15 C and greater, but its response is more temperature sensitive.

Piezoelectric DMs have been made with as many as 10^3 actuators and diameters as large as 30 cm. The typical spacing between actuators is several mm. The maximum deflection of the surface (the *stroke*) is typically on the order of 10 um.

6.2.2. MEMS mirrors

A second type of DM, undergoing rapid development, are micro electro-mechanical systems (**MEMS**) mirrors (Figure 6.6). These are fabricated in silicon wafers using lithographic technology employed by the semiconductor industry.

They can in principle provide very high actuator density and count. Their main limitations at present are small size and limited stroke.

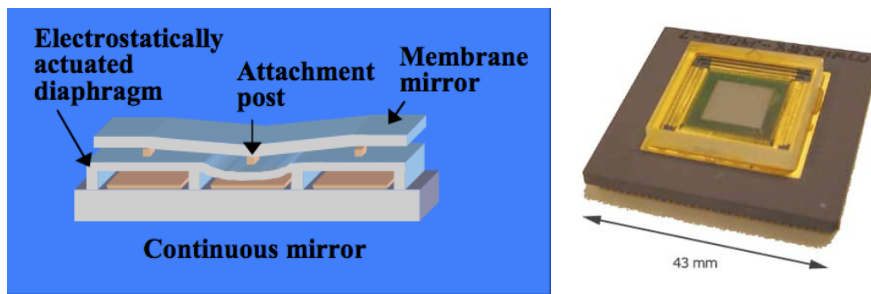


Figure 6.6. Cross section (left) and photograph (right) of a MEMS deformable mirror. This technology shows great promise for AO applications (Credit: Claire E. Max, UCSC).

6.2.3. Bimorph mirrors

A bimorph mirror consists of two thin plates of piezoelectric material bonded over a configuration of electrodes. An applied voltage causes the mirror to bend in response. These mirrors are particularly-well suited for use with curvature sensors.

6.2.4. Segmented mirrors

Segmented mirrors have individual segments, each controlled by actuators. Normally, each segment has three degrees of freedom: tip, tilt and height (piston), which can all be individually controlled.

Edge sensors provide information about the relative positions of adjacent segments.

Very large segmented mirrors have been made (eg. the Keck telescope primary mirrors). These do not move fast enough to correct atmospheric turbulence, but are *active* in that they move to compensate for thermal and gravitational distortion and alignment errors.

6.2.5. Adaptive secondary mirrors

Adaptive secondary mirrors have been developed that use magnetic actuators (voice coils) to deform a thin face sheet that is polished to a convex or concave shape (Figure 6.7). The largest so far are the adaptive secondary mirrors of the Large Binocular Telescope (LBT).

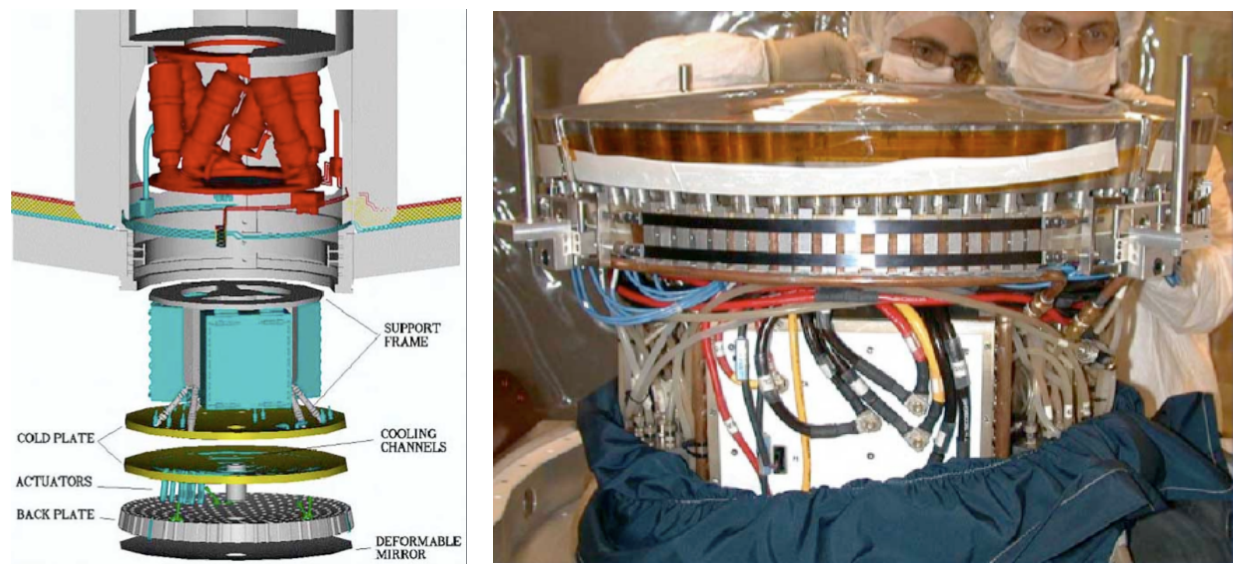


Figure 6.7. Schematic and photograph of the MMT deformable secondary mirror (Credit: Claire E. Max, UCSC).

7. Conventional AO

Early AO systems provided only low-order correction of the wavefront. On small telescopes, just correcting tip-tilt can provide a substantial gain. From Table 5.2 we see that these two Zernike modes together contain 87% of the wavefront phase variance.

More generally, if one completely corrects the first j Zernike modes, the wavefront phase variance is reduced to Δ_j , for which values are listed in Table 5.2.

The resulting Strehl ratio can be estimated using the Maréchal approximation. Thus,

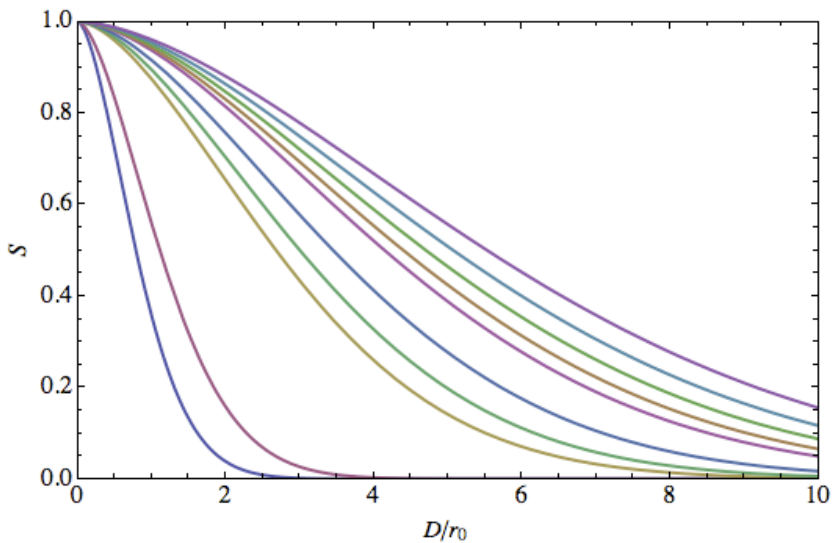


Figure 7.1. Strehl ratio achievable with perfect correction of low order Zernike modes. From bottom to top, the curves correspond to correction of no modes, one mode (tilt), two modes (both tilt modes), three modes (tip-tilt and focus, four modes, etc.

$$S \approx \exp(-\Delta_j). \quad (7.1)$$

This is plotted in Figure 7.1 for the first 10 terms. Correcting both tilt modes produces a significant improvement in Strehl ratio for telescope with diameter less than $\sim 5 r_0$. Since r_0 increases with wavelength, low-order AO can be quite effective at mid and far infrared wavelengths.

Figure 7.2 shows the number of Zernike modes that must be corrected in order to achieve a Strehl ratio of 0.8, as a function of telescope diameter. Achieving this Strehl ratio at 1 um with a 30-metre telescope would require correction of $\sim 10^5$ modes.

7.1. Single-star AO

The simplest type of AO system employs light from a single natural guide star (NGS) and a single deformable mirror. If the star

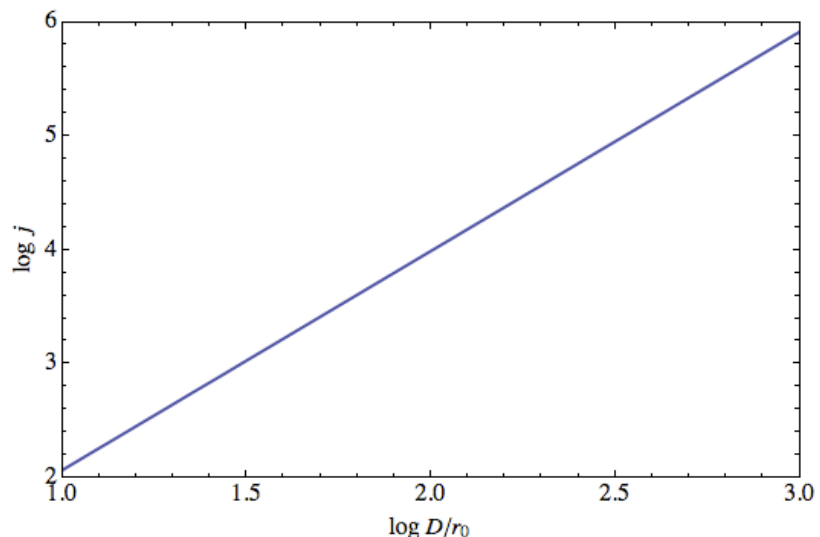


Figure 7.2. Number of modes that must be corrected to achieve a Strehl ratio of 0.8 as a function of aperture diameter.

is reasonably bright, this system can provide very good performance for objects close to the star. However, the sky coverage (the area of sky accessible for AO) is very limited, as will be seen in the next section.

7.2. Isoplanatic effects

Let's estimate the variation in Strehl ratio as a function of angle θ from the guide star. The rms phase difference between the light from the reference star and the object, averaged over the pupil, will be

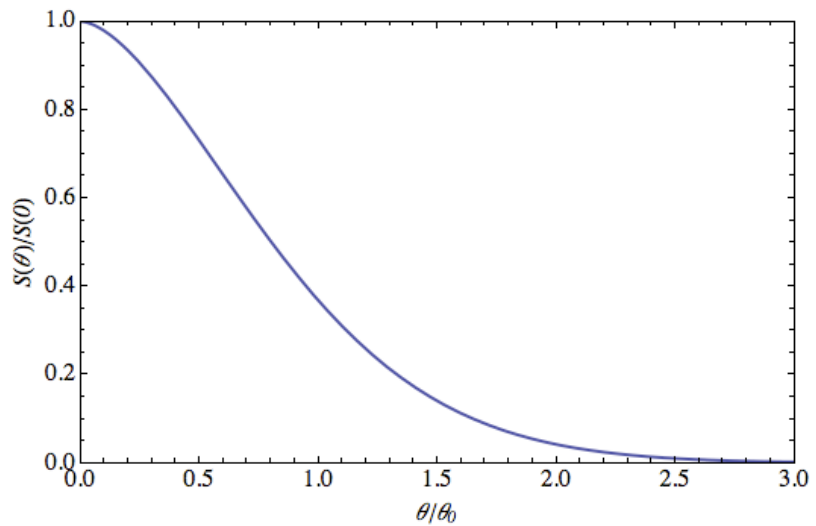


Figure 7.3. Strehl ratio as a function of angle from the guide star, for conventional adaptive optics.

$$\begin{aligned}\sigma_\theta^2 &= \frac{1}{A} \int_A [\varphi(\mathbf{r}) - \varphi(\mathbf{r} + \boldsymbol{\theta}h)]^2 d^2r \\ &= (\theta/\theta_0)^{5/3},\end{aligned}\quad (7.2)$$

where, for a Kolmogorov spectrum (using Eqn. 4.28),

$$\theta_0 = \left[2.913 k^2 \sec^{8/3} \zeta \int_0^\infty C_N^2(h) h^{5/3} dh \right]^{-3/5}. \quad (7.3)$$

From this we see that the isoplanatic angle $\theta_0 \propto \lambda^{6/5}$, and is determined by high-level turbulence.

This rms error must be added to the rms error from other sources, independent of θ . Call this $\sigma_{\phi 0}^2$. Then the ratio of the Strehl ratio at angle θ to that at $\theta = 0$ will be

$$\frac{S(\theta)}{S(0)} = \frac{\exp(\sigma_\theta^2 + \sigma_{\phi 0}^2)}{\exp(\sigma_{\phi 0}^2)} = \exp(\sigma_\theta^2). \quad (7.4)$$

This function is plotted in Figure 7.3. The image quality is reduced substantially at the isoplanatic angle and decreases rapidly beyond that.

At typical astronomical sites, $\theta_0 \sim 5$ arcsec at a wavelength of 1 um, so the target needs to be within a few arcsec of a fairly bright star for good correction.

7.3. Control systems

Information from the WFS(s) is processed by a **control system**, which controls the shape of the DM(s). There are two possibilities, illustrated in Figure 7.4.

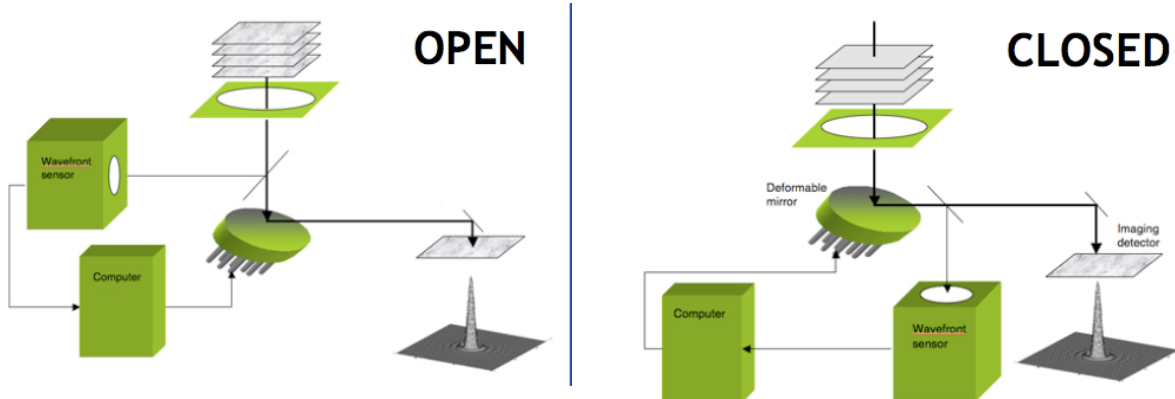


Figure 7.4. Open and closed-loop control systems (Credit: Claire E. Max, UCSC).

An **open-loop** control system uses the WFS measurements to predict the correct shape of the DM and then applies a correction. Light reaches the WFS *before* correction by the DM. There is no monitoring of the effect of this correction, and therefore there is ***no feedback*** in this system.

In a **closed-loop** control system light is sent to the WFS *after* correction by the DM. This allows the effect of the DM to be monitored and further corrections applied to reduce the error. Thus, ***feedback*** is employed in a closed-loop system. This generally gives a better correction than an open-loop system.

Control theory is beyond the scope of these notes, but is covered in depth by many text books. For a brief introduction in the context of Adaptive Optics, I recommend the presentation by Don Gavel (UCSC), available on line at <http://www.ucolick.org/~max/289C/>.

When applying a control signal to a DM, one must take into account various factors such as hysteresis and nonlinear response. Also, these mirrors usually suffer from ***cross-talk*** - moving a single actuator affects the shape of the mirror at other locations.

The ***influence function*** of a DM is a matrix that describes the change in each subaperture due to a voltage applied to a single electrode. Ideally this should be close to diagonal (little cross-talk).

7.4. The Gemini ALTAIR AO system

An example of a conventional adaptive optics system is the ALTAIR AO system available on the 8-metre Gemini North telescope. The optical and mechanical layout for the natural guide star mode is shown in Figures 7.5 - 7.7.

Light passing through the telescope focal plane is intercepted by a collimator mirror, and directed to the deformable mirror (DM). This mirror is placed in the beam at a position that is optically conjugate to an altitude of 10.5 km. The deformable mirror has 177 piezoelectric actuators.

Light reflected from the deformable mirror passes next to a tip-tilt mirror (TTM) that can pivot rapidly on two axes to remove both tilt components of the wavefront. This leaves the DM free to correct higher-order modes that do not require as much stroke.

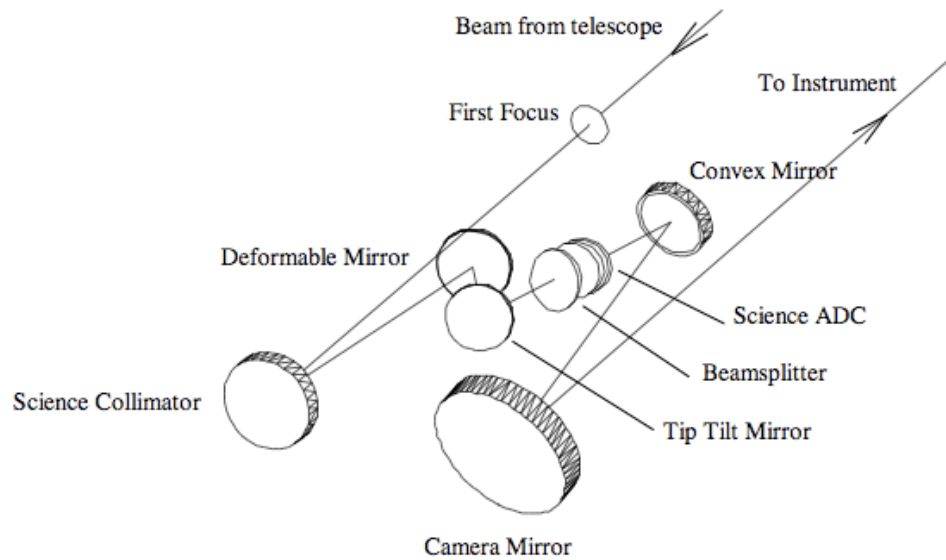


Figure 7.5. Science target light path for the Gemini ALTAIR AO system. (Herriot et al. 1998)

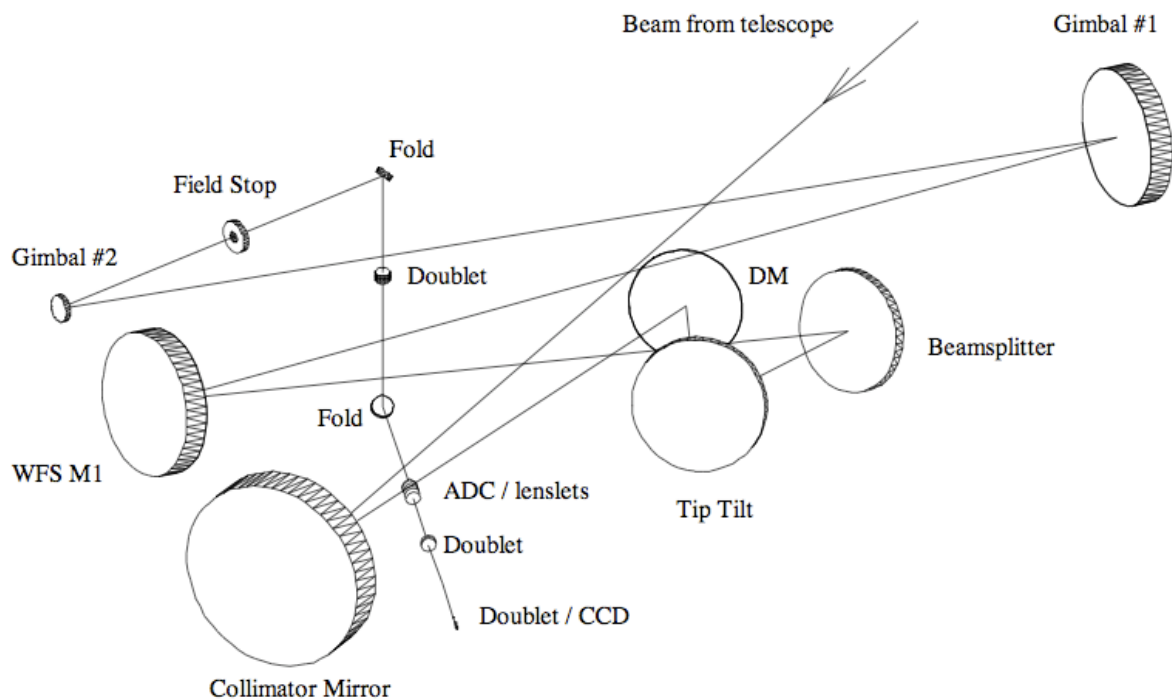


Figure 7.6. NGS light path for the Gemini ALTAIR AO system. (Herriot et al. 1998)

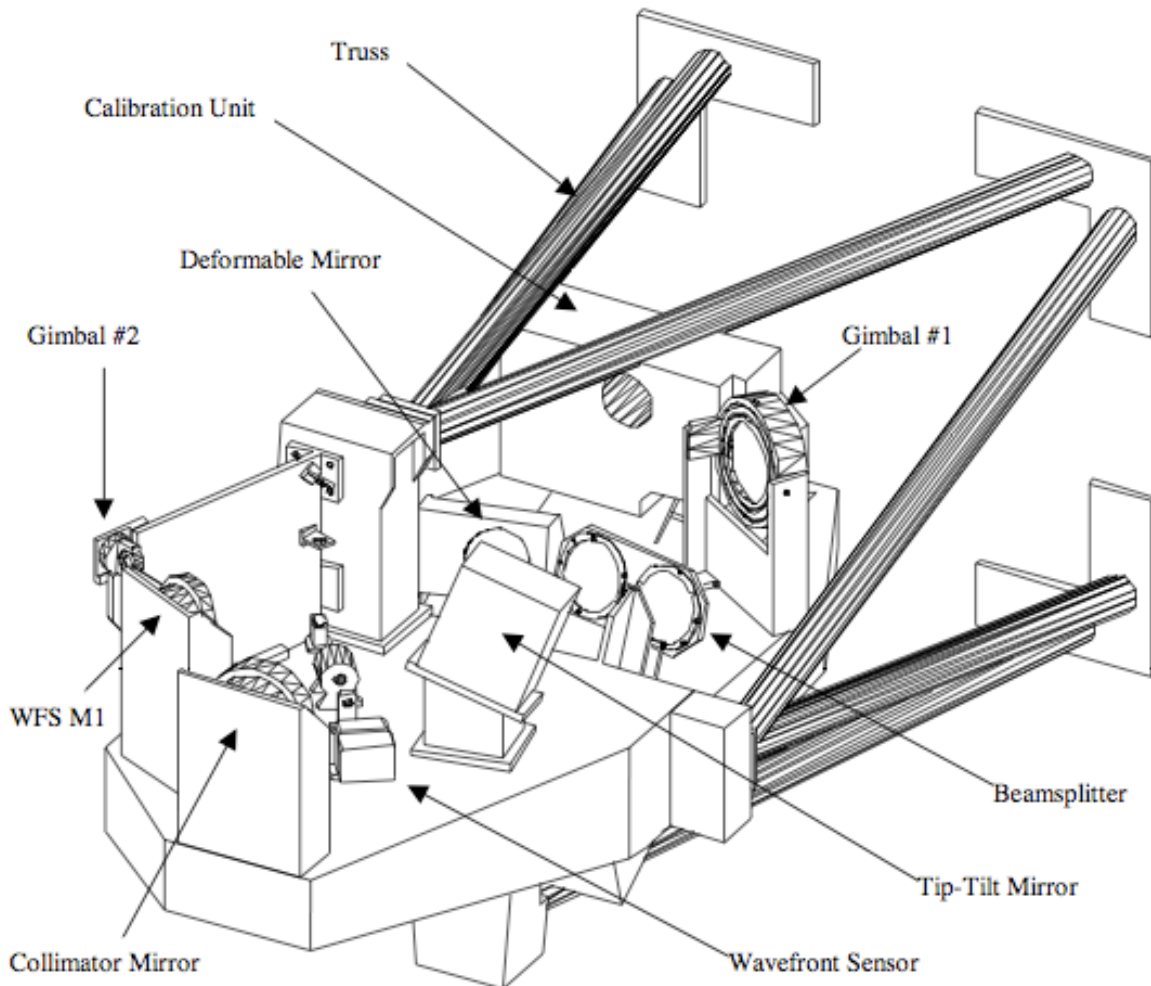


Figure 7.7. Mechanical configuration of the Gemini ALTAIR AO system. (Herriot et al. 1998)

A dichroic beamsplitter reflects 99% of the visible light between 0.4 and 0.83 μm wavelength. The reflected light passes through a reimaging system to a wavefront sensor (WFS). The WFS is a Shack-Hartmann type with 144 subapertures.

The beamsplitter transmits 97% of the near-infrared light between 0.85 and 2.5 μm wavelength. This light is sent to the science instrument, which is either a near-infrared imaging camera or a near-infrared spectrometer.

The Gemini AO control system is shown in Figure 7.8. The wavefront error (WFE) measured by the WFS is analyzed by a **reconstructor** algorithm to determine the drive signals that are sent to the DM and TTM. These are updated at a rate of 1 KHz.

The three low order modes, tip-tilt and focus (TTF) signals are filtered and the low-frequency trend is used to update the position of the telescope secondary mirror (M2) to eliminate focus and coma errors resulting from misalignment.

The 10 lowest order modes are also analyzed and used to update the shape of the primary mirror, which is actively controlled.

Also shown in Figure 7.8 is an on-instrument WFS (OIWFS) which measures tip tilt and focus, so that errors due to flexure of the instrument and optomechanical system can be corrected.

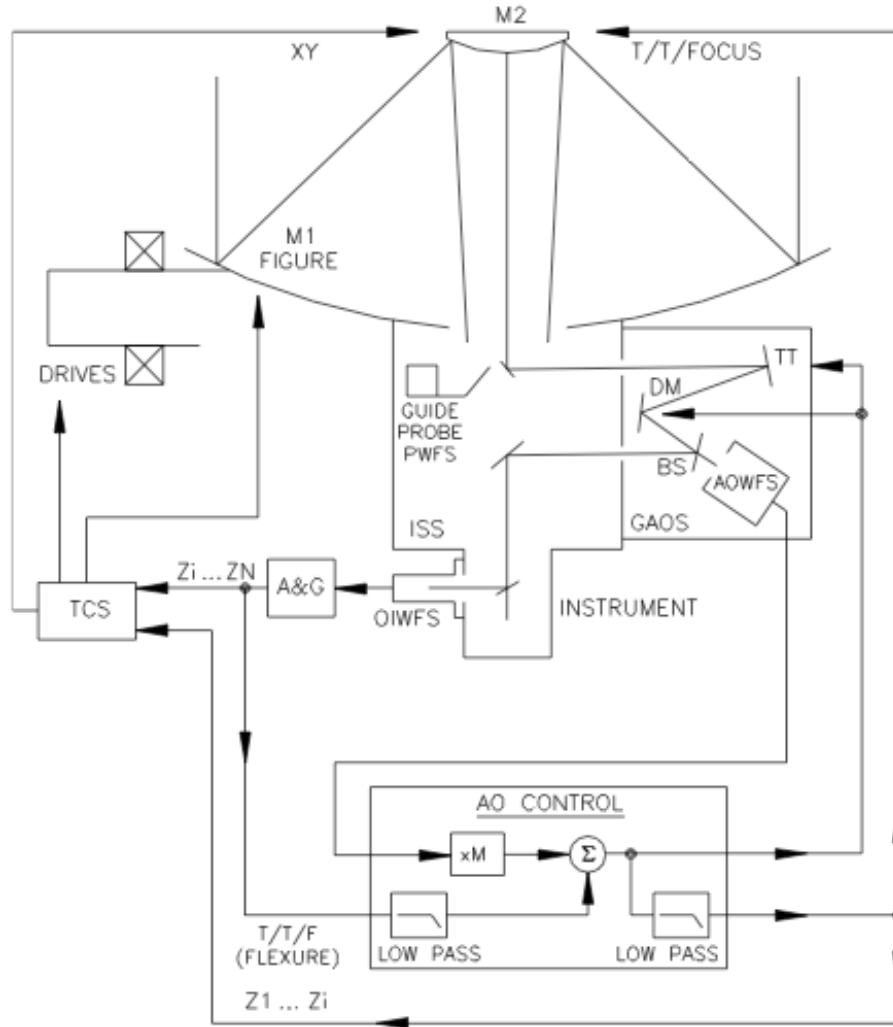


Figure 7.8. The ALTAIR AO control system, for NGS mode. (Herriot et al. 1998)

7.5. AO Performance

7.5.1. Error contributions

There are many independent factors that influence the performance of an AO system. The variances of these are all added to give the total wavefront phase variance of the system. Some of the most important ones are:

We have already seen that the isoplanatic error contributes a variance of

$$\sigma_\theta^2 = (\theta/\theta_0)^{5/3}. \quad (7.5)$$

The **DM fitting error** describes the residual wavefront error due to the finite size of a deformable mirror element,

$$\sigma_{DM}^2 = \mu(d/r_0)^{5/3}, \quad (7.6)$$

where d is the diameter of the element (projected back to the entrance pupil) and μ is a constant that depends on the type of deformable mirror. For a DM that uses discrete actuators attached to a continuous thin mirror, $\mu \simeq 0.28$.

The **servo lag error** results from the finite time required to measure the phase and update the DM,

$$\sigma_\tau^2 \simeq 0.28(\tau/\tau_0)^{5/3}, \quad (7.7)$$

where τ is the time lag.

Wavefront sensor measurement error σ_{WFS}^2 results from photon statistics and also detector read noise.

Non-common-path errors σ_{NCP}^2 arise from phase errors that occur within the AO system and instrument, due to the different paths taken by the science and NGS light after the beam splitter.

The total phase variance arising from these sources is

$$\sigma_\phi^2 = \sigma_\theta^2 + \sigma_{DM}^2 + \sigma_\tau^2 + \sigma_{WFS}^2 + \sigma_{NCP}^2. \quad (7.8)$$

From this, the Strehl ratio can be estimated using Eqn. (5.24),

$$S \approx \exp\{-[\sigma_\theta^2 + \sigma_{DM}^2 + \sigma_\tau^2 + \sigma_{WFS}^2 + \sigma_{NCP}^2]\}. \quad (7.9)$$

8. Laser AO

The very limited sky coverage available with conventional AO has motivated the development of laser AO. Here one uses a powerful laser to produce one or more artificial **laser guide stars** (LGS) in the atmosphere. These can be placed at any convenient location, greatly increasing the available sky coverage.

The lasers can be **continuous wave** (CW) or pulsed. Most current systems use CW lasers as these are simpler and provide a high return signal. Pulsed lasers can provide information about the range to the guide star, but are more complex and generally have lower power levels.

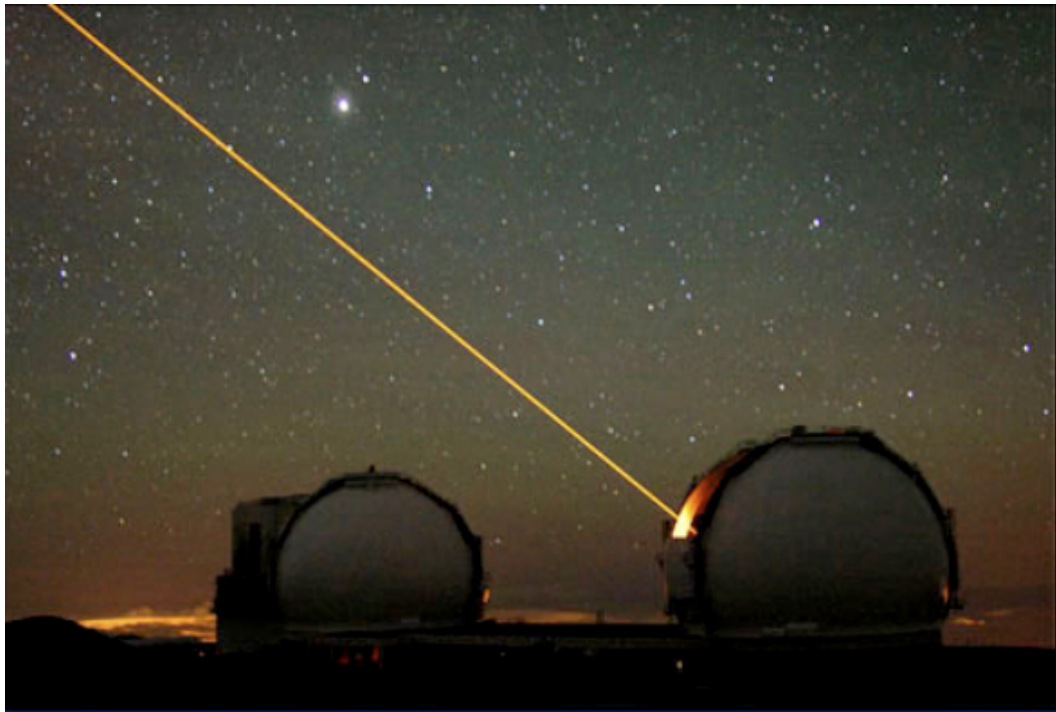


Figure 8.1. Rayleigh scattering from the beam of this sodium laser at the Keck observatory is readily visible to the eye. (Credit: Claire E. Max, UCSC).

8.1. Rayleigh and sodium laser systems

A Rayleigh laser system uses the light returned from the lower part of the atmosphere, primarily by Rayleigh scattering (Figure 8.1). This provides a return signal that extends to a maximum height of about 30 km.

Sodium laser systems are tuned to the strong D₂ resonance line of atomic sodium at a wavelength of 589 nm.

Both laser systems can be either CW or pulsed. Pulsed lasers have the advantage that detection can be made synchronously. By gating the detector, low-altitude Rayleigh light can be blocked, and the effect of elongation due (see below) can be mitigated.

8.2. Limitations

8.2.1. Tip-tilt

Both Rayleigh and sodium lasers systems have a fundamental limitation. *They cannot sense tilt modes of the atmosphere.* This is because transmitted and received beams are both affected in the same manner by atmospheric tilt (Figure 8.2).

8.2.2. Focal anisoplanatism

LGAO systems suffer from two geometrical effects that reduce performance. The first is *focal anisoplanatism*, commonly known as the *cone effect*. Light from the science target (a very large distance away) passes through regions of the atmosphere that are not traversed by light from the beacon. Thus turbulence in these regions is not sensed, or corrected, by the AO system. This is discussed further in Section 9.

The cone effect is worse for Rayleigh systems as the beacon is closer to the telescope.

8.2.3. LGS elongation

A second problem is *laser guide star elongation*. This affects both Rayleigh and sodium systems, although the latter less so. Because light scatters from all along the laser beam, the beacon is actually a cylinder of light. If seen from any direction other than exactly end-on, it will appear elongated (Figure 8.3). This reduces the accuracy with which the turbulence can be sensed.

Elongation can be reduced by projecting the laser beam from the centre of the telescope aperture. This can be done by means of a small mirror located behind the telescope's secondary mirror.

With large telescopes elongation remains a problem even when the laser is centrally projected. This is because the outer regions of the telescope aperture view the laser beacon obliquely.

Sodium beacons are less affected by elongation due to their greater distance, typically 90 km. However the sodium layer has a finite thickness, typically ~ 10 km, so elongation remains a problem for large telescopes.

Elongation can be reduced by the used of pulsed lasers. By gating the WFS synchronously with the laser pulse, one can block the light returned from the lower altitudes.

8.3. Properties of the sodium layer and effects of variability

Atomic sodium is found in the mesosphere in a region extending typically from an altitude of 70 to 120 km. The highest density is centred around 90 km and is typically about 10 km thick.

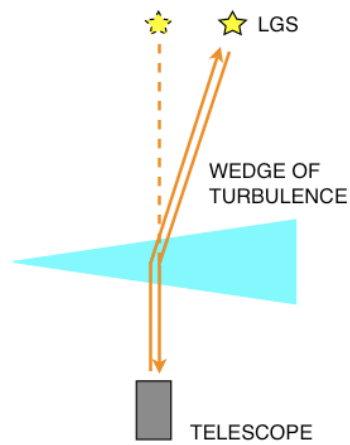


Figure 8.2. Laser guide stars are blind to atmospheric tilt components. Because the transmitted and received beams are both bent by the same amount, the apparent position of the LGS is unchanged.

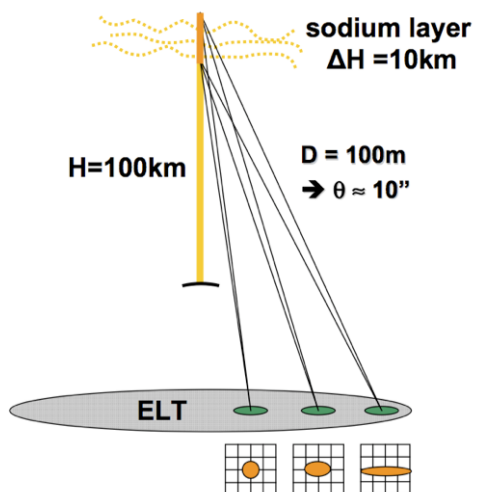


Figure 8.3. LGS elongation. Subapertures in the outer part of the pupil of a large telescope see an elongated beacon. (ESO)

It is believed that the sodium atoms (and also potassium, magnesium, etc) are deposited at the top of the layer by vaporization of meteors. Chemical reactions, occurring at the bottom of the layer remove the atomic sodium, so the layer is dynamic, with large fluctuations in density structure and altitude (Figure 8.4).

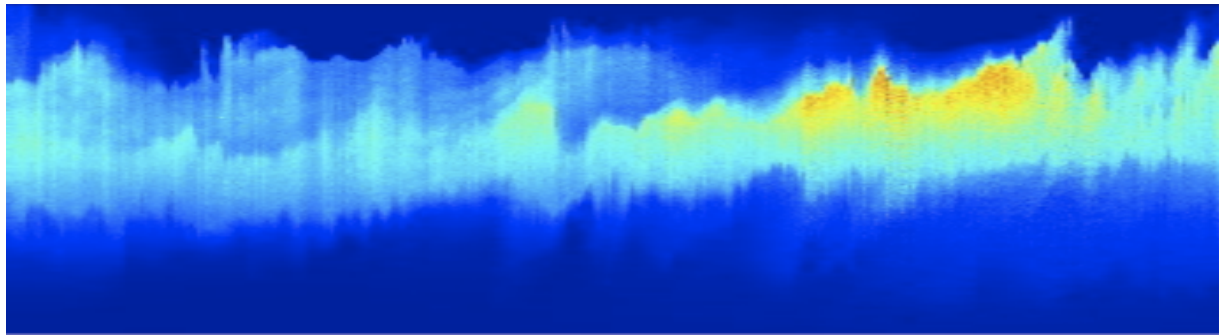


Figure 8.4. Vertical density profile of the sodium layer as a function of time. The vertical axis ranges from 80 - 100 km and the horizontal axis covers a period of 6 hours. These data were obtained with the Purple Crow lidar system of the University of Western Ontario. (Herriot et al. 2006).

With large telescopes, LGS elongation is significant, even with sodium beacons. To reduce this, the laser beam is launched along the telescope axis, typically from behind the secondary mirror. Nevertheless, the outer parts of the entrance pupil receive the laser light obliquely, so the LGS appears elongated. For the outermost subapertures of a 30-m telescope, the elongation is several arcsec.

Elongation reduces the accuracy with which the wavefront phase can be determined. For example, in a Shack-Hartmann detector, the image produced by each lenslet is elongated. This makes centroiding less accurate. Also, because the sodium density profile has fluctuating internal structure (Figure 8.4), so does the LGS. This structure causes fluctuations in the position of the centroid which are then misinterpreted as changes in the local wavefront slope.

These problems can be reduced by the use of matched-filter type algorithms



Figure 8.5. Sodium lidar at the 6-m liquid mirror Large Zenith Telescope, near Vancouver, Canada, will provide high-resolution density profiles of the sodium layer.

(Conan et al. 2007), but there is nevertheless an inevitable loss of performance.

A potentially more serious problem is confusion caused by rapid fluctuations in the mean height of the sodium layer. If the mean height changes, this is seen by the WFS as a change in wavefront curvature - a focus error. This cannot be distinguished from a true focus change produced by atmospheric turbulence. If the AO system then moves the DM to correct the perceived focus change caused by a change in the sodium height, light from the science target will be thrown out of focus!

The seriousness of this problem depends on the rapidity of sodium height variations. Since atmospheric fluctuations occur on a timescale on the order of milliseconds (τ_0), if sodium height fluctuations occur much more slowly than this, they can be separated by temporal filtering (Herriot et al. 2006).

Existing sodium lidar data do not have sufficient temporal resolution to measure sodium variability on ms time scales, although extrapolation of current data indicates that these fluctuations may be a significant source of error for AO systems on extremely-large telescopes (ELTs) since the error grows in proportion to D^2 (Davis et al. 2006). New measurements are in progress to better determine the temporal properties of the sodium (Chun et al. 2008, Pfrommer et al. 2008).

9. Advanced AO concepts

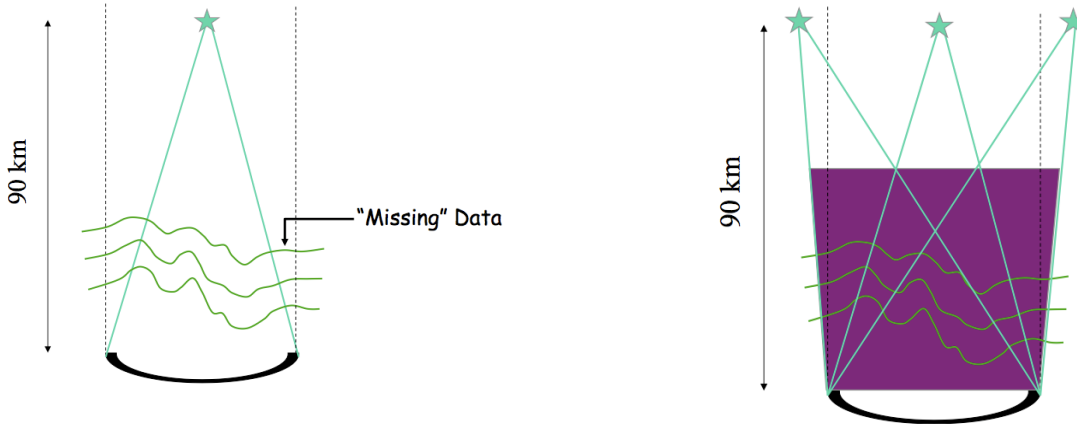


Figure 9.1. Illustration of the cone effect (left). Turbulence in the region indicated by the arrow is not sensed by light from the sodium laser beacon. The problem can be corrected by using multiple LGS (right). (Andy Foster, Observatory Sciences Ltd.)

As Figure 9.1 shows, because of focal anisoplanatism (the cone effect) a single LGS provides incomplete information about the turbulence affecting light from the science target.

The aim of atmospheric tomography is to use multiple guide stars to improve our knowledge of the instantaneous turbulence structure above the telescope by probing different lines of sight.

This knowledge can then be applied in several ways:

- MCAO (*multiconjugate adaptive optics*) - phase correction is applied to two or more DMs conjugated to different *heights* in the atmosphere
- MOAO (*multiobject adaptive optics*) - phase correction is applied to multiple DMs, one for each target direction (ie object).
- GLAO (*ground-layer adaptive optics*) - phase correction is applied to single DM, conjugated at low altitude, to cancel effects of the ground layer only.

9.1. Atmospheric tomography

We have seen that light propagating through the atmosphere develops phase errors from atmospheric turbulence. This turbulence is generally confined to distances on the order of 10 km or less. Therefore, the Fresnel scale $L_F = \sqrt{\lambda z}$ is at most ~ 7 cm at a wavelength of 0.5 um and therefore less than r_0 . At longer wavelengths this will still be true since r_0 grows faster than L_F with wavelength. Therefore, to a good approximation, we can neglect diffraction effects for AO applications.

Also, we can neglect log-amplitude fluctuations as these are much smaller than phase fluctuations in astronomy. (They can be large for horizontal observations through strong daytime turbulence.)

Therefore, the phase error in a particular direction is given by the integral of the optical path differences along the line of sight

$$\varphi(\mathbf{r}) = \int_0^\infty n(\mathbf{r}, z) dz. \quad (9.1)$$

9.1.1. Fourier slice theorem

The Fourier transform of this gives the $f_z = 0$ component of the three-dimensional Fourier transform of the index of refraction fluctuations,

$$\begin{aligned} \tilde{\varphi}(\mathbf{f}) &= \int_0^\infty \tilde{n}(\mathbf{f}, z) dz, \\ &= \int_{-\infty}^\infty \tilde{n}(\mathbf{f}, z) \exp(-2\pi iz \cdot 0) dz, \\ &= \tilde{n}(\mathbf{f}, 0). \end{aligned} \quad (9.1)$$

Therefore, each WFS measurement gives a 2-dimensional slice through the 3-dimensional Fourier space of \tilde{n} (see Figure 9.2). With many such slices in different directions, one can build up an estimate of $\tilde{n}(\vec{f})$.

9.2. MCAO

Multi-conjugate adaptive optics (MCAO) is a new technique which greatly extends the performance of AO. By combining multiple WFS and multiple DMs, conjugated to turbulence over a range of altitudes, the isoplanatic angle can be increased by as much as an order of magnitude, providing a wider field of view and more uniform image quality.

Figure 1.9 illustrates the performance gain that can be achieved even with a relatively simple dual-conjugate MCAO system.

The fundamental breakthrough of MCAO is that if phase errors are corrected by a DM that is conjugate to the turbulence that produces them, then the correction will be achieved over a wide field angle. This improves the uniformity of image quality, and the area of sky that can be observed with a single pointing.

If there are multiple layers of turbulence, then multiple DMs are required to correct it, and multiple WFS are needed to sense the turbulence. The principle is illustrated in Figure 9.3, for the case of two turbulent layers.

In reality, the distribution of turbulence is continuous. However, it is strongest near the ground, and again at a height of approximately 12 km. Thus a dual-conjugate system employing two DMS, one conjugated

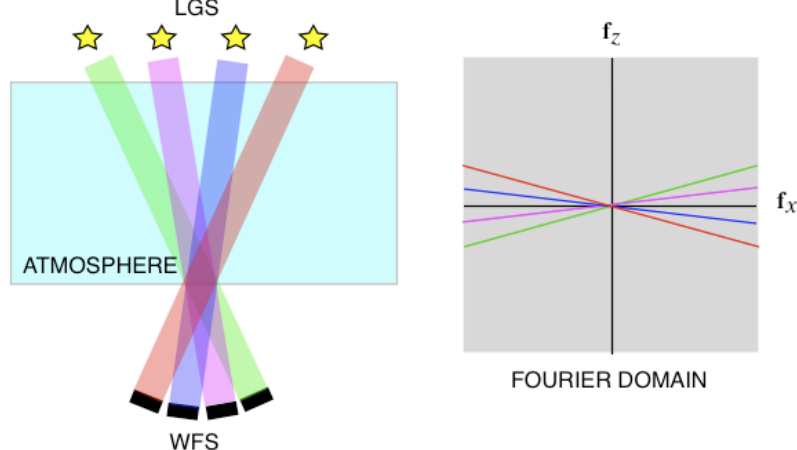


Figure 9.2. Fourier slice theorem. Each guide star provides a 2-d image that is the integral of the turbulence along a particular direction. The Fourier transform of this image represents a 2-d slice through the 3-d Fourier domain of the atmospheric turbulence. With enough slices, one can estimate the 3-d Fourier transform of the turbulence over the range spanned by the slices.

at low altitude and the other conjugate to the high-altitude, is quite effective.

9.3. MOAO

Multiobject adaptive optics is a new concept in AO. The idea is to not try to correct the wavefront over the entire field of view, but only in directions of particular science targets (Figure 9.4).

This can be done by incorporating a DM into the optics that feeds each individual imager or integral field unit (IFU) spectrometer, which are deployed robotically to the positions of interest.

Tomographic measurements based on WFS measurements of multiple guide stars are used to predict the wavefront error in the direction of each object.

The individual DMs are then used to correct the predicted error by open loop control (no feedback is possible from the individual probes as there are no LGS deployed in the directions of the science targets).

An advantage of this scheme is that a wide field of view can be covered, because only small regions need to be corrected.

9.4. GLAO

The aim of ground-layer adaptive optics (GLAO) systems is to partially correct atmospheric turbulence over a wide field of view.

Low altitude (ground-layer) turbulence affects all directions nearly equally (see Figure 9.4). Therefore, if one provides a wavefront correction appropriate to the ground layer only, the isoplanatic angle will be large.

Because the high-level turbulence is not being compensated, the Strehl ratio will be poor. Nevertheless, the seeing will be improved and there will be a significant reduction in image blur.

Models indicate that a reduction of FWHM by about a factor of two, in the K band, can be achieved over a field of view of 10 arcmin.

9.5. Polychromatic AO

Foy et al. (1995) first proposed a technique to overcome the problem that LGS cannot provide wavefront tilt information. The idea is to induce mesospheric sodium atoms to emit photons at more

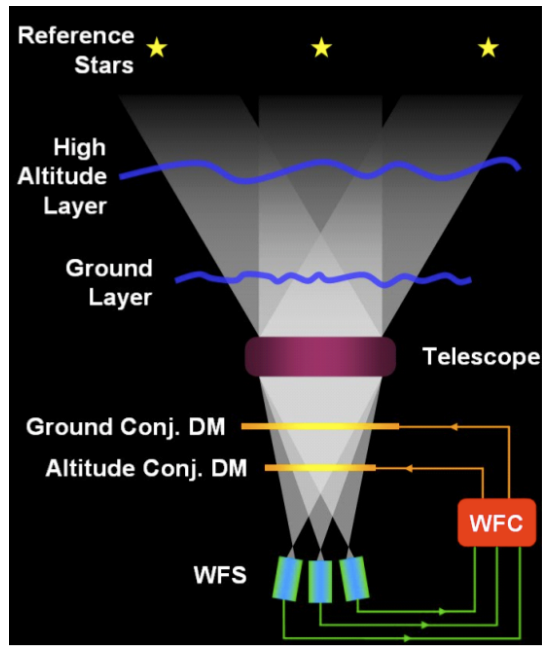


Figure 9.3. In an MCAO system, multiple deformable mirrors greatly increase the isoplanatic angle by compensating two or more turbulent layers. (European Southern Observatory)

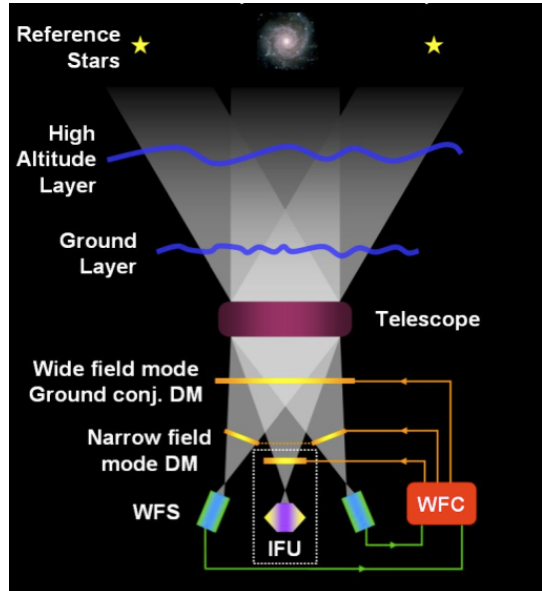


Figure 9.4. An MOAO system uses a separate deformable mirror for each science target. These are operated in open-loop mode based on measurements from several laser beacons. (European Southern Observatory)

than one wavelength. By detecting both wavelengths, it is possible to determine the magnitude and direction of the atmospheric tilt component.

This takes advantage of the fact that the index of refraction of air has a small dependence on wavelength. This is usually ignored in AO, but is significant for short wavelengths. Thus, short wavelengths are refracted more when passing through the atmosphere.

A tilt component can thus be distinguished by a difference in apparent position of the LGS at two different wavelengths. From this difference, the absolute tilt can be determined.

Sodium can be excited to a higher energy level by combining two lasers operating at 589 and 569 nm. The emitted radiation then includes ultraviolet light at a wavelength of 330 nm.

The advantage of this is that there would be no need for natural guide stars at all. Thus the sky coverage would be 100%.

Several groups are presently pursuing this idea.

9.6. Extreme AO and high-contrast imaging systems

Extreme AO systems aim to provide very high-order correction of the wavefront in order to reduce light diffracted by residual wavefront errors (Figure 9.5).

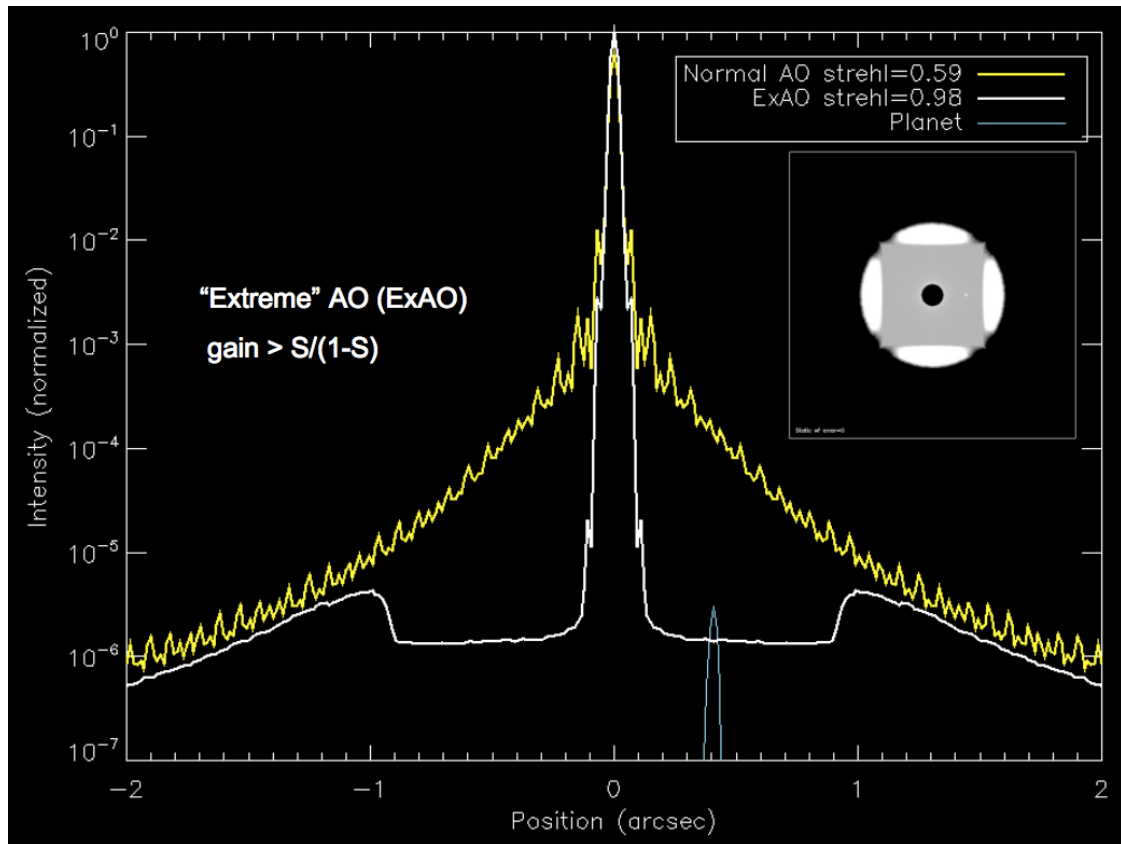


Figure 9.5. PSF of an ExAO system, compared to conventional AO. (Bruce Macintosh, LLNL)

The goal is to reduce this scattered light to very low levels in order to detect faint companions to bright stars (eg. planets).

Extreme AO systems employ deformable mirrors having a very high actuator count and wavefront sensors with many subapertures in order to reduce the fitting error.

They are limited to relatively bright stars, which can provide enough photons to provide high-resolution measurements of the wavefront.

This is combined with conventional methods for reducing scattered light that have been developed for coronagraphy. These include a baffle (called a *Lyot stop*) located at an intermediate pupil image to block light diffracted from obstructions such as the secondary mirror support spider.

In addition, *nulling interferometry* may be employed to cancel light from the star by means of destructive interference.

Systems currently under development, such as the Gemini Planet Imager (GPI), and the VLT planet finder (SPHERE) are expected to detect planets with a contrast ratio of $\sim 10^6$, to as high as $\sim 10^8$, compared to their host stars.

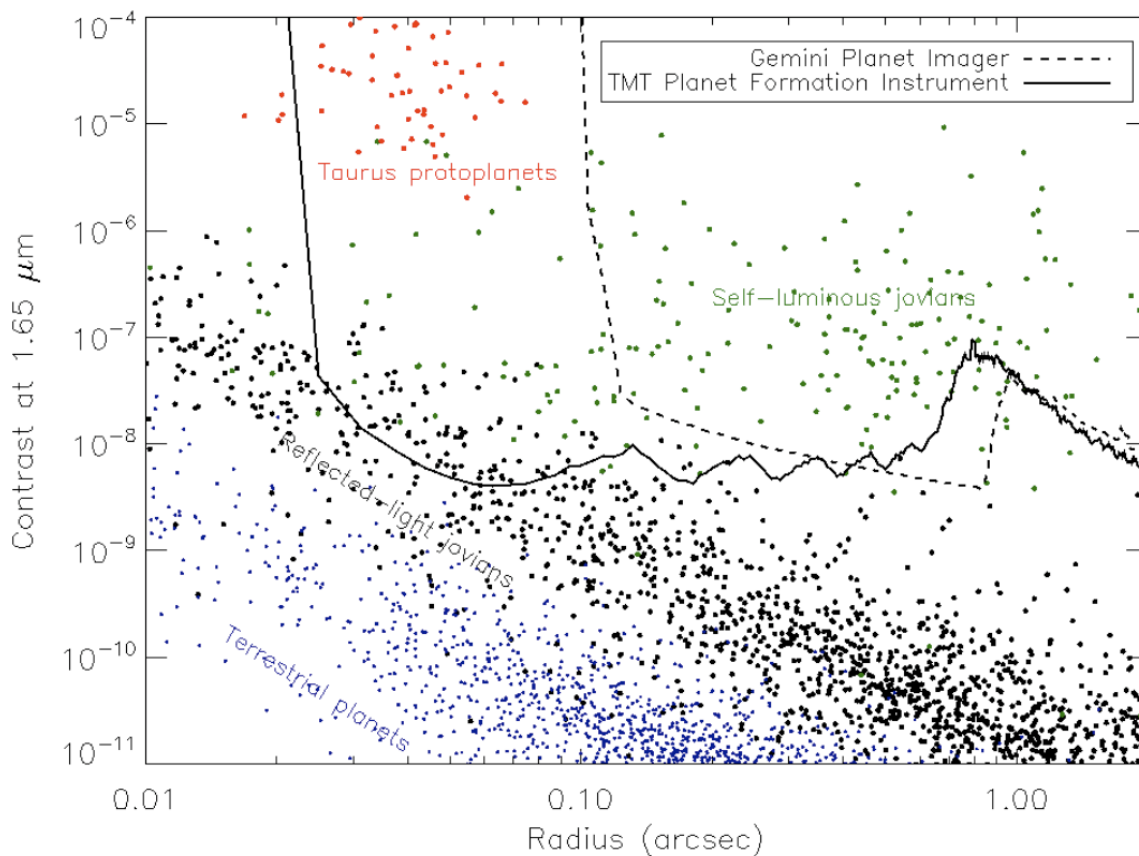


Figure 9.7. Discovery space for ExAO systems. The curves show detection limits for GPI on the 8-m Gemini South telescope and PFI on the Thirty Meter Telescope. (Bruce Macintosh, LLNL)

10. Astrometry and photometry with AO

Adaptive optics has the potential to provide enormous gains in sensitivity, photometric accuracy, and astrometric accuracy. However, this comes with limitations and the peculiarities of AO images must be understood and correctly accounted for in any analysis.

10.1. The AO PSF

From Eqn. (5.24), we see that the Strehl ratio is determined by the residual (uncorrected) wavefront error. What is the effect of these residual errors on the PSF? This depends on the spatial distribution of the phase fluctuations across the pupil. These fluctuations will generally have the same characteristic scale as the original atmospheric errors, and therefore will produce a contribution to the PSF that looks very much like a seeing-limited PSF, but containing less energy than a purely seeing-limited image.

So, the AO PSF is the sum of two components:

A diffraction-limited component with $FWHM \sim \lambda/D$ and an atmospheric component with $FWHM \sim \lambda/r_0$. This is illustrated in Figure 10.1.

The fraction of light contained in the diffraction-limited component is $\sim S$, while the fraction of light in the atmospheric component is $1 - S$.

The PSF is not constant across the field of view. Because of anisoplanatism, the Strehl ratio (and therefore the fraction of energy in the diffraction core) decreases with angle from the reference star.

10.2. Performance gains with AO

Many, perhaps most, astronomical observations target faint unresolved, or partially resolved, objects that need to be detected and measured in the presence of a relatively bright sky background (more precisely, a “foreground”). In these cases,

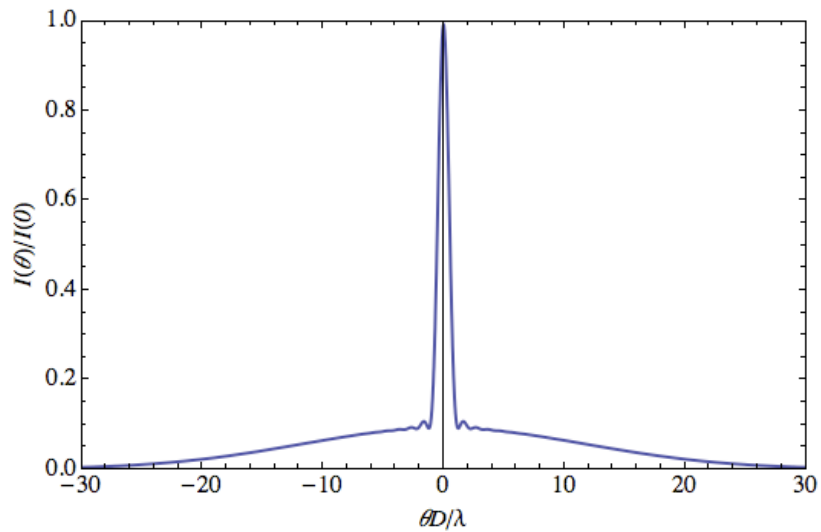


Figure 10.1. PSF of an AO system delivering a Strehl ratio of 0.01 with $D/r_0 = 20$. A diffraction limited core is embedded in a diffuse seeing-limited halo. The core has high contrast, but contains only 1% of the light in this case.

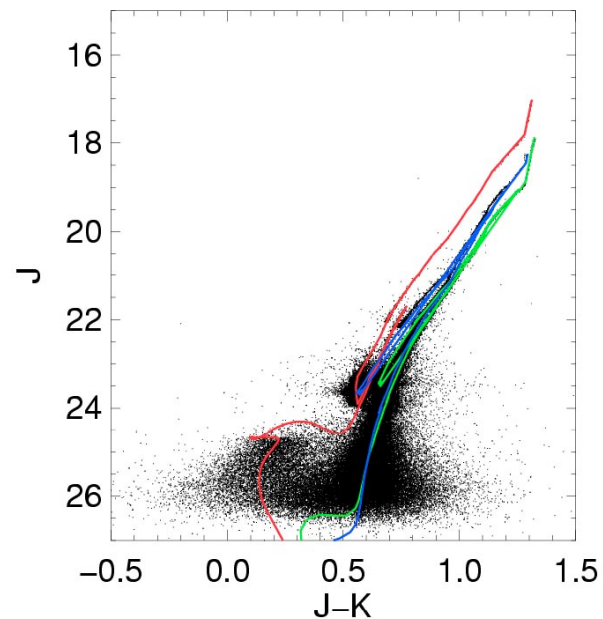


Figure 10.2. Simulation of MCAO photometry of stellar populations. (Knut Olsen, NOAO)

the dominant source of noise is usually photon statistics of the background light.

10.2.1. Photometry

AO provides a large gain by improving the resolution. For a point-like source, the FWHM goes from λ/r_0 to λ/D . Thus, the amount of background light contaminating the image is reduced by a factor of $(D/r_0)^2$ and the signal-to-noise ratio (SNR) is improved by a factor of D/r_0 . This can be more than an order of magnitude with a large telescope.

For partial AO correction, the fraction of light in the diffraction core of the image is $\sim S$, the Strehl ratio. Therefore the gain in signal-to-noise ratio provided by AO is SD/r_0

$$\frac{SNR_{AO}}{SNR_{NOAO}} \approx \frac{SD}{r_0}. \quad (10.1)$$

An example of simulated MCAO photometry of a crowded stellar field is shown in Figure 10.2.

10.2.2. Astrometry

With astrometry, we are concerned with accurately measuring the positions of objects. Again, the objects are often point like.

It is easy to show that the position error, due to random noise, in the measurement of a point-like object is

$$\sigma_\theta \approx \frac{\vartheta}{SNR}, \quad (10.2)$$

where ϑ is the FWHM of the image. AO provides a two-fold gain here. First, the FWHM is decreased by AO, by the ratio r_0/D . Second, the SNR is increased by a factor of SD/r_0 (Eqn. 10.1). Thus the position error is reduced by a factor of

$$\frac{\sigma_{\theta AO}}{\sigma_{\theta NOAO}} \approx \frac{1}{S} \left(\frac{r_0}{D} \right)^2. \quad (10.3)$$

This is a very large factor, more than two orders of magnitude for a large telescope.

Precise AO astrometric measurements have allowed the accurate determination of stellar orbits in the galactic centre and the determination of the position and mass of the galactic super-massive black hole (Figure 10.3). with the Keck laser AO system, an astrometric accuracy of 150 microarcsec (uas) has been achieved.

A fundamental limit to astrometric accuracy comes from the atmosphere. Atmospheric turbulence causes variations in the image scale, which fluctuate at the atmospheric time scale. This produces a fluctuating geometric distortion of the field of view, causes the relative positions of stars to move.

This atmospheric contribution to the error can be reduced by averaging - either by exposing longer or coadding individual exposures. So, it decreases as $t^{-1/2}$.

MCAO can reduce this atmospheric error further. With two or more DMs conjugated at different altitudes, variations in image scale can be induced which cancel those of the atmosphere, at the positions of the LGS. Effectively, the field of view is “pinned” at these locations by the AO system. Residual

atmospheric distortion increases away from the LGS, but its value is much lower, typically by an order of magnitude, than with no AO.

It has been estimated that 30-m class telescopes equipped with MCAO might achieve an astrometric precision as low as 10 uas.

10.3. Limitations arising with AO

10.3.1. Photometry

An obvious issue with AO arises from the form of the PSF (Figure 10.1). Unless the Strehl ratio is very high, a significant amount of light ends up in a diffuse halo surrounding the objects. This complicates photometric measurements because the halo looks like a spatially-varying background. Thus sky subtraction is more difficult.

The best way to deal with this is by PSF fitting techniques, where the halo is explicitly included. However the large difference in angular scale between the diffraction core and the halo (a factor of D/r_0) makes this challenging.

A second problem arises due to the variation in the Strehl ratio across the field of view. It is highest close to the guide star(s) and generally lower elsewhere. The uniformity is better with MCAO, but the variation is still significant, and hard to predict. Thus, the photometric algorithm needs to be capable of dealing with spatially-varying PSFs.

Determining the precise form of the PSF is also an issue. Where there are stars, it can be measured. But with few stars (a field of galaxies at high galactic latitude, for example) this can be a problem. In principle it should be possible to predict the PSF by recording the WFS measurements throughout the observation. But, this has not yet been demonstrated.

10.3.2. Astrometry

We have seen that astrometry can be much improved with AO, but one must also keep in mind the limitations. While MCAO can reduce the atmospheric geometric distortion, it can also introduce distortion of its own. The system tries to maintain the positions of the LGS fixed. But, this is only as good as the geometric stability of the system. If the positions of the optical elements that receive light from the LGS and pass it to the WFS change, a corresponding distortion will be introduced into the image from the science camera.

Thus, AO has great potential and has already made substantial gains. Further progress will require care and attention to detail in the design of future AO systems.

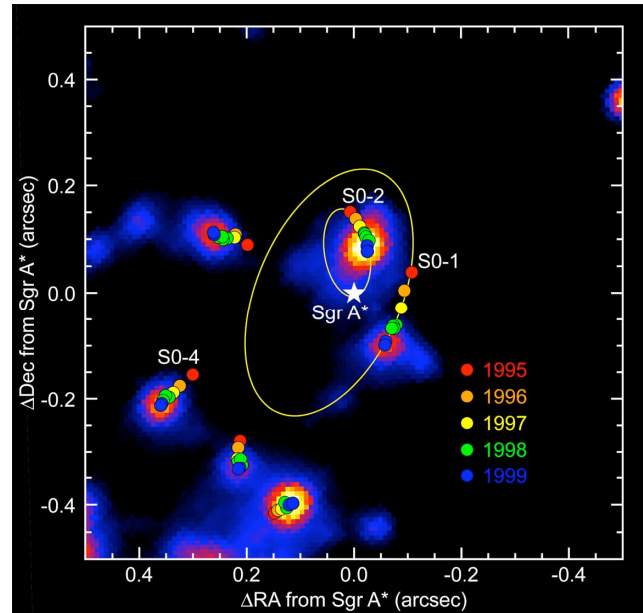


Figure 10.3. Image of the galactic centre obtained with the Keck laser AO system, showing motion of the stars. (Andrea Ghez, UCLA)

11. ELT AO systems

Extremely-large telescopes (ELTs) will make extensive use of adaptive optics. AO is essential to allow these telescopes to achieve their full scientific potential.

With AO, the resolution of a telescope increases in proportion to its diameter. And, the sensitivity for the detection of point sources increases in proportion to the diameter to the fourth power. This is a tremendous factor, making a 30-m ELT ~ 100 times more sensitive than the Keck telescopes or the VLT.

11.1. Thirty Meter Telescope (TMT)

The Thirty Meter Telescope (TMT) is one of several ELTs currently under development (Figure 11.1). It will employ a 30-m diameter primary mirror composed of 492 segments.

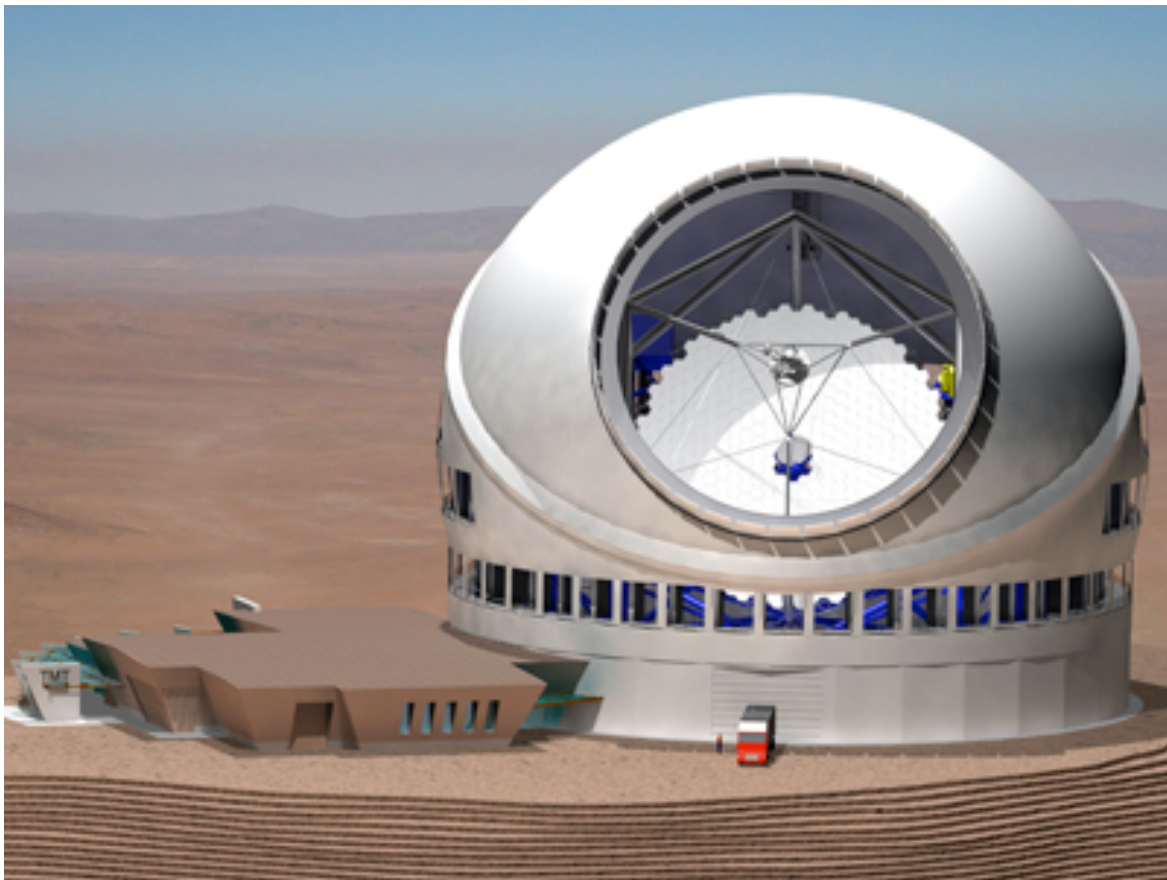


Figure 11.1. Extremely large telescopes such as the 30-m TMT will make extensive use of adaptive optics. (TMT)

The TMT will employ many AO systems:

- NFIRAOS (Narrow-Field InfraRed Adaptive Optics System) is the facility MCAO system.
- MIRAO (Mid-Infrared Adaptive Optics)
- MOAO (Multi-Object Adaptive Optics)
- ExAO (Extreme Adaptive Optics)
- GLAO (Ground-Layer Adaptive Optics)

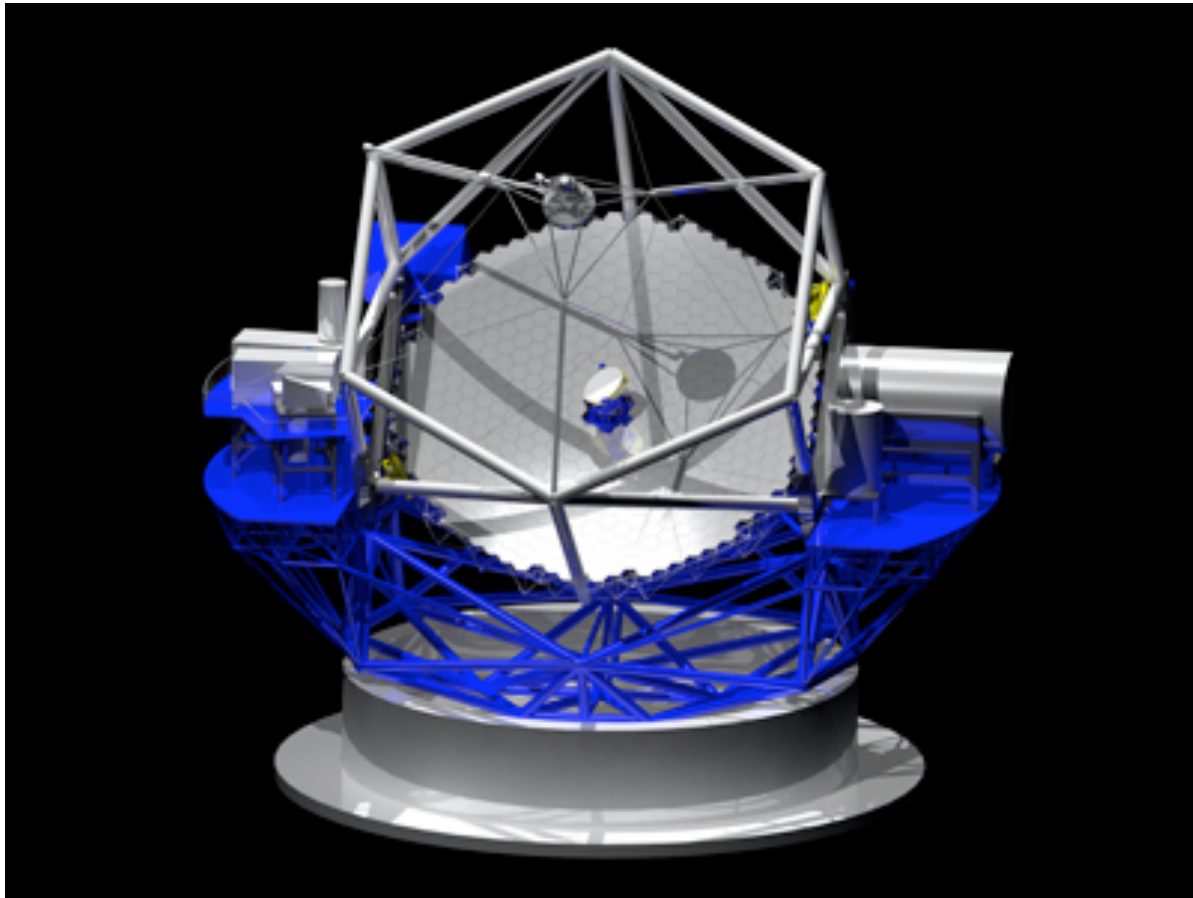


Figure 11.2. TMT will project laser beams from a launch telescope located behind the secondary mirror. The main AO system (NFIRAOS) is located on the Nasmyth platform on the left side of this representation. It receives light directed there from the tertiary mirror, visible at the center of the primary mirror. (TMT)

11.1.1. NFIRAOS

NFIRAOS will be the facility near-infrared AO system, providing corrected images to three instruments (IRIS, NIRE and WIRC). Located on the Nasymth platform, it receives light from the tertiary mirror and feeds any of three instruments (Figure 11.2). Its main characteristics are:

- It will operate in the 0.8 - 2.5 μm wavelength range.
- The corrected field of view will be 30 arcsec diameter.
- It employs two DMs, one conjugated at low altitude and the second at an altitude of 12 km.
- The residual wavefront error is expected to be ~ 190 nm, which corresponds to a Strehl ratio of 0.24 at a wavelength of 1 μm and 0.75 in the K band (2.2 μm).
- The sky coverage will be 50% at the galactic pole (limited by the availability of natural guide stars).

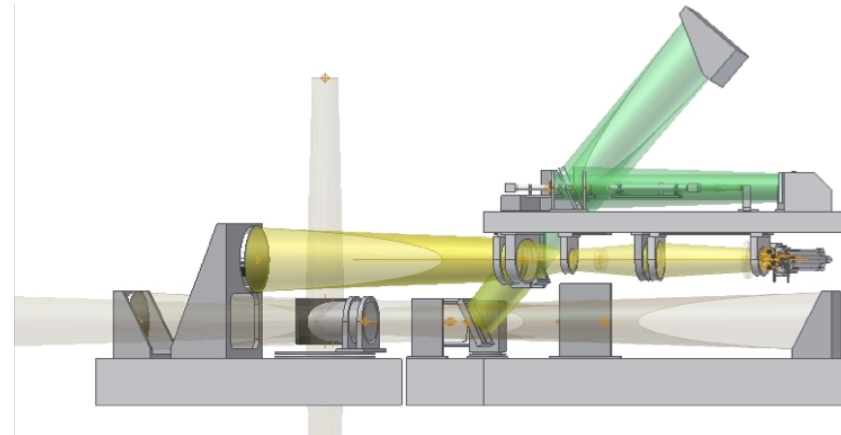


Figure 11.3. Optical layout of the TMT NFIRAOS MCAO system. (TMT)

11.1.2. IRIS

A first-light TMT instrument, the InfraRed Imaging Spectrometer (IRIS) is a combination imager and integral field spectrometer that will be used behind the NFIRAOS MCAO system (Figure 11.4).

With a 15 arcsec square field of view and 4 mas pixel size, it will be capable of studying the faintest and most distant objects at the diffraction limit of the TMT (Figure 11.5).

It will operate over a 0.8 - 2.5 μm wavelength range and provide spectral resolutions as high as 4000.

11.1.3. PFI

The TMT *Planet Formation*

Instrument (PFI) will employ ExAO and coronographic techniques to achieve a high contrast ratio for the study of exoplanets.

Figure 11.6 shows the optical layout and Figure 11.7 illustrates the expected performance of PFI.

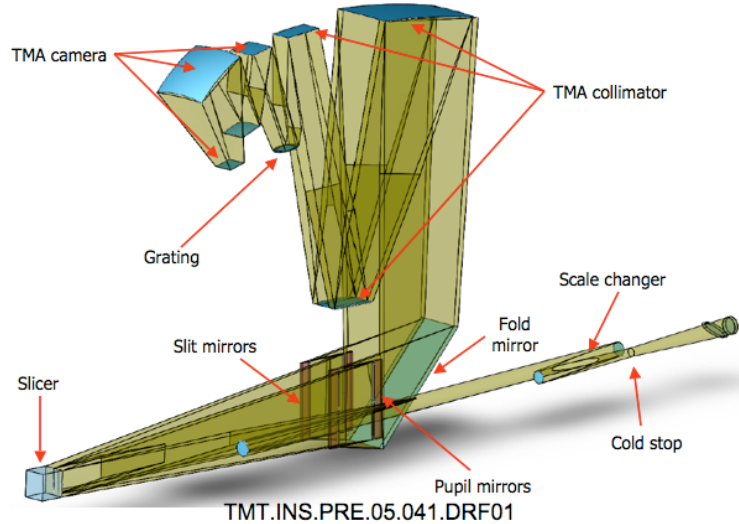


Figure 11.4. IRIS is a high-sensitivity imager and integral field spectrometer behind the NFIRAOS MCAO system. (TMT)

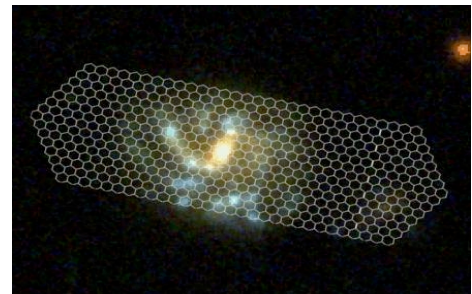


Figure 11.5. The IRIS IFU centered on a distant galaxy. (James Larkin, TMT)

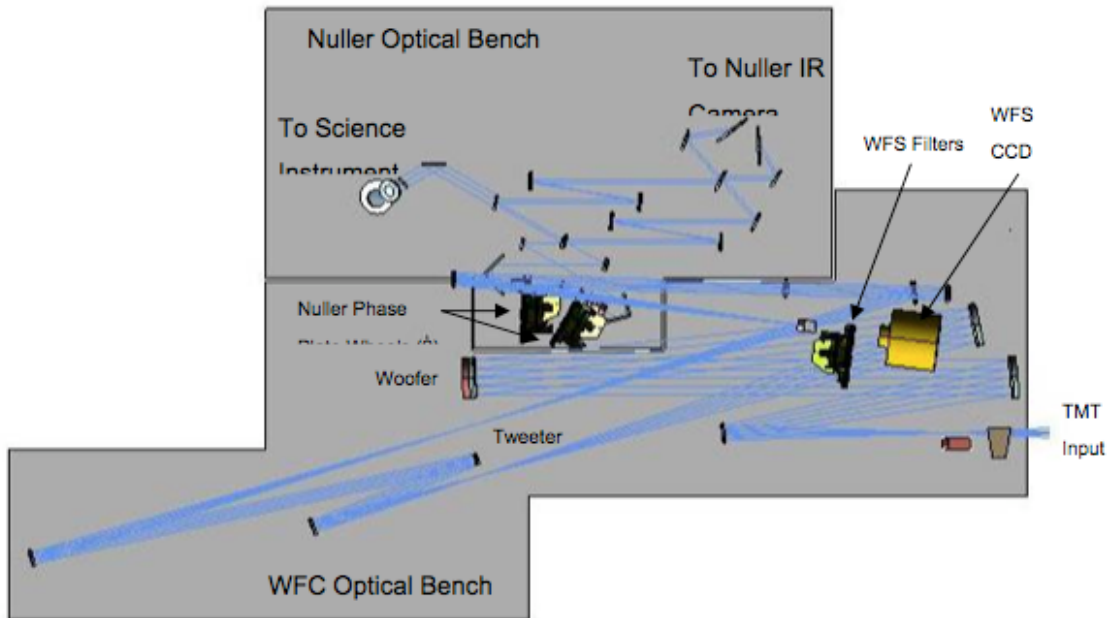


Figure 11.6. Optical layout of PFI. It combines an ExAO system and interferometric nullder to achieve a high contrast ratio. (TMT)

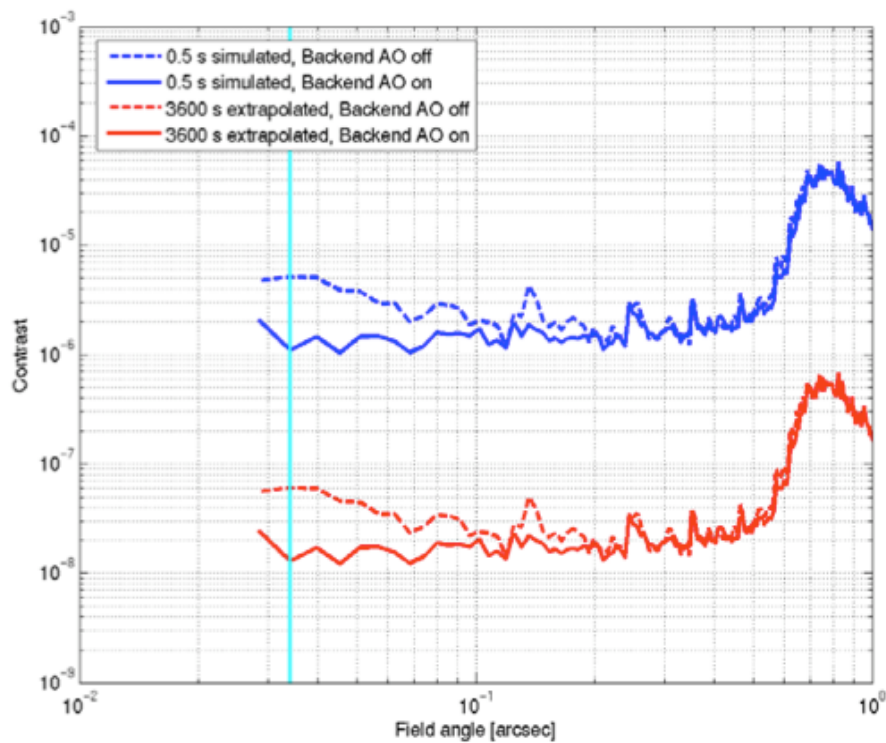


Figure 11.7. Projected performance of PFI for short and long exposure times. A contrast ratio of 10^8 may be achieved in a 1 hr integration time. (TMT)

11.1.4. IRMOS

The *InfraRed MultiObject Spectrometer* (IRMOS) will employ MOAO to provide wavefront correction to each of 16 deployable IFU probes. These can be positioned at the locations of objects of interest in order to obtain spatially-resolved spectrophotometry at close to the diffraction limit (Figure 11.8).

IRMOS will operate in the 0.8 - 2.5 μm wavelength range, probing a field of view as large as 5 arcmin diameter, and providing a spectral resolution of 2000 - 10000.

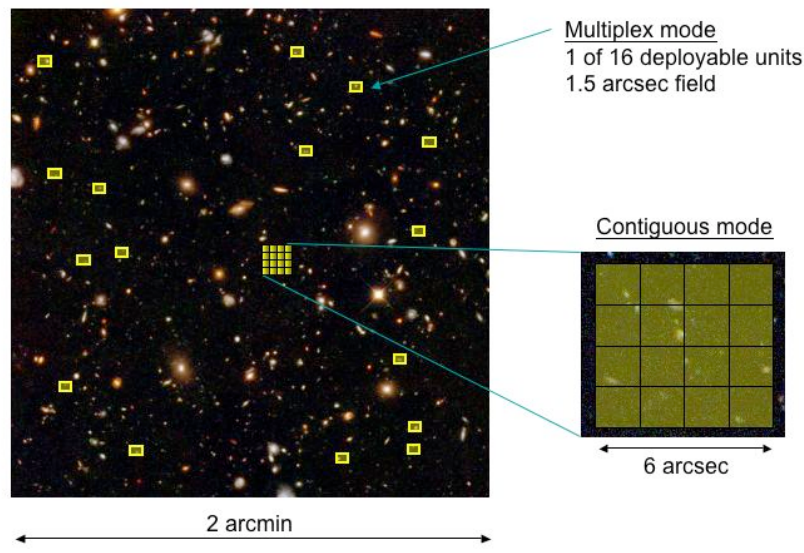


Figure 11.8. IRMOS, a multiobject integral field spectrometer employing MOAO (TMT)

11.1.5. WFOS

TMT's *Wide-Field Optical Spectrometer* (WFOS) will be capable of GLAO to provide a boost in sensitivity by image sharpening over a 20 arcmin field of view (Figure 11.9).

WFOS will operate over a 0.3 - 1.2 μm wavelength range.

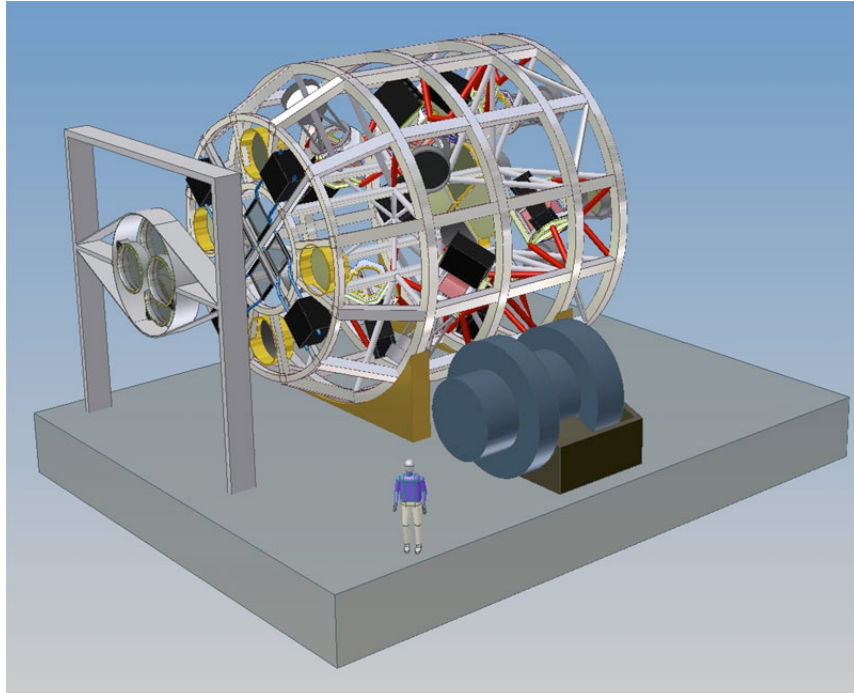


Figure 11.9. WFOS, a wide field multiobject optical/IR spectrometer employing GLAO (TMT)

11.1.6. MIRES

The TMT Mid-InfraRed Echelle Spectrometer (Figure 11.6) will provide high resolution ($R \sim 5000 - 100,000$) spectrophotometry over a 5 - 28 μm wavelength range.

It will employ conventional laser adaptive optics and will operate at the diffraction limit (Figures 11.10 and 11.11).

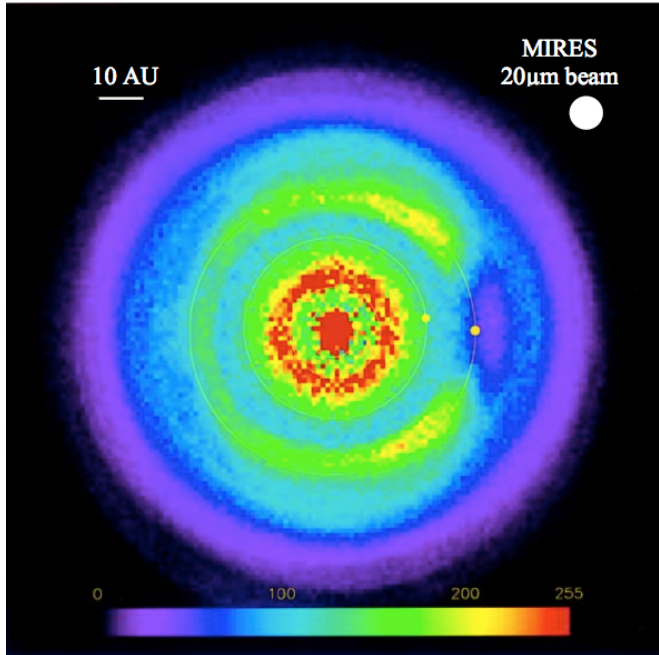


Figure 11.11. Simulation of a protoplanetary disk showing a massive accreting planet. With AO, MIRES will achieve a resolution 5 times better than that of JWST at mid-infrared wavelengths. (TMT)

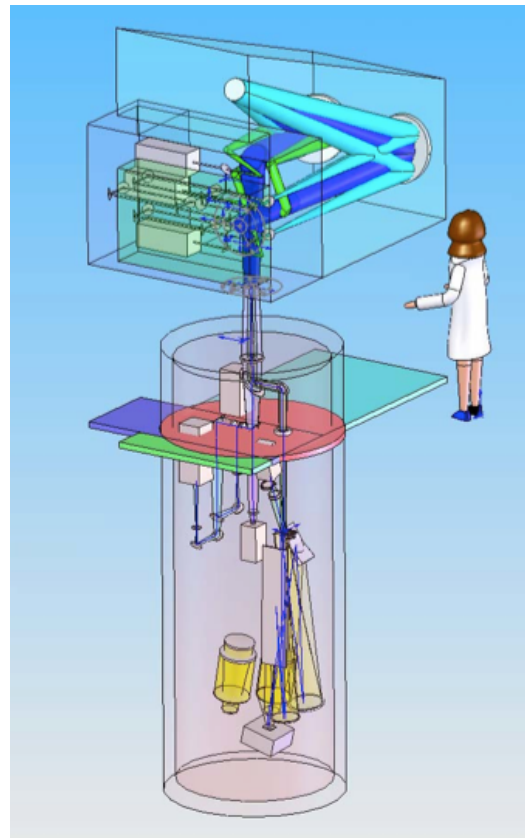


Figure 11.10. MIRES is a high-resolution mid-infrared echelle spectrometer employing a conventional laser AO system. (TMT)

References

- Andrews L, 2004, *Field Guide to Atmospheric Optics*, SPIE, Bellingham.
- Bouy H, Kolb J, Marchetti E, Martín E L, Huélamo N, Barrado y Bavascyés D, 2008, *Multi-conjugate adaptive optics images of the Trapezium cluster*, A & A, 477, 681-690.
- Born M, & Wolf E, 1999, Principles of Optics, 7th edition, Cambridge University Press, Cambridge.
- Buscher D F, Armstrong J T, Hummel C A, Quirrenbach A, Mozurkewich D, Johnston K J, Denison C S, Colavita M M, & Shao M, 1995, *Interferometric seeing measurements on Mt. Wilson: power spectra and outer scales*, Appl Optics, 34, 1081-1096.
- Chun M R, Wilson R W, Avila R, Butterly T, Aviles J-L, Rigaut F J, Ellerbroek B L, 2008, *High-temporal monitoring of a sodium laser guide star*, SPIE, 7015, in press.
- Colavita M M, Shao M, & Staelin D H, 1987, *Atmospheric phase measurements with the Mark III stellar interferometer*, Appl Optics, 26, 4106-4112.
- Conan R, Lardiere O, Jackson K, Herriot G, Bradley C, 2008, *Sodium LGS wavefront sensing test bench for the Thirty Meter Telescope*, SPIE, 7015, in press.
- Davis D S, Hickson P, She C-Y, Herriot G, 2006, *Temporal variability of the telluric sodium layer*, Optics Lett, 31, 3369-3371.
- Foy R, Migus A, Biraben F, Grynberg G, McCullough P, Tallon M, 1995, The polychromatic artificial sodium star: A new concept for correcting the atmospheric tilt, A & A Supp, 111, 569.
- Fried D L, 1965, *Statistics of a geometric representation of wavefront distortion*, JOSA, 55, 1427-1435.
- Fried D L, 1966, *Optical resolution through a randomly inhomogeneous medium for very long and very short exposures*, JOSA, 56, 1372-1379.
- Greenwood D P, 1976, Bandwidth specification for adaptive optics, JOSA, 67, 390-393.
- Greenwood D P, & Fried D, 1976, Power spectra requirements for wave-front-compensation systems, JOSA, 66, 193-206.
- Hardy J W, 1998, *Adaptive Optics for Astronomical Telescopes*, Oxford Univ Press, NY.
- Herriot G, Morris S, Roberts S, Fletcher M, Saddlemeyer L, Singh G, Veran J-P, Richardson, 1998, *Innovations in Gemini Adaptive Optics Systems Design*, SPIE, 2252, 488-499.
- Herriot G, Hickson P, Ellerbroek B, Véran J-P, She C-Y, Clare R, Looze D, 2006, *Focus errors from tracking sodium layer altitude variations with laser guide star adaptive optics for the Thirty Meter Telescope*, SPIE, 6272, 627211.
- Hickson P, 1994, *Wavefront curvature sensing from a single defocussed image*, JOSA A, 11, 1667-1673.
- Kolmogorov A N, 1941, Dan SSSR, 65, 291
- Kolmogorov A N, 1941, *Dissipation of energy in the locally isotropic turbulence*, Comptes rendus (Doklady) de l'Académie des Sciences de l'U.R.S.S., 32, 16-18.
- Kolmogorov A N, 1941, *The local structure of turbulence in incompressible viscous fluid for very large Raynold's numbers*, Comptes rendus (Doklady) de l'Académie des Sciences de l'URSS, 30, 301-305.
- Maréchal A, 1947, Rev d'Optique, 26, 257.
- Moffat A F J, 1969, A&A, 3, 455.
- Nightingale N S, Buscher, D F, 1991, *Interferometric seeing measurements at the La Palma Observatory*, MNRAS, 251, 155-166.
- Noll R J, 1976, *Zernike polynomials and atmospheric turbulence*, JOSA, 66, 207-211.
- Obukhov A.M, 1949, Izv. Akad Nauk SSSR, Ser Geo Geofiz, 13, 58.
- O'Byrne J W, 1968, *Seeing measurements using a shearing interferometer*, PASP, 100, 1169-1177.
- Pfrommer T, Hickson P, She J-L, Vance J D, 2008, *High-resolution lidar experiment for the Thirty-Meter Telescope*, SPIE, 7015, in press.
- Racine R, 1996, *The telescope point spread function*, PASP, 108, 699-705.
- Ragazzoni R, 1996, *Pupil plane wavefront sensing with an oscillating prism*, J Mod Optics, 43, 289-293.
- Roddier F, 1981, The effects of atmospheric turbulence in optical astronomy, Prog in Optics, XIX, 281-376.

- Roddier F, 1988, *Curvature sensing and compensation: a new concept in adaptive optics*, Appl Optics, 27, 1223-1225.
- Roddier F (ed), 1999, *Adaptive Optics in Astronomy*, Cambridge Univ Press.
- Tatarski V I, 1961, *Wave Propagation in a Turbulent Medium*, McGraw-Hill, NY.
- Tokovinin A, & Travuillon, T, *A model of optical turbulence profile at Cerro Pachón*, MNRAS, 365, 1235-1242.
- Tyson R K, 1998, *Principles of Adaptive Optics*, Academic Press, Boston.
- Tyson R K, 2000, *Introduction to Adaptive Optics*, SPIE, Bellingham.
- Tyson R K, Frazier, 2004, *Field Guide to Adaptive Optics*, SPIE, Bellingham.
- Yaglom A M, 1949, Dan SSSR, 69, 743.